# Exploring DJ-1 as a Therapeutic Target in 2D and 3D Models of Melanoma

Emilia Apollonia Szlosarek

October 2025

UEA registration number: 100269764

# I) Acknowledgements

I would like to thank several wonderful people with whom I worked with over the course of my Master's by Research project. Firstly, I would like to thank my supervisors, Prof. Maria O'Connell and Dr. Emily Hobson for all their amazing support and guidance throughout my project, especially when I was finding it tough. I am very grateful for all their help and answering my many questions! Secondly, I would like to thank Dr. Sean Tattan and Dr. James McColl for their help with advanced microscopy imaging and analysis, and Prof. Mark Searcey and Dr. Zoë Goddard for their advice and feedback on my project.

Additionally, I would like to thank all those who helped me in the lab. Firstly, I would like to thank Dr. Isabel Hamshaw who was always very positive and supportive, and Dr. Daria Golubova who gave good advice and always left sweet treats for us in the write-up room to keep us going! Next, I would like to thank Dr. Rebecca Casson for her help, Will Robinson for his friendship and support and Megan Williams who started the DJ-1 project and helped me with any questions I had.

I would also like to thank my friends Rana, Natalia and Abby who were always willing to listen to me talk about stressful lab days and when experiments were not going the way I hoped. I am so glad that I have such kind-hearted friends.

Finally, I would also like to thank my family for their endless support, patience, guidance and belief in me – I love you all.

# II) Abstract

DJ-1, also known as PARK7, is a Parkinson's disease-associated protein and oxidative stress sensor, which can activate the redox-sensitive Nrf2 pathway. Recent evidence has demonstrated that DJ-1 is overexpressed in various cancers, including melanoma, suggesting it has a role in cancer development and progression and may therefore serve as a potential therapeutic target. The mechanisms behind this role remain incompletely elucidated; nonetheless, it appears to be due to DJ-1's capabilities in protecting cancer cells from oxidative damage and its regulation of multiple signalling pathways involved in carcinogenesis and chemoresistance, including the Nrf2 pathway. This project aimed to investigate the role of DJ-1 and its potential as a therapeutic target in melanoma via 2D and 3D *in vitro* tissue models.

In a 2D *in vitro* model of melanoma, metastatic A375 DJ-1 expressing cells cultured in a monolayer exhibited DJ-1 protein in both the cytoplasm and nuclei. DJ-1 knockdown via siRNA transfection was validated by siGLO and RT-qPCR, with results showing that 100 nM DJ-1 siRNA decreased DJ-1 mRNA levels by 65% but had no significant effects on Nrf2, heme oxygenase-1 or NADPH quinone oxidoreductase-1 mRNA expression, two downstream target genes of Nrf2. 100 nM DJ-1 siRNA significantly decreased A375 cell viability, suggesting that DJ-1 may influence A375 cell proliferation. Addition of the BRAF inhibitor, vemurafenib (1 µM), following knockdown had no extra effect on cell viability compared to the non-targeting control in combination with vemurafenib (1 µM).

To test DJ-1's potential as a therapeutic target for melanoma, experiments involving the small molecule inhibitor of DJ-1, STK793590, were conducted. STK793590 targets the DJ-1 homodimer. STK793590 (50 µM) in combination with vemurafenib (1 µM) reduced A375 cell viability by 58% compared to the DMSO control. Intriguingly, STK793590 had no effects on mRNA expression of DJ-1, Nrf2, heme oxygenase-1 or NADPH quinone oxidoreductase-1. Following experiments in the 2D *in vitro* model of melanoma, 3D *in vitro* models of melanoma were developed and optimised to test the effects of STK793590 in combination with vemurafenib on A375 tumouroid growth. The Matrigel Matrix, 'hanging drop' and ultra-low adherence (ULA) plate methods were investigated. Out of these, the ULA plate method proved most favourable to conduct these experiments. Vemurafenib alone (1 µM) and STK793590 (50 µM) in combination with vemurafenib (1 µM) caused significant decreases in A375 tumouroid growth, however the combination was no better than vemurafenib treatment alone. Overall, this project revealed disparate results in 2D *in vitro* models compared to 3D *in vitro* models, necessitating further studies to confirm the potential of DJ-1 *in vivo* as a therapeutic target in skin melanoma.

# III) List of Contents

# IV) Presentations

Szlosarek, E. A., Pavlyk, I., Carpentier, J., Chan, P. Y., Bomalaski, J. S., Szlosarek, P. W. (2024) Pegargiminase (ADI-PEG20) and melphalan as a novel drug combination for uveal melanoma. *Keystone Symposia, Tumor Metabolism*, 12th-15th February 2024 (Banff, Canada) (Poster).

Szlosarek, E. A., Williams, M., Hobson, E., Tattan, S., O'Connell, M. A. (2024) Exploring DJ-1 in melanoma: A potential novel therapeutic target. *Norwich Cancer Research Network Symposium*, 11th September 2024 (Norwich, UK) (Poster).

Szlosarek, E. A., Williams, M., Hobson, E., Tattan, S., O'Connell, M. A. (2024) Exploring DJ-1 in melanoma: A potential novel therapeutic target. *University of East Anglia's Chemistry, Pharmacy and Pharmacology Research Day*, 13th September 2024 (Norwich, UK) (Poster).

Szlosarek, E. A., Williams, M., Hobson, E., Tattan, S., O'Connell, M. A. (2025) Exploring DJ-1 as a therapeutic target in 2D and 3D models of melanoma. *University of East Anglia's Chemistry, Pharmacy and Pharmacology Research Day*, 2nd September 2025 (Norwich, UK) (Poster and Oral Presentation).

# V) List of Tables

# VI) List of Figures

# VII) Abbreviations

ABC – ATP-binding cassette

AKT – Protein kinase B

ARF – Alternative reading frame

ATM – Ataxia telangiectasia mutated

$\alpha$-MSH – Alpha-melanocyte stimulating hormone

ANOVA – Analysis of variance

APAF-1 – Apoptotic Protease-Activating Factor-1

APC – Antigen presenting cell

ARE – Antioxidant response element

ASK1 – Apoptosis signal-regulating kinase 1

Bad – BCL-xL/BCL-2 associated death promotor

BAK – BCL-2 homologous antagonist killer

BAX – BCL-2 associated X-protein

BBB – Blood brain barrier

BCC – Basal cell carcinoma

BCL-2 – B-cell lymophoma-2

BCL-xL – B-cell lymphoma-extra large

BCP-1 – bromo-2-chloro-propane

β-TrCP – Beta-transducin repeats-containing proteins

Bim – BCL-2 interacting mediator of cell death

BRAF – B-raf proto-oncogene

BSA – Bovine serum albumin

bZip – Basic region leucine zipper

cAMP – Cyclic adenosine monophosphate

CARs – Chimeric antigen receptors

CDKN2A– Cyclin dependent kinase inhibitor 2A

CDKs – Cyclin-dependent kinases

cDNA – copy DNA

CHK2 – Checkpoint kinase 2

CNC – Cap 'N' Collar

CPX – Ciclopirox olamine

CRAF – RAF Proto-oncogene serine/threonine-protein kinase

CSCs – Cancer stem cells

Ct – Cycle threshold

CT – Computed tomography

CTLA-4 – Cytotoxic T-lymphocyte associated protein 4

CUL1 E3 – Cullin-1 ubiquitin E3 ligase complex

CUL3 – Cullin 3

CYP450 – Cytochrome P450

Cys106 – Cysteine 106

DADS – Diallyl disulfide

DAPI – 4',6-diamidino-2-phenylindole

Daxx – Death domain associated protein

DES – Diethylstilboestrol

DCM – Dichloromethane

DCs – Dendritic cells

DIPEA – N,N-Diisopropylethylamine

DJ-1 – Protein deglycase 1

DLBC – Lymphoid neoplasm diffuse large B-cell lymphoma

DMEM – Dulbecco's Modified Eagle Medium

DMF – Dimethyl fumarate

DMSO – Dimethyl sulfoxide

DNA – Deoxyribonucleic acid

DPBS – Dulbecco's phosphate buffered saline

DTIC – Dacarbazine

E2F – E2 promoter binding factor

EE – Ethinyloestradiol

ECACC – European Collection of Cell Cultures

ECM – Extracellular matrix

EGFR – Epidermal growth factor receptor

EMT – Epithelial-mesenchymal transition

ERK1/2 – Extracellular signal-related kinase 1/2

FBS – Fetal bovine serum

GAPDH – Glyceraldehyde 3-phosphate dehydrogenase

GDP – Guanosine diphosphate

GEPIA – Gene Expression Profiling Interactive Analysis

GLOBOCAN – Global Cancer Observatory

GnRHR – Luteinising hormone-releasing hormone receptor

GST – Glutathione S-transferase

GSH – Glutathione

GTP – Guanosine triphosphate

Hdm2 – Human double minute 2

HER2 – Human epidermal growth factor receptor 2

HIF-1α – Hypoxia inducible factor 1 subunit alpha

HO-1 – Heme-oxygenase 1

HRP – Horseradish peroxidase

HSF1 – heat shock transcription factor 1

IGF1 – insulin-like growth factor 1

IL-2 – Interleukin 2

JNK – c-Jun N-terminal kinases

JNK1 – c-Jun N-terminal kinase 1

kDa – Kilodalton

Keap1 – Kelch-like ECH-associated protein 1

KIT – KIT proto-oncogene

LDH – Lactate dehydrogenase

Leu166 – Leucine166

LH – Luteinising hormone

LMP – Low molecular mass peptide

LY6K – Lymphocyte antigen 6 complex locus K

mAb – Monoclonal antibody

MAPK – Mitogen-activated protein kinase

MC1R – Melocortin-1 receptor

MDM2 – Mouse double-minute 2 homolog

MDR – Multi-drug resistance

MEK – MAP kinase kinase

MEKK1 – Mitogen-activated protein kinase kinase kinase 1

MeOH – Methanol

MGMT – O6-Methylguanine-DNA methyltransferase

MHC – Major histocompatibility complex

MITF – Microphthalmia-associated transcription factor

MRI – Magnetic resonance imaging

mRNA – Messenger RNA

MTIC – 5-(3-methyl-1-trazeno)imizadole-4-carboxamide

mTOR – Mammalian target of Rapamycin

MTS – 3-(4,5-dimethylthiazol-2-yl)-5(3-carboxymethonyphenol)-2-(4-sulfophenyl)-2H-tetrazolium

NADPH – Nicotinamide adenine dinucleotide phosphate

NF1 – Neurofibromin 1

NF-κB – Nuclear factor kappa-light-chain-enhancer of activated B cells

NOTCH1 – Neurogenic locus notch homolog protein 1

NQO1 – NAD(P)H quinone oxioreductase-1

NRAS – Neuroblastoma ras viral oncogene homolog

Nrf2 – Nuclear factor erythroid 2-related factor 2

NT – Non-targeting control

NURR1 – Nuclear receptor related 1 protein

OS – Overall survival

PAAD – Pancreatic adenocarcinoma

PAR-2 – Protease-activated receptor-2

PARK7 – Parkinson's disease protein 7

PBS – Phosphate buffered saline

PCR – Polymerase chain reaction

PD – Parkinson's Disease

PD-1 – Programmed cell death protein 1

PD-L1 – Programmed death-ligand 1

Pen/Strep – Penicillin/Streptomycin

PFA – Paraformaldehyde

PFS – Progression-free survival

P-gp – P-glycoprotein

PI3K – Phosphatidylinositol 3-kinase

PI3K/AKT/mTOR - Phosphatidylinositol 3-kinase/protein kinase B/target of rapamycin

$PIP_2$ – Phosphatidylinositol (4,5)-bisphosphate

$PIP_3$ – Phosphatidylinositol (3,4,5)-triphosphate

PTEN – Phosphatase and tensin homolog

PVDF – Polyvinylidene difluoride

RAS – Reticular activating system

RB – Retinoblastoma protein

RNA – Ribonucleic acid

RNAi – RNA interference

ROS – Reactive oxygen species

RPM – Rotations per minute

RT-qPCR – Reverse transcription-quantitative polymerase chain reaction

RTKs – Receptor tyrosine kinases

SASPs – Senescence-associated secretory phenotype factors

SCC – Squamous cell carcinoma

SDS – Sodium dodecyl sulfate

SERMs – Selective estrogen receptor modulators

shRNA – Short hairpin RNA

siRNA – Small interfering RNA

SKCM – Skin cutaneous melanoma

sMaf – Small musculoaponeurotic fibrosarcoma proteins

SREBP – Sterol regulatory element-binding protein

STAT1 – Signal transducer and activator of transcription 1

STS – Staurosporine

TAP – Transporter associated with antigen processing protein

TBST – Tris-buffered saline with 0.1% Tween20

TCF/LEF – T-cell factor/lymphoid enhancer factor

TERT – Telomerase reverse transcriptase

TH – Tyrosine hydroxylase

THYM – Thymoma

TME – Tumour microenvironment

TMZ – Temozolomide

TNF-α – Tumour necrosis factor alpha

Trx1 – Thioredoxin-1

TSP-1 – thrombospondin-1

UK – United Kingdom

ULA – Ultra-low adherence

UV – Ultraviolet

VEGF – Vascular endothelial growth factor

VEGF-A – Vascular endothelial growth factor A

VEGFC – Vascular endothelial growth factor C

Wnt – Wingless/Integrated

# 1. Introduction and Aims

**1.1 Cancer**

*1.1.1 An introduction to cancer*

Cancer is a ruthless disease characterised by the uncontrolled and erratic growth of cells driven in part by genetic mutations, enabling invasion into tissues and propagation throughout the body. There are many different types of cancer with some of the most common being lung, liver, bowel, female breast and stomach worldwide[1]. In the UK, over 385,000 people are diagnosed with cancer every year, and 167,000 of those diagnosed die[2]. In 2022 alone, it was estimated by the Global Cancer Observatory (GLOBOCAN) that there were 10 million deaths from cancer worldwide and it is currently predicted that there will be 35 million new cancer cases globally every year by 2050[3]. These are dismal statistics indicating that cancer is an ongoing major global health issue. In recent years, there have been advances in cancer research, allowing for better treatments for patients suffering from this disease. Nevertheless, new treatments are constantly needed due to variable patient response rates and ongoing resistance to therapy (see **Section 1.2.3**), highlighting the need for continued research.

*1.1.2 Hallmarks of Cancer*

The 'hallmarks of cancer' is a logical framework that was created by Hanahan and Weinberg in 2000 to help explain the numerous biological characteristics of cancer[4]. Hanahan and Weinberg originally proposed 6 hallmarks, however as of 2022, there are a now a total of 14 cancer hallmarks, with some described as emerging hallmarks or enabling characteristics[5,6]. These are shown below in **Figure 1**. For the purpose of this thesis, sustaining proliferative signalling, resisting cell death and evading growth suppressors are described in more detail.
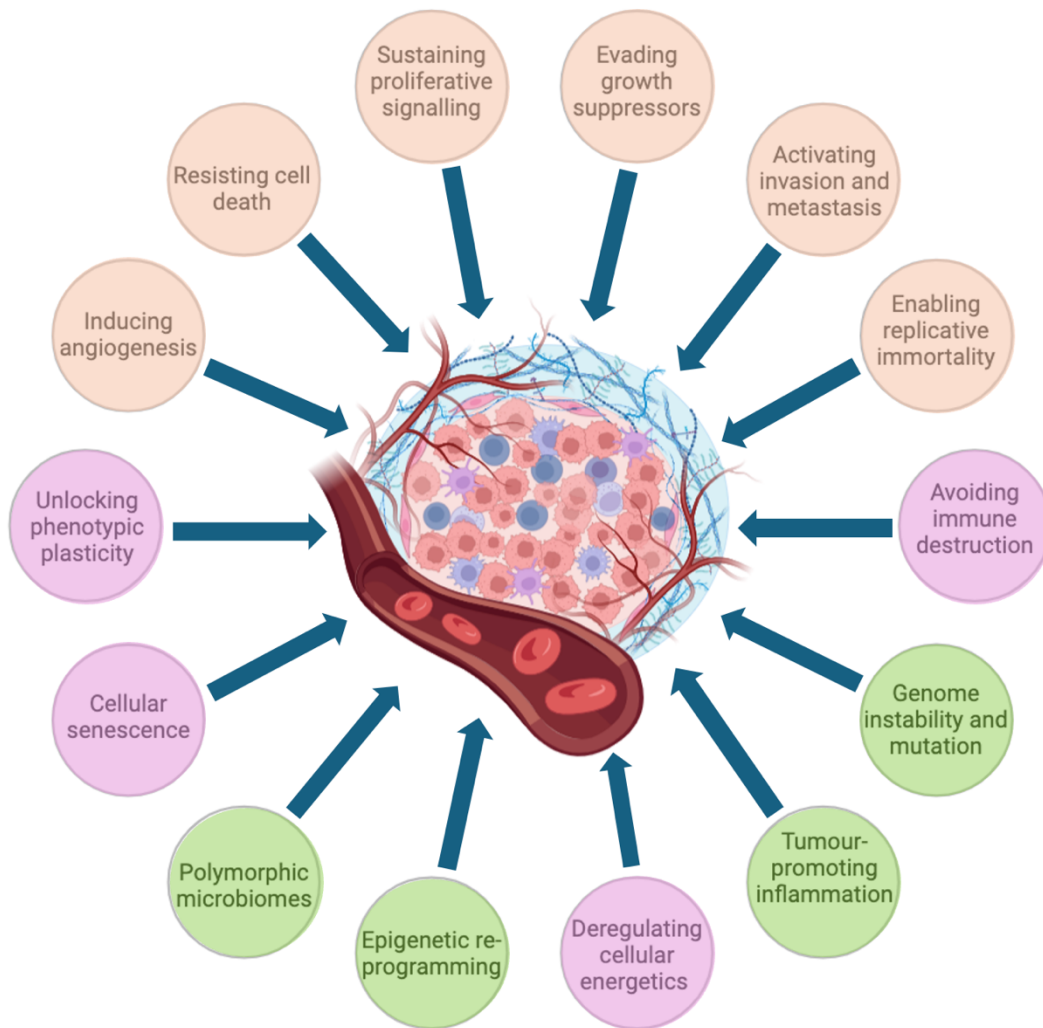
**Figure 1 – The hallmarks of cancer.** There are a total of 14 hallmarks, of which polymorphic microbiomes, non-mutational epigenetic reprogramming, tumour-promoting inflammation and genome instability and mutation are described as enabling characteristics (highlighted in green) and unlocking phenotypic plasticity, cellular senescence, avoiding immune destruction and deregulating cellular energetics are described as emerging hallmarks (highlighted in pink). The original core hallmarks of cancer proposed in 2000 are highlighted in orange (figure created in Biorender and adapted from Hanahan, 2022[6]).

Hanahan and Weinberg argue that one of the most important characteristics of cancer is its ability to sustain proliferative signalling[5]. Healthy cells can meticulously control growth factors which in turn control the cell cycle[5]. On the other hand, cancer cells dysregulate growth factor signalling, therefore also dysregulating the cell cycle[5]. This results in excessive cell division and proliferation. The cell cycle consists of a series of occurrences that occur throughout a cell's life, ultimately culminating in cell division [**Figure 2**]. The two main phases of the cell cycle are the interphase and the mitotic (M) phase[7]. Interphase consists of three phases known as the $G_1$ phase, S phase and $G_2$ phase[7]. $G_1$ is the phase during which the cell grows; it increases in size and produces different organelles and proteins required for synthesis of DNA[7]. The cell then moves into the S phase where it replicates genomic DNA that is present within the nucleus. After this

stage has finished and the DNA has been copied, the cell moves into the $G_2$ phase where it begins preparing for mitotic division[7]. The M phase then follows, and this is where mitosis occurs[7,8]. Mitosis consists of 5 phases known as prophase, metaphase, anaphase, telophase and cytokinesis[8]. Following proper completion of all these phases, the cell can divide the previously copied genetic material into two daughter cells[7,8]. The cell cycle then repeats, allowing for further cell division and proliferation.
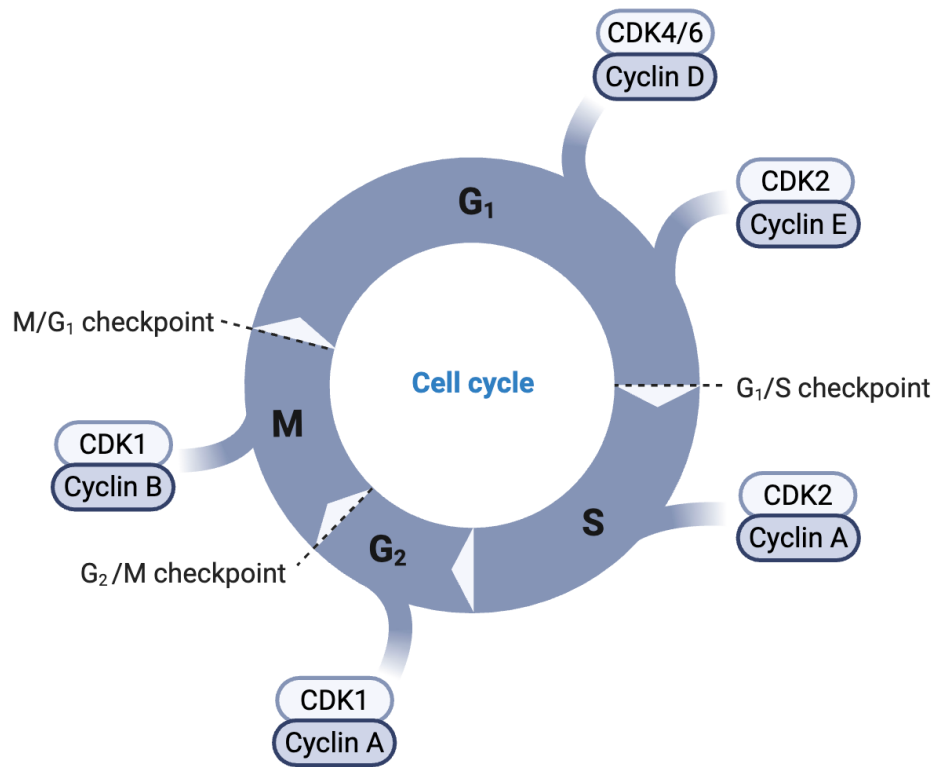


**Figure 2 – The cell cycle.** The cell cycle is made up of the $G_1$, S, $G_2$ and M phases. It is also controlled by various checkpoints throughout. At the $G_1$/S checkpoint, cell size, organelle production, protein production, and any DNA damage is surveyed. At the $G_2$/M checkpoint, cell size and DNA damage is surveyed once again and at the M/$G_1$ phase, attachment between spindle microtubules and chromosomes is surveyed (figure created in Biorender).

Throughout the cell cycle process, there are checkpoints controlled by cyclin-dependent-kinases (CDKs) in distinct signalling pathways that can hamper progression of the cell cycle or trigger cell cycle exit or death if any DNA damage occurs[9] [**Figure 2**]. It is now known that mutations present in cancer cells power continued cell division by interfering with signalling pathways involved in cell cycle exit and entry into S-phase as shown in **Figure 3**.
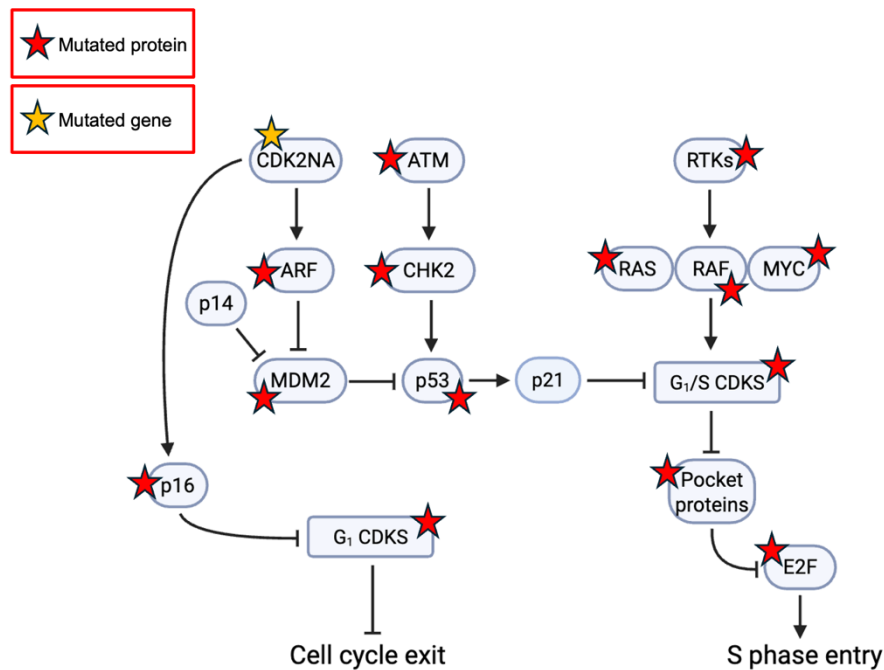
**Figure 3 – Some important signalling pathways implicated in the cell cycle process with common mutations in cancer which drive cell cycle progression.** Commonly mutated genes in cancer are indicated by an orange star and commonly mutated proteins in cancer are indicated by a red star, whereas less commonly mutated proteins are indicated without a star. It is important to note that, in most cases, the proteins illustrated are named after the genes that encode them. Mutations in cancer are predominantly associated with cell cycle regulation in response to DNA damage and growth signals prior to S phase. Each of the shown genes, proteins and pathways have potential to be targets for cancer treatment. ATM plays a crucial role in repairing damaged DNA, ARF and CHK2 are both tumour suppressor proteins, MDM2 targets proteins for degradation via the proteasome and pocket proteins include tumour suppressors retinoblastoma protein (RB), p107 and p130. Abbreviations: ARF, alternative reading frame; ATM, ataxia telangiectasia mutated; CDK, cyclin dependent kinase; CHK2, checkpoint kinase 2; MDM2, mouse double minute 2 homolog; RTK, receptor tyrosine kinase (figure created in Biorender and adapted from Matthews, Bertoli and Bruin, 2021[9]).

An alternative way that cancer cells sustain proliferative signalling is through evading growth/tumour suppressors which is another fundamental hallmark of cancer[5]. p16 is a cyclin kinase inhibitor and an example of a tumour suppressor that regulates the cell cycle[10,11] as shown in **Figure 3**. It is encoded for by the CDKN2A gene[10,12]. The main role of p16 involves inactivating the G1 phase-CDK complexes of the cell cycle[10,11]. When G1-CDK complexes are inactivated, cell cycle exit is inhibited. CDKN2A is commonly mutated in cancer as described [**Figure 3**] and as a result p16 may not be produced[13]. If this occurs, cell cycle exit cannot happen, and cancerous cells continue proliferating[13]. p14 is another tumour suppressor whose main role involves promoting p53 activation[14]. p53 is a tumour suppressor itself which inhibits cell proliferation and induces apoptosis via cell death regulators such as BCL-2/BAX when DNA damage is apparent[15]. p14 inhibits MDM2, a protein targeting p53 for degradation in the proteasome[16,17]. Owing to

this inhibition, p53 stays active and induces p21 expression which allows arrest of CDK2/1-cyclin A/B complexes, thereby preventing cell cycle progression from the $G_2$ to M phase or $G_1$ to S phase via E2F inhibition[16,17,18]. E2F is a transcription factor which mediates transcription of genes needed for S phase cell cycle progression[9,17,18]. CDKNA mutations with p14 loss are also commonly seen in cancer, resulting in p53 loss of function[14,19]. These allow cancer cells to evade apoptosis and continue to proliferate.

Cancer cells can also become resistant to cell death [**Figure 1**], for example through p53 loss of function[5]. p53 is involved in the BCL-2 apoptotic pathway, also known as the cell intrinsic pathway of apoptosis, which is controlled and balanced by various pro- and anti-apoptotic proteins[20]. BCL-2 is an anti-apoptotic protein and binds to two pro-apoptotic proteins known as BAX and BAK, keeping them inoperative[5]. Under DNA damage conditions, p53 can activate BAX and BAK, triggering release of Cytochrome C from mitochondria which then leads to formation of a Cytochrome C, Procaspase9 and APAF-1 (Apoptotic Protease-Activating Factor-1) complex[21]. As a result, caspase-9 is activated and induces caspase-3, -6, and -7 activation which in turn induce apoptosis of the cell[21]. p53 loss of function mutations cause BAX and BAK to remain inactive, preventing the downstream signalling essential for apoptosis, allowing the cancer cell to survive[22]. Aside from evading cell death via p53 loss of function, cancer cells can also become resistant against cell death by upregulating anti-apoptotic proteins such as BCL-2 and downregulating pro-apoptotic proteins such as BAX and BAK, or by bypassing the cell extrinsic ligand-induced death pathway[5].

Other important and essential hallmarks of cancer include inducing angiogenesis and avoiding immune destruction[6]. Angiogenesis is a process that provides tumours with all the nutrients they need for survival through the formation of new blood vessels from pre-existing ones[5]. This process is often mediated by angiogenic promoting or inhibitory regulators such as vascular endothelial growth factor-A (VEGF-A) and thrombospondin-1 (TSP-1)[5]. Avoiding immune destruction encompasses processes that reduce the efficacy of mechanisms in charge of immune system recognition and elimination of cancer cells[5]. Disarray of antigen presentation is one example of such a process[23]. This usually comes about through efficacy disruption of the major histocompatibility complex (MHC) I pathway, transporter associated with antigen processing (TAP) protein, tapasin and LMP2 and LMP7 which are MHC-encoded proteasome subunits[24].

The 'hallmarks of cancer' is an extremely important framework that aids us in our understanding of how cancer operates so that new treatments can be discovered. This framework is constantly transforming. For instance, non-mutational epigenetic reprogramming was only recently added to the hallmark framework (as an enabling characteristic) due to increasing evidence that gene-regulatory networks in tumours can be controlled by various compromised and adopted mechanisms that are not influenced by gene mutation or genome instability[6,25,26]. Cellular senescence is a term used to

describe cells in a persistent cell cycle arrest state and was also only recently added to the framework[27]. In cancer, senescent cells stop proliferating and become resistant to apoptosis[6]. Recent insights have indicated that these cells start secreting senescence-associated secretory phenotype (SASP) factors which instigate tumour growth and vascularisation and additionally activate invasion and metastasis of cancer cells[6,28,29]. These added hallmarks confirm the dynamic nature of the framework and substantiate the likelihood that more novel characteristics will undoubtedly be added to it in the future.


*1.1.3 Current treatments for cancer*

Considering the widespread nature of cancer, treatment is vital. Various treatment options may be available to a cancer patient. These can include surgery, chemotherapy, radiotherapy, immunotherapy, hormonal therapy, targeted therapy and stem cell or bone marrow transplants. The type of cancer and its stage dictate the type of treatment a patient will receive. It is often common for patients to receive a combination of different cancer therapies, for instance, patients with melanoma may have chemotherapy treatment along with immunotherapy treatment and surgery.

Chemotherapy is an anticancer treatment that involves the use of cytotoxic drugs to kill cancer cells[30]. The main types of cytotoxic drugs used in chemotherapy fall under 4 groups: alkylating agents, antimetabolites, cytotoxic antibiotics and plant derivatives[31]. Each group of cytotoxic drugs has a specific mechanism of action which have been compiled in **Table 1** along with class examples. Although the mechanism of action for each group is different, suppression of cell proliferation is the main overriding theme. The idea of using chemotherapy to treat cancer was first born at the beginning of the 20th century but not fully realised until the 1940s during World War II by pharmacologists Alfred Gilman and Louis Goodman[32]. Gilman and Goodman's research on sulfur and nitrogen mustards (chemical warfare alkylating agents), ultimately led to the first therapeutic experiments involving intravenous administration of mustard agents into patients with lymphoma[32,33]. The results of these experiments showed remarkable tumour regression and drugs developed from mustard agents are now widely utilised in the clinic. There are however significant pitfalls to using cytotoxic drugs, which include severe side effects as caused by chemotoxicity, a term that describes damage inflicted upon healthy cells by the toxic nature of chemotherapy[32,33]. Some of these side effects include hair loss, bone marrow toxicity and sterility[34]. Since the invention of chemotherapy, there has been a big shift into precision and personalised cancer medicine[35]. Personalised cancer medicine takes a more specific treatment approach compared to chemotherapy, so the toxic side effects seen with chemotherapy are avoided. Immunotherapy and various targeted therapies are archetypes of precision and personalised cancer medicine and are discussed next.

**Table 1 – Cytotoxic drugs used in chemotherapy** (adapted from Rang and Dale, 2020[31])

| Group | Mechanism of action | Classes | Examples |
|---|---|---|---|
| Alkylating agents | DNA cross-linking (intrastrand). | Nitrogen mustards, platinum compounds, nitrosoureas | Melphalan, Carmustine, Cisplatin |
| Antimetabolites | Inhibition of DNA/RNA synthesis. | Pyrimidine pathway, purine pathway, folate antagonists | Gemcitabine, tioguanine, Methotrexate |
| Plant derivatives | Target assembly of microtubules and inhibit formation of spindles during metaphase stage of cell cycle (vincristine). Can also inhibit activity of topoisomerase (irinotecan) or keep microtubule polymers stable (paclitaxel). | Vinca alkaloids, campothecins, taxanes | Vincristine, Irinotecan, Paclitaxel |
| Cytotoxic antibiotics | Target DNA/RNA synthesis and activity of topoisomerase. | Anthracyclines | Doxorubicin |

Immunotherapy is a treatment which involves utilising a patient's immune system to combat cancer and encompasses both immune system stimulation and inhibition[36]. There are several types of immunotherapies which currently include: immune checkpoint inhibitors, monoclonal antibodies, chimeric antigen receptor (CAR)-T cell therapy, cancer vaccines, adoptive cell transfer and immune system modulators[36]. Monoclonal antibodies (mAbs) are laboratory-developed proteins which identify specific targets, rendering them a type of targeted cancer therapy[31]. Certain mAbs work by inducing apoptosis and suppressing cancer cell survival pathways by binding to and inhibiting receptors and growth factors[31]. Trastuzumab (Herceptin) is a type of humanised murine mAb which works by blocking the human epidermal growth factor receptor 2 (HER2) from conveying signals through pathways such as PI3K (phosphatidylinositol-3 kinase) and MAPK (mitogen-activated protein kinase), therefore inhibiting cell growth and survival[37]. Overexpression of HER2 was first associated with reduced survival in breast cancer in 1987, which then allowed for the invention and approval of trastuzumab in 1998[31,38,39]. Today, trastuzumab is routinely given in combination with chemotherapy drugs such as docetaxel to HER2-positive breast cancer patients following trial results which showed a 79% 1-year survival rate in patients who were given trastuzumab alongside standard chemotherapy[31].

Other mAbs work by stimulating the host immune system after binding to their target, causing cancer cells to die via killer T cells or complement-mediated lysis[31]. These types of mAbs are known as immune checkpoint inhibitors and Nivolumab is one example. Immunological checkpoints regulate immune responses and prevent the immune system from targeting healthy cells (self-tolerance)[36]. Nivolumab is a humanised mAb that targets a receptor called programmed cell death protein 1 (PD-1), which is important

in suppressing immune response and thus T-cell activation to enhance self-tolerance[31]. Through blocking the PD-1 receptor, PD-L1 (the ligand to PD-1) is prevented from binding, reversing T-cell suppression[40]. This mechanism allows the immune system to better detect cancer cells which have previously avoided immune monitoring[31]. Nivolumab is used in the treatment of many different cancers some of which include mesothelioma, melanoma, non-small cell lung cancer, kidney cancer, lymphoma and head and neck cancers[41].

CAR-T cell therapy and cancer vaccines are two examples of novel developing immunotherapy treatments. CAR-T cells are purpose-built T-cells that express chimeric antigen receptors (CARs) and are a type of adoptive cell transfer therapy[42]. These receptors enable the purpose-built T-cells to identify antigens present on tumour cells through an MHC-independent approach[42,43]. This process leads to release of inflammatory cytokines such as interleukin 2 (IL-2) and tumour necrosis factor $\alpha$ (TNF-$\alpha$), hence inducing anti-tumour effects[43]. The first CAR-T cell therapy to be approved was tisagenlecleucel (Kymriah) in 2017 for the treatment of B-cell acute lymphoblastic leukaemia, which was engineered to target the CD19 protein on B cells[44]. Tisagenlecleucel was approved following results from the phase II ELIANA clinical trial (NCT02435849) which showed an 83% remission rate in paediatric patients with B-cell acute lymphoblastic leukaemia[44,45]. Nonetheless, there are drawbacks to CAR-T cell therapy, including severe side effects and limited efficacy against solid tumours[46]. Compared to CAR-T cell therapy, cancer vaccines are still in the very early stages of development. Their mechanism of action involves boosting the adaptive immune system towards specific tumour antigens to control tumour growth and to eliminate any remaining disease[47]. Clinical trials concerning cancer vaccines have seen disappointing results thus far which can be attributable to factors such as tumour immune microenvironment suppression; yet certain studies have indicated that cancer vaccines can be effective when considering the right settings[47,48]. For instance, a phase I clinical trial found that screening patients with gastric cancer for LY6K expression prior to treatment with a LY6K-177 peptide vaccine therapy resulted in good tolerance with some reported anticancer benefit[49].

Certain cancers can be hormone-dependent if they occur in tissues which are sensitive to hormones. In these cases, hormonal therapy can be used as a treatment; hormone agonists or antagonists are administered to hinder growth of tumours[31]. An example of a hormone antagonist is tamoxifen, an antioestrogen given to patients with breast cancer[31]. Tamoxifen belongs to a group of drugs known as selective estrogen receptor modulators (SERMs) and its mechanism of action in breast tissue involves binding to estrogen receptors, competing against endogenous estrogen, thus suppressing transcription of genes that respond to estrogen[31,50]. Tamoxifen was first authorised for use in advanced breast cancer; however, additional adjuvant studies revealed that tamoxifen decreased contralateral breast cancers by 30-50%[50]. Examples of hormone agonists include

gonadotrophin-releasing hormone agonists such as buserelin and goserelin which are used in the treatment of prostate cancer[31]. The mechanism of action for both involves binding to the luteinising hormone-releasing hormone receptor (GnRHR) on anterior pituitary cells, leading to initial secretion of luteinising hormone (LH)[51]. However, with continuous exposure, these agonists subsequently start to inhibit LH secretion, resulting in a drop in testosterone and dihydrotestosterone, which prostate cancer cells rely on for growth[51].

In summary, there are a plethora of different cancer treatments which can be chosen and adjusted (including combination treatments) to suit a patient's needs, however there are still issues that need to be addressed. Treatments such as chemotherapy come with severe side effects and fail to consider the heterogeneity of cancer; some patients may respond well to a certain treatment whilst others may not. Therapies that fall under the personalised cancer medicine branch cause less severe adverse effects compared to chemotherapy, yet despite this, side effects are induced regardless. Aside from this, there is also an increasing problem with cancers becoming resistant to drugs through various mechanisms[52] (see **Section 1.2.3**). These types of challenges will need to be overcome to better improve cancer treatment for the future.

**1.2 Melanoma**

*1.2.1 An introduction to melanoma*

Melanoma is the most lethal form of skin cancer commonly caused by overexposure to ultraviolet (UV) radiation from the sun or artificial sources such as tanning beds[53]. In addition to UV overexposure, there are several other risks which can also increase the likelihood of developing melanoma[53] (see **Table 2**).

**Table 2 – Risk factors for melanoma** (adapted from Long *et al*, 2023[53])

| Risk factors for melanoma |
|---|
| UV radiation overexposure from the sun:<br>• Total sun exposure of any kind<br>• History of sunburn<br>• First childhood sunburn (under 13 years old)<br>• Acute sunburn – 10/more episodes<br>UV radiation overexposure from indoor tanning beds:<br>• Any use – 1/more sessions<br>• Early exposure (under or equal to 20 years old)<br>• Excessive use – 10/more sessions per year |
| Atypical naevi (moles) |
| High number of naevi – more than 100 |
| History of melanoma |
| History of non-melanoma skin cancer (e.g. basal cell carcinoma or squamous cell carcinoma) |
| First-degree relative with melanoma (e.g. father) |
| Xeroderma pigmentosum |
| Skin type (e.g. skin type I and II are high risk) |
| Red hair colour |
| Blue eye colour |
| Male sex |

Melanoma can often be successfully treated in its earlier stages, usually with surgery; however, survival rates fall markedly after metastasis[54]. To help diagnose melanoma in its earlier stages, the **ABCDE** acronym is used when observing naevi[55]. The acronym stands for **A**symmetrical, **B**order, **C**olour, **D**iameter, and **E**volving[55]. If a naevus is asymmetrical, has irregular borders, is more than one colour, has a large diameter (over 6 millimetres) or evolves over time in shape, colour or size, it is recommended to go and see a doctor[55]. Males are more likely to have melanomas on their trunk area whereas women are more likely to have melanomas on their legs[53]. A doctor will conduct a skin exam and may take a skin biopsy (either a shave, punch, incisional or excisional) to test for melanoma. If a diagnosis of melanoma has been made, additional tests such as magnetic resonance imaging (MRI) and computed tomography (CT) scans may be done to ascertain the stage that it is at[55] (see **Figure 4** for melanoma stages).
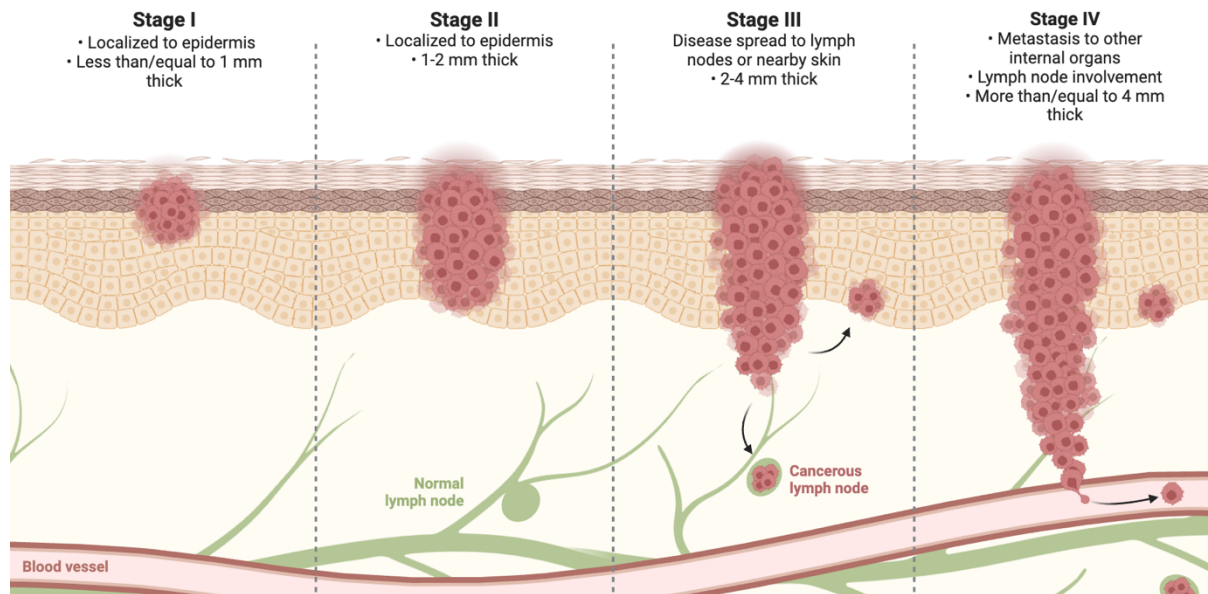
**Figure 4 – The stages of melanoma** (figure adapted from Biorender).

In the UK, approximately 17,500 people are diagnosed with melanoma each year and the incidence rate of melanoma is rising fast worldwide[56,57]. Mortality rates for melanoma in the UK have been declining in recent years, mainly due to better treatment availability and increased awareness about the risk factors such as UV exposure, yet it is still predicted there will be 2,800 deaths from melanoma cancer every year by 2038-2040[58]. Melanoma has a high mutational burden and relies heavily on intracellular signalling pathways such as MAPK and PI3K[59].

Melanoma develops from skin cells called melanocytes[60]. Melanocytes are melanin-producing pigment cells which originate from neural crest cells during development[60]. They are mainly found in the basal layer of the skin epidermis but can also be found in places such as the eye, meninges and gastrointestinal tract[53,61]. Melanin consists of a combination of yellow/orange pigment (pheomelanin) and brown/black pigment (eumelanin)[62]. These are credited for the pigmentation of skin, hair and eyes, with eumelanin specifically attributed to the protection of skin from UV damage[62-65]. Production and storage of melanin pigment occurs in distinct melanocyte organelles known as melanosomes[66,67]. These melanosomes are relayed on to keratinocytes, vital cells possessing immune-related functions also found within the epidermis, which internalise and arrange melanin pigment, allowing for protection against UV radiation[63,67,68]. Keratinocytes are the most prevalent cell type in the epidermis and surround melanocytes[66,68]. The exact processes behind melanin transport into keratinocytes via melanosomes and melanin internalisation by keratinocytes are still not fully understood[69]. There are a few hypotheses, though it is mainly thought that melanin transport occurs via an intricate exocytosis-endocytosis model and that melanin internalisation occurs via phagocytosis through protease-activated receptor-2 (PAR-2)[69].

Under DNA damage conditions caused by UV radiation, both melanocytes and keratinocytes secrete $\alpha$-melanocyte stimulating hormone ($\alpha$-MSH) which binds to G-protein-coupled melanocortin receptor 1 (MC1R) present on melanocytes, activating the cyclic AMP (cAMP) pathway and promoting melanin production and DNA repair[70,71].

Melanocyte transformation by genetic mutations leads to melanoma[60,72]. Mutations induce significant abnormalities in key melanocyte signalling pathways, resulting in aberrant development and proliferation. As melanocytes proliferate, naevi (moles) form, which are often benign in nature, however some can progress to intermediate neoplasms and finally to invasive/malignant melanoma[60]. Types of mutations differ between the two main categories of melanoma which are referred to as chronically sun damaged (CSD) or not chronically sun damaged (non-CSD). CSD melanomas are usually associated with mutations such as NRAS, NF1, KIT and BRAF[nonV600E] whereas non-CSD melanomas are associated with BRAF[V600E] mutations[60]. NRAS (also known as Neuroblastoma Ras Viral Oncogene Homolog) is a mutant/oncogene of the RAS protein involved in MAPK and PI3K signalling (see **Figure 5**) and up to around 30% of all melanomas are NRAS-mutated[73,74]. Receptor tyrosine kinases (RTKs) such as epidermal growth factor receptor (EGFR) are activated by growth factors (e.g. EGF) which in turn activate NRAS[75]. Activated NRAS then triggers the MAPK pathway (comprising of BRAF/CRAF, MEK, and ERK) and the PI3K pathway (comprising of PI3K, PDK1, AKT, and mTOR) leading to cell survival and proliferation through AP-1-mediated cell cycle progression[73]. NRAS-mutated melanocytes can induce constant activation of the MAPK and PI3K pathways, giving rise to excessive/sustained cell proliferation and therefore melanoma progression[73]. For instance, NRAS[Q61] (located at codon Gln[61]) is the most common type of NRAS-mutated melanoma, and is able to induce constant activation of MAPK and PI3K through conformational modifications which keep RTK-associated RAS-GTPase proteins in a constant GTP-bound active state[73,76]. There are currently no approved treatments which target NRAS due to its tight bond formation between active RAS-GTP and inactivated RAS-GDP forms[77,78].

BRAF is a mutant/oncogene of the BRAF protein kinase which, like NRAS, is involved in MAPK signalling[79]. BRAF is mutated in about 50% of all melanomas, of which the greater part are BRAF[V600E] (located at amino acid 600) mutations[80]. BRAF[V600E] mutations lead to constant activation of the MAPK pathway regardless of extracellular factors[81]. Most BRAF mutations also coincide with PTEN loss of function mutations in melanoma[57]. PTEN is a tumour suppressor that inhibits PI3K signalling by dephosphorylating phosphatidylinositol (3,4,5)-triphosphate ($PIP_3$) to phosphatidylinositol (4,5)-bisphosphate ($PIP_2$)[82]. This then inhibits AKT activation which is known to control cell proliferation but also inhibit pro-apoptotic proteins such as BCL-2-associated death promotor (Bad) to suppress cell death[82]. When PTEN function is lost, PDK1 is activated by $PIP_3$ which then activates AKT, meaning that the PI3K signalling pathway is continuously activated, allowing cancer cells to proliferate and evade apoptosis[82].

Around 15% of patients with melanoma carry mutations in neurofibromin 1 (NF1)[83]. NF1 is a tumour suppressor gene that inhibits activity of the RAS protein in the MAPK signalling pathway[83,84]. Mutations that cause loss of NF1 keep RAS in its active form (GTP-bound) which leads to intensified MAPK signalling[84]. KIT is a proto-oncogene RTK that is mutated in approximately 1-3% of all melanomas[84]. Mutations in KIT often lead to disruption or constant activation of PI3K and MAPK signalling pathways[85,86].
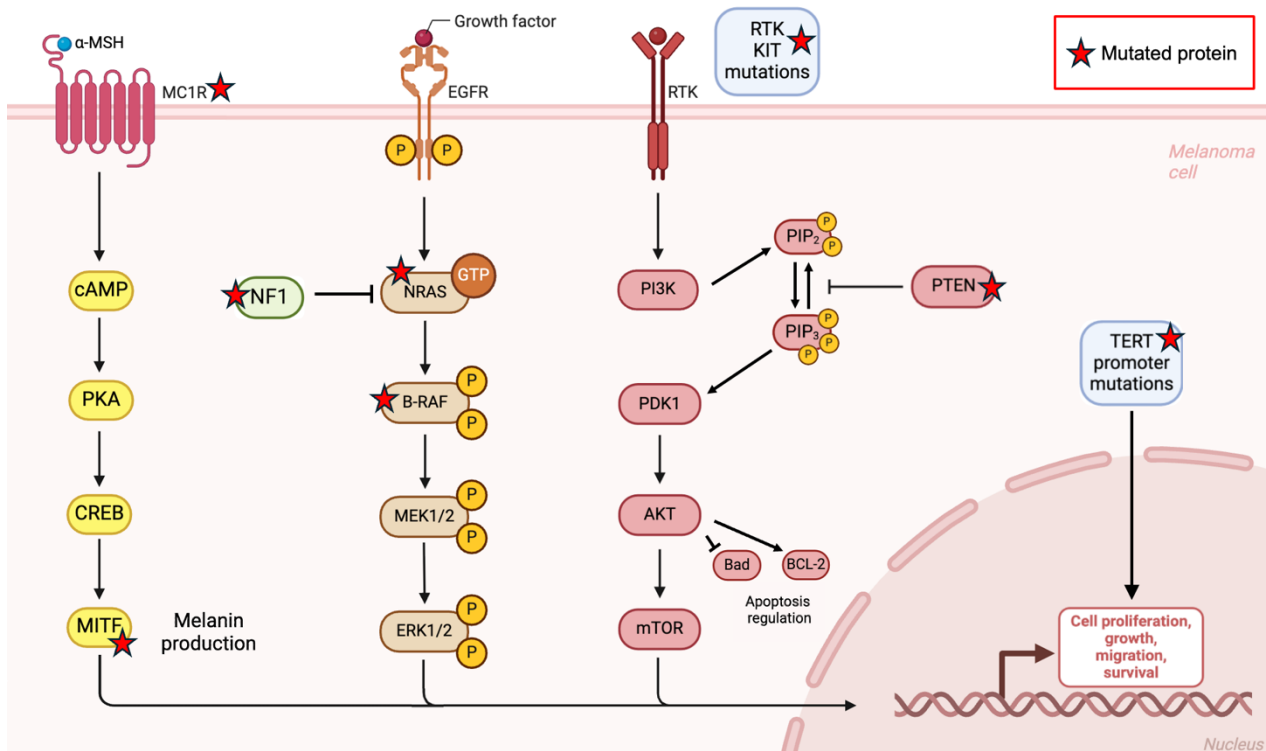


**Figure 5 – Key signalling pathways in melanoma highlighted with frequently mutated proteins.** Key signalling pathways in melanoma include PI3K, MAPK and MC1R which all contribute to melanoma cell proliferation, growth, migration, survival. The MC1R pathway additionally regulates melanin production. Frequently mutated proteins in the pathways are indicated with a red star. These mutations disrupt normal cell functions and usually lead to overactivation of the shown signalling pathways, allowing melanoma cells to continue proliferating and evade apoptosis (figure adapted from Biorender and Davis *et al*, 2018[84]).

Aside from mutations most seen in CSD and non-CSD melanomas, there are numerous additional types of mutations linked to melanoma. For instance, mutations in Microphthalmia-associated Transcription Factor (MITF) are found in approximately 10-20% of melanoma tumours[87]. MITF is involved in regulation of various melanocyte growth, survival and differentiation signalling pathways[87,88]. For example, MITF controls expression of the p21 gene in the cell cycle meaning that mutations in MITF lead to cell cycle dysregulation, thereby promoting tumour progression[87]. Telomere reverse transcriptase (TERT) promoter mutations are also seen in melanoma. The TERT gene controls the enzyme telomerase which has functions in cell activity, telomere stability and genome stability[89]. Telomeres are nucleoproteins found at the ends of chromosomes and their main function is to maintain genome stability. They are also known to shorten

in length with every cell division[90]. TERT promoter mutations lead to increased TERT transcription and telomerase activity resulting in maintained telomere length which allows for continuous proliferation and replicative immortality[89]. MC1R (receptors present on melanocytes discussed earlier) loss of function mutations are associated with red hair and freckled/fair skin phenotypes which are more sensitive to UV radiation[88]. These MC1R loss of function mutations cause an imbalance in the eumelanin/pheomelanin ratio; eumelanin production is decreased whereas pheomelanin production is increased[63]. Since eumelanin provides protection against UV radiation[63,64], a reduction in its production (due to MC1R loss of function) elevates the risk of melanoma development[64].

Overall, melanoma is a cancer with an extremely high mutational burden. Mutations in melanocytes cause dysregulation of key signalling pathways, most notably PI3K and MAPK. However, there is evidence that additional pathways such as the wingless/integrated (Wnt), are also dysregulated in melanoma[91]. The Wnt pathway regulates cell proliferation and migration by activating β-catenin, a transcriptional co-activator that interacts with TCF/LEF transcription factors to activate target genes[92]. Activating Wnt mutations cause overactivation of β-catenin which drives excessive proliferation, survival and migration of melanoma cancer cells[91].


*1.2.2 Current treatments for melanoma*

Methods of treating melanoma today include surgery, chemotherapy, radiotherapy, immunotherapy and targeted therapy. Surgery is the first line of treatment for all stages of melanoma but is most successful in the early stages when metastasis has not yet occurred. Chemotherapy, immunotherapy and radiotherapy are often administered as adjuvant therapies following surgical excision of visible melanoma to destroy any remaining cancer cells.

A common type of chemotherapy drug given to patients with melanoma is dacarbazine which is also known as dimethyltriazeno-imidazol carboxamide (DTIC) [**Table 3**]. DTIC has been the conventional chemotherapy for advanced melanoma since 1972[93]. It belongs to the 'alkylating agents' group of cytotoxic drugs used in chemotherapy (see **Section 1.1.3**) and is given intravenously. Its mechanism of action involves generating 3-methyl-(triazen-1-yl)imidazole-4-carboxamide (MTIC) after activation by liver enzymes belonging to the cytochrome P450 family[94,95]. MTIC has cytotoxic capabilities; it alkylates DNA bases thereby inhibiting replication of DNA, leading to apoptosis[95,96]. However, DTIC only has a response rate of 15-20% in melanoma patients, with a progression-free survival (PFS) of 3-6 months prior to developing resistance to treatment[95,96]. Temozolomide (TMZ) is another common chemotherapy drug given to patients with advanced melanoma[97]. It is an analogue of dacarbazine and a prodrug that is
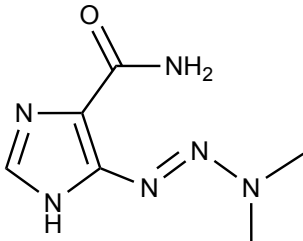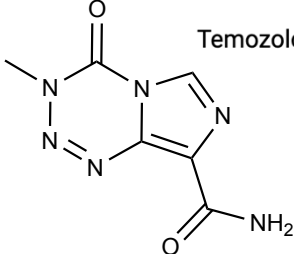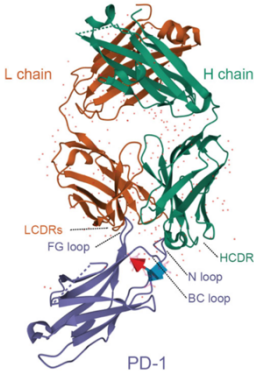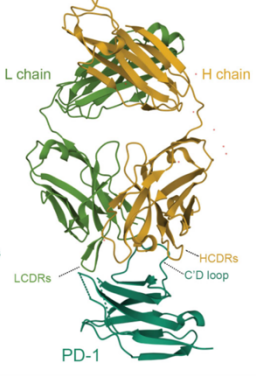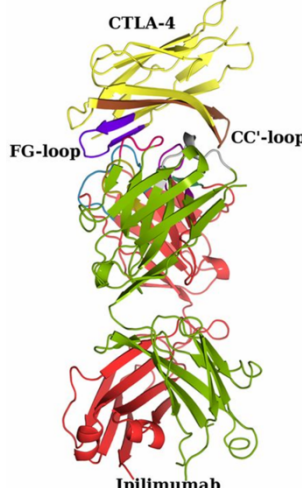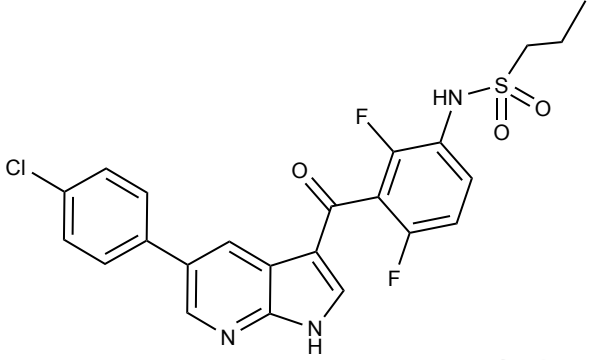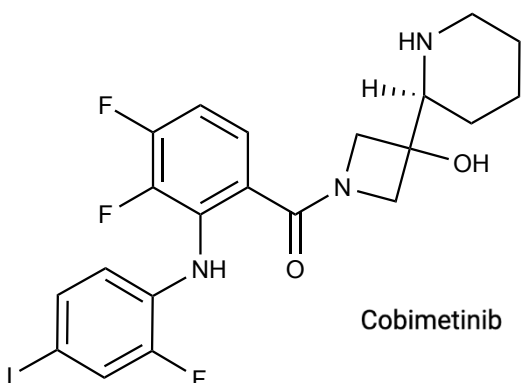
metabolised to MTIC[97]. The efficacy of TMZ is comparable to that of dacarbazine, as demonstrated by the results of two phase III trials[98,99]. However, it does come with some additional benefits. TMZ is known to cross the blood brain barrier (BBB) due to its lipophilic properties, which DTIC is unable to do, meaning that TMZ has influence on melanoma brain metastases[97]. One study found a decrease from 43% to 10% in incidence of brain metastasis in melanoma patients treated with TMZ compared to DTIC[100]. TMZ is also delivered orally, rendering it far more convenient for patients[97]. Aside from DTIC and TMZ, several other single-agent chemotherapeutics from classes such as vinca alkaloids, taxanes, nitrosoureas and platinum compounds have been tested in melanoma; nevertheless, their response rates do not surpass that of DTIC or TMZ[95].

There are several types of immunotherapy drugs used in the treatment of melanoma some of which include nivolumab, ipilimumab and pembrolizumab. Nivolumab and pembrolizumab both work by targeting PD-1 as described in **Section 1.1.3**, whereas ipilimumab works by targeting the cytotoxic T-lymphocyte associated protein 4 (CTLA-4) receptor[101]. CTLA-4 is involved in inhibiting activation of T cells and their proliferation[101]. For T-cell activation to occur, T-cell receptors (TCRs) need to bind to the MHC I or II on antigen presenting cells (APCs)[101]. A co-stimulatory signal is then needed which is attained by the binding of B7-1 (or CD80) and B7-2 (or CD86), both found on APCs, to CD28 receptors present on T-cells[101,102,103]. During this process, T cells express CTLA-4 which binds to B7-1 and -2, stopping them from binding to CD28, thereby reducing T-cell activation[101,103]. Ipilimumab is a humanised mAb (much like nivolumab and pembrolizumab) that binds to CTLA-4, hence inhibiting the binding of B7-1 and -2 to CTLA-4, allowing for T-cell activation, proliferation and increased immunity[101,102,103]. Today it is also possible to treat advanced melanoma with combinations of immunotherapy drugs. For example, ipilimumab can be given in combination with nivolumab, after results from the phase III CheckMate 067 (NCT01844505) trial showed that nivolumab plus ipilimumab gave a higher response rate and longer PFS and overall survival (OS) compared to ipilimumab given alone for advanced melanoma[104,105].

Targeted therapy for melanoma mainly involves the use of drugs which target proteins BRAF and MEK, both integral to MAPK signalling. Vemurafenib is an example of a BRAF inhibitor which is selective for BRAF$^{V600E}$ mutations[106,107]. It is administered orally and its mechanism of action entails binding to the ATP-binding site of the BRAF$^{V600E}$ kinase, limiting its activity and subsequently suppressing overactivation of the MAPK pathway, hence reducing proliferation of cancer cells[106,107]. Vemurafenib was shown to better improve PFS and OS in melanoma patients with BRAF$^{V600E}$ mutations compared to standard DTIC therapy (OS was 84% for vemurafenib after 6 months and 64% for DTIC after 6 months)[108]. Cobimetinib is an example of a MEK inhibitor used in treatment of advanced melanoma[109]. It is also administered orally, and its mechanism of action involves inhibiting the MEK1 and MEK2 kinase enzymes in a reversible manner[110]. Cobimetinib is often given together with vemurafenib, after results from clinical trials

such as the phase III coBRIM study (NCT01689519) revealed longer PFS and OS in melanoma patients harbouring the BRAF$^{V600}$ mutations after the combination treatment versus single vemurafenib treatment[109,111,112]. Mouse models bearing BRAF$^{V600E}$ mutations also showed increased apoptosis and decreased tumour growth when cobimetinib was administered alongside vemurafenib[113].

**Table 3 – Common therapies used in the treatment of melanoma** (structures of chemotherapies and targeted therapies were drawn using ChemDraw; structures of PD-1 inhibitors were taken and adapted from Zhang *et al*, 2022[114]; structure of ipilimumab was taken and adapted from Ramagopal *et al*, 2017[115])

| Chemotherapy |
|---|
| Alkylating agents |



Dacarbazine (DTIC)

Temozolomide (TMZ)

| Immunotherapy |
|---|

| PD-1 inhibitors | CTLA-4 inhibitors |
|---|---|



Nivolumab

Pembrolizumab



| Targeted therapy |
|---|

| BRAF inhibitors | MEK inhibitors |
|---|---|



Vemurafenib

Cobimetinib

Although there are different therapies available to a melanoma patient, they are not always effective, relapse may occur and resistance to treatment can develop. For instance, melanoma resistance to BRAF inhibitors was and remains widespread, and one of the main motivations for the initial development of MEK inhibitors was to attempt to

mitigate this effect[109]. These types of problems highlight the need for discovery of novel drug targets in melanoma.

### 1.2.3 Chemoresistance

Chemoresistance describes the ability of cancer cells to bypass and survive anticancer treatments. It is a prevalent issue in cancer therapy; drug resistance is directly or indirectly responsible for 80-90% of cancer patient deaths[116]. Cancer cells can achieve chemoresistance by various mechanisms utilising transporter pumps, activation of oncogenes, mitochondrial alteration, epithelial-mesenchymal transition (EMT), cancer stem cells, the tumour microenvironment, autophagy, non-coding RNAs, inhibition of apoptosis and drug inactivation by way of example[117,118]. Multiple mechanisms can also occur at the same time and in certain cases, cancer is able to develop multi-drug resistance (MDR)[116,119]. Chemoresistance is divided into two groups: intrinsic resistance and acquired resistance[116]. Intrinsic resistance refers to resistance that exists prior to the administration of a drug, while acquired resistance refers to the development of resistance after drug exposure[120].

Melanoma has a variety of chemoresistance mechanisms [**Figure 6**][121]. The most prevalent of these involve drug efflux transporters which typically decrease drug accumulation in cancer cells. ATP-binding cassette (ABC) transporters are upregulated in melanoma in response to certain treatments and work by actively transporting drugs out of cells[121]. P-glycoprotein (P-gp) and multidrug-resistance-associated proteins (MRPs) are examples of two key groups of ABC transporters[121]. Of these, some of the ones found in melanoma include ABCB1 (also known as P-gp or MDR1), ABCC2, ABCB5 and ABCB8[121]. ABCC2 has been linked to cisplatin resistance whereas ABCB5 and ABCB8 have been linked to doxorubicin resistance[121,122,123,124]. In melanoma chemoresistance, expression of heat shock transcription factor 1 (HSF1) is also upregulated[121]. HSF1 is a protein that manages proteotoxic stress[125]. It is not an efflux transporter itself but rather a transcription factor that increases drug efflux capability via ABC transporters and is known to contribute to melanoma cell proliferation and survival[125,126].
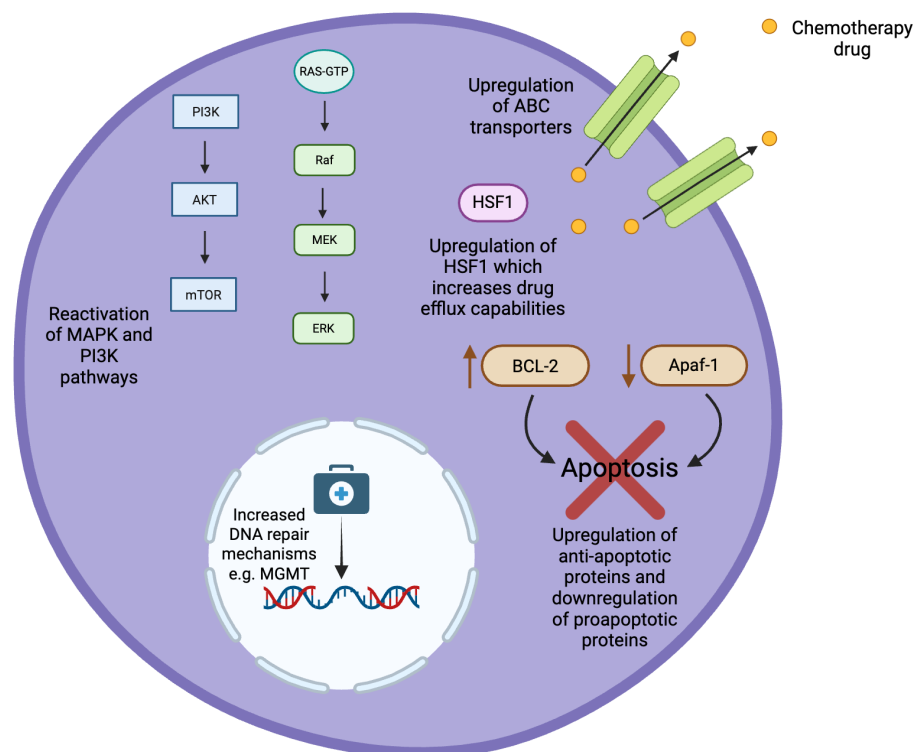
**Figure 6 – Mechanisms of chemoresistance commonly seen in melanoma.** Some of the chemoresistant mechanisms in melanoma include reactivation of MAPK and PI3K signalling pathways, upregulation of drug efflux transporters, HSF1 upregulation, increased DNA repair mechanisms and regulation of anti- and pro-apoptotic proteins. Abbreviations: Apaf-1, apoptotic protease activating factor 1; BCL-2, B-cell lymphoma-2; HSF1, heat shock transcription factor 1; MGMT, $O^6$-methylguanine-DNA methyltransferase (figure created in Biorender).

Drug resistance in melanoma can also be facilitated by modified DNA repair mechanisms[121,127]. Alkylating agents used in melanoma treatment cause $O^6$-chloroethylguanine DNA impairment through adducts which leads to interstrand DNA crosslinking, resulting in inhibition of DNA replication[121,127]. $O^6$-alkylguanine DNA alkyltransferase is an enzyme that repairs these adducts, reducing the cytotoxic activity of alkylating agents[128]. $O^6$-methylguanine-DNA methyltransferase (MGMT) is another enzyme that also participates in repair of DNA damaged by alkylating agents and its expression has been revealed to be elevated in melanoma[121,127,129]. Overall, in chemo-resistant melanoma cells, DNA repair is heightened. Apoptosis inhibition mechanisms are also seen in chemo-resistant melanomas; anti-apoptotic proteins such as BCL-2 are upregulated (see **Section 1.1.2**) whereas proapoptotic proteins such as APAF-1 are downregulated[121,130]. In addition to this, human double minute 2 (Hdm2), a ubiquitin ligase that negatively regulates p53 (which induces apoptosis [**Section 1.1.2**]), is also upregulated in melanoma[121].

In the case of BRAF inhibitor resistance seen in melanoma (mentioned in **Section 1.2.2**), microRNA-125a is known to play a role. Research shows that microRNA-125a expression is elevated in melanoma cells after acquiring resistance to BRAF inhibitors[131]. In

BRAF[V600E]-mutated melanomas, microRNA-125a inhibits pro-apoptotic proteins BAK1 and MLK3 in the cell intrinsic pathway[131]. Other mechanisms of chemoresistance include reactivating the MAPK and PI3K/AKT signalling pathways[131,132].

Many therapies for metastatic melanoma fail due to different chemoresistance mechanisms. Although treatment can be improved in some cases with combinations of drugs (such as BRAF inhibitors and MEK inhibitors), more research in this area is required. New mechanisms of chemoresistance are continually being discovered, meaning that new targets for overcoming these mechanisms must also be sought. One such emerging interest is in the protein DJ-1, a sensor of oxidative stress that has been reported to increase chemoresistance in certain cancers and may have potential as a therapeutic target for melanoma[133].

## 1.3 DJ-1

### 1.3.1 An introduction to DJ-1

DJ-1, also known as PARK7, is a Parkinson's disease (PD)-associated protein belonging to the DJ-1/ThiJ/PfpI superfamily of proteins[134]. It has a molecular weight of 20kDa, is composed of 189 amino acids and has a dimeric structure consisting of $\alpha$-helices and $\beta$-sheets [**Figure 7**]. Its conformation is comprised of a 6-stranded $\beta$-sheet (parallel), enclosed by $\alpha$-helices, a $\beta$-hairpin, and a 3-stranded $\beta$-sheet (antiparallel)[135]. The Cys106 residue is particularly critical for DJ-1 function and homodimer formation, although it is also thought that the Leu166 residue may likewise be critical for homodimer formation [**Figure 7**][135,136,137].
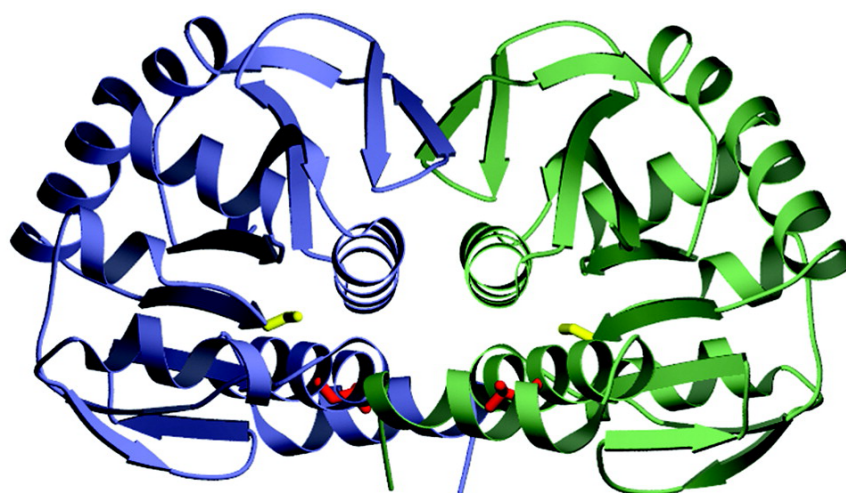


**Figure 7 – DJ-1 crystallographic dimer.** The dimeric structure of DJ-1 as an active unit is made up of $\alpha$-helices and $\beta$-sheets. One monomer/subunit is shown in blue, the other in green. The critical Cys106 residue is shown in yellow and the critical Leu166 residue is shown in red (image taken and adapted from Wilson *et al*, 2003[135]).

DJ-1 has a wide range of functions which include regulating transcription, apoptosis, autophagy, chaperones, mitochondrial function and the inflammatory response[138]. However, its most recognised function is in protecting cells against oxidative stress, earning it the title of an oxidative stress sensor[139]. Under oxidative stress conditions, the Cys106 residue in DJ-1 is oxidised to sulfinate ($-SO_2H$) and sulfonate ($-SO_3H$) forms, causing DJ-1 to move into the mitochondria from the cytoplasm (where it is usually found under normal conditions)[138,140]. This process allows for the antioxidant function of DJ-1 to take effect, eliminating reactive oxygen species (ROS) (acting as a scavenger), and essentially, the extent of oxidation that occurs at the Cys106 residue dictates the activity of DJ-1[140]. When regulating transcription, DJ-1 acts as a transcriptional co-activator[141]. It binds non-covalently to different transcription factors including androgen receptor, signal transducer and activator of transcription 1 (STAT1), nuclear receptor related 1 protein (NURR1) and sterol regulatory element-binding protein (SREBP)[141]. DJ-1 can also move from the cytoplasm to the nucleus of cells during the cell cycle process following mitogen stimulation, modulating gene transcription of human tyrosine hydroxylase (TH) (important for dopamine biosynthesis) and thioredoxin-1 (Trx1)[141].

In addition to the functions already mentioned, DJ-1 has also been reported to possess some enzymatic activity[138] [**Table 4**]. Until recently, DJ-1 was controversially considered as a deglycase; however, new investigations have demonstrated that this characterisation is not entirely accurate, as DJ-1 can also operate as a glutathione (GSH)-independent glyoxalase[142,143]. DJ-1 deglycase activity involves repairing glyoxal- and methylglyoxal-glycated amino acids and proteins via targeting early glycation intermediates, releasing the restored proteins along with glycolate or lactate[144]. On the other hand, DJ-1 glyoxalase activity involves detoxifying carbonyl compounds, for example, DJ-1 coverts glyoxal and methylglyoxal into glycolate and D-lactate[145]. Discourse over DJ-1 glycation repair mechanisms persists; yet it is unequivocal that evidence demonstrates DJ-1 can exhibit both deglycase and glyoxalase enzymatic activities[141]. In dopaminergic cells, DJ-1 undergoes proteolytic conversion to a protease, leading to increased antioxidant activity against oxidative stress caused by apoptosis[146]. Once the DJ-1 protease is active, it establishes a caspase-like catalytic couplet between the critical Cys106 residue and a His126 residue[146]. DJ-1 also exhibits esterase activity[141].

**Table 4 – Functions of DJ-1** (adapted from Sun and Zheng, 2023[141])

| DJ-1 functions | |
|---|---|
| **Non-enzymatic** | **Enzymatic** |
| • Transcriptional co-activator<br>• Oxidative stress sensor<br>• Detoxification | • Deglycase<br>• Glyoxalase<br>• Protease<br>• Esterase<br>• Scavenger |

Since DJ-1 has roles in various cellular mechanisms, it is naturally implicated in distinct signalling pathways. For instance, DJ-1 is known to activate the PI3K signalling pathway and the extracellular signal-regulated kinase 1/2 (ERK1/2) signalling pathway, both of which respond to oxidative stress stimuli[147]. It also activates the nuclear factor erythroid 2-related factor 2 (Nrf2) signalling pathway, a cellular defence mechanism against oxidative stress (see **Section 1.3.2** below)[138].

*1.3.2 Nrf2, a downstream target of DJ-1*

Nuclear factor erythroid 2-related factor 2 (Nrf2) is a transcription factor belonging to the Cap 'N' Collar (CNC) family of basic leucine zipper transcription factors[148]. It is recognised as a 'master regulator' of oxidative stress since it controls transcription of genes with anti-inflammatory, cytoprotective and detoxification capabilities, protecting cells against oxidative stress[149,150]. Nrf2 is controlled by its negative regulator, Kelch-like ECH-associated protein 1 (Keap1), which binds to the Neh2 domain associated with ETGE and DLG motifs[149,151]. This causes polyubiquitination of Nrf2 and degradation through the 26S proteasome[150,152]. Beta-transducin repeat-containing proteins (β-TrCP) are involved in Nrf2 polyubiquitination, serving as adapters for Cullin-1 E3 ubiquitin ligase[153,154,155]. Nrf2 has a high turnover rate and short half-life of 10-30 minutes[156].

Under normal cellular conditions, Nrf2 is inactive through its interaction with Keap1 and subject to degradation[151]. When oxidative stress conditions present, the Nrf2/Keap1 interaction is disrupted, allowing Nrf2 to accumulate and translocate into the nucleus[151]. DJ-1 acts on the Nrf2 pathway by interrupting the Nrf2/Keap1 interaction [**Figure 8**][137,138,140]. Once in the nucleus, Nrf2 forms a heterodimer with sMaf proteins and binds to the antioxidant response element (ARE) on DNA, which triggers transcription of various target cytoprotective, antioxidant and detoxification genes[138,150]. Some examples of these target genes include antioxidants heme oxygenase-1 (HO-1) and thioredoxin-1 (Trx1) and the Phase II detoxification enzyme, NAD(P)H quinone dehydrogenase 1 (NQO1)[157].
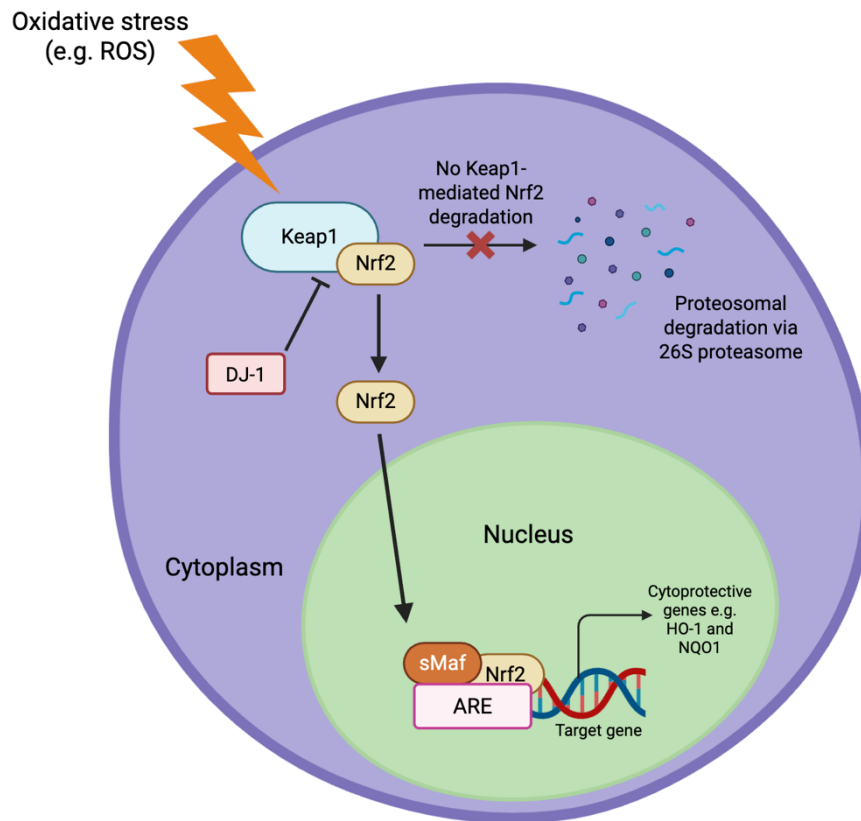
**Figure 8 – The role of DJ-1 in the Nrf2 signalling pathway.** DJ-1 inhibits the interaction between Nrf2 and Keap1, which triggers Nrf2 to accumulate in the nucleus and bind with sMaf protein to the ARE to initiate transcription of various cytoprotective genes. As a result of this inhibition, Nrf2 avoids Keap1-mediated degradation via the 26S proteasome. Abbreviations: ARE, Antioxidant Response Element; Nrf2, Nuclear factor erythroid 2-related factor 2; sMaf, small musculoaponeurotic fibrosarcoma proteins (figure created in Biorender).

Nrf2 is also known to be involved in cancer progression and chemoresistance[149]. Overexpression of Nrf2 in various cancers including colon and breast has been linked to poor prognosis in patients and resistance to chemotherapy treatment[158,159,160]. Nrf2 has also been found to be overexpressed in melanoma[161,162]. The mechanisms underlying Nrf2's role in cancer are complex and often rooted in the 'hallmarks of cancer'[149]. One way that Nrf2 aids in cancer progression is through promoting cell proliferation[163]. It enhances expression of genes associated with cell proliferation such as insulin-like growth factor 1 (IGF1), vascular endothelial growth factor C (VEGFC) and NOTCH1[149]. Nrf2 activation can also be influenced by the PI3K signalling pathway which regulates cell proliferation[164]. Another way that Nrf2 facilitates cancer progression is by promoting cell evasion of apoptosis[149]. Nrf2 does this by inducing expression of anti-apoptotic proteins BCL-2 and B-cell lymphoma-extra large (BCL-xL) and decreasing pro-apoptotic expression of BAX[149,165]. Furthermore, Nrf2 protects cancer cells against oxidative stress (via promoting expression of various cytoprotective genes), allowing for cancer cell survival[158].

Since Nrf2 is implicated in cancer and chemoresistance, it has become an attractive therapeutic target. Inhibitors of Nrf2 have been proposed as potential novel therapies for melanoma and other cancers. Several plant-derived natural products inhibit Nrf2, including triptolide, brusatol, luteolin, and retinoic acid[166,167]. In addition, small molecules including clobetasol and ML-385 have also been reported to inhibit it[168]. Nevertheless, none of these are employed in clinical settings yet[167,168].

### 1.3.3 DJ-1 in Parkinson's Disease

Although DJ-1 has protective roles in cells, it may also be considered a double-edged sword due to its involvement in the pathogenesis of certain diseases. It is most known for contributing to Parkinson's disease, through loss of function mutations, but is additionally implicated in other neurodegenerative diseases, and in cardiovascular diseases and cancer[137,146].

Parkinson's disease (PD) is a chronic neurodegenerative disease which mainly affects the elderly[169]. Key symptoms of this disease include repression of voluntary movements (termed bradykinesia), muscle rigidity, tremor at rest and a varying degree of cognitive impairment[169,170]. The pathophysiology of PD is associated with the degeneration or loss of dopaminergic neurons in the *substantia nigra* part of the brain and also with aggregation of α-synuclein Lewy bodies[171,172].

Loss of function of DJ-1 is associated with PD. This link was first discovered in 2003 by Bonifiati and his colleagues[173]; they discovered a missense mutation and substantial deletion in the DJ-1 gene which then led to the characterisation of DJ-1 as a novel gene for early onset autosomal recessive PD[173]. As a result of this discovery, DJ-1 is now considered a potential biomarker for PD. Furthermore, certain mutations in DJ-1 have been shown to interfere with the dimeric structure of DJ-1, leading to its inactivation in PD[135,174]. DJ-1 loss of function mutations are associated with neuroinflammation, oxidative stress-induced cell death, dysfunction of mitochondria, hindered autophagy, increased α-synuclein aggregation and decreased levels of dopamine neurotransmitter in PD[174,175,176]. These findings indicate that DJ-1 could be a potential therapeutic target in PD.

### 1.3.4 DJ-1 in cancer

DJ-1 is also known to play a role in carcinogenesis. DJ-1 overexpression has been observed in multiple cancer types, some of which include lung, brain, breast, thyroid, pancreatic, and melanoma (including uveal) [133,177,178]. This suggests that DJ-1 could be beneficial as a biomarker for cancer. Data obtained from the Gene Expression Profiling Interactive Analysis (GEPIA) web server[179], as displayed in **Figure 9**, demonstrates that

DJ-1 is overexpressed more than twofold in thymoma (THYM), skin cutaneous melanoma (SKCM), pancreatic adenocarcinoma (PAAD) and lymphoid neoplasm diffuse large B-cell lymphoma (DLBC) samples compared to their paired normal tissues. Interestingly, the opposite is seen in acute myeloid leukaemia (LAML) samples relative to their paired normal tissues. This discovery of DJ-1 overexpression in SKCM suggests that DJ-1 may play a role in melanoma development and progression, which is an aspect that this project intends to explore.
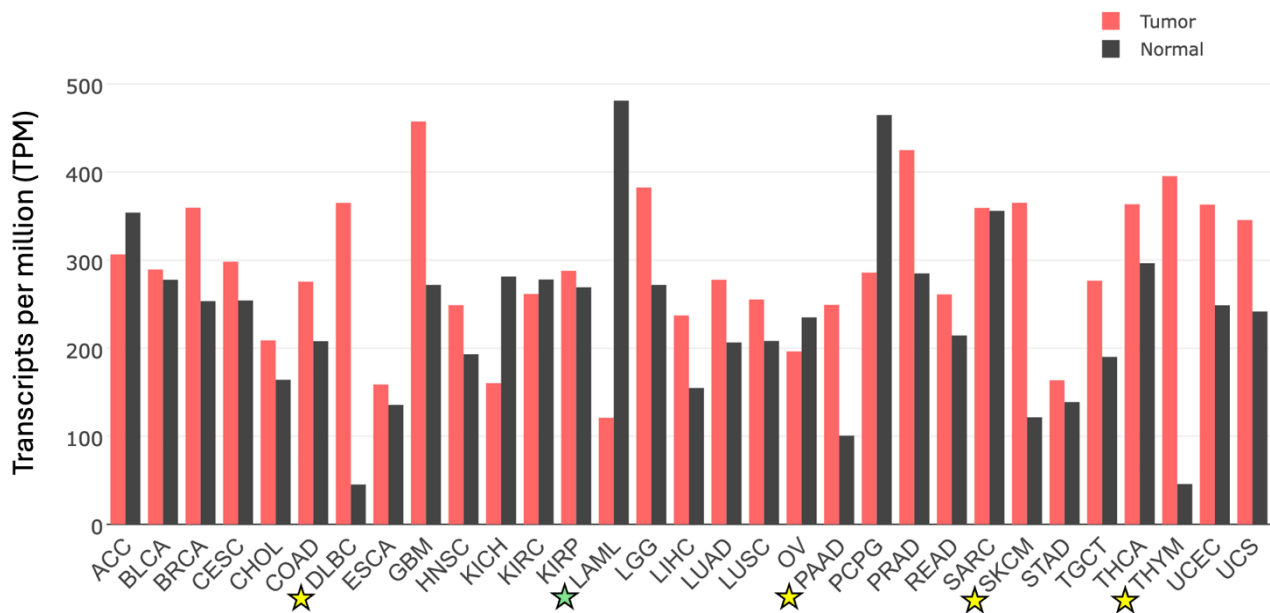


**Figure 9 – DJ-1/PARK7 gene expression profile across all tumour samples and paired normal tissues from the GEPIA RNA expression data bank.** Yellow stars indicate DJ-1 overexpression in tumour samples whereas green stars indicate DJ-1 overexpression in normal tissue samples. Cancer abbreviations: ACC, Adrenocortical carcinoma; BLCA, Bladder Urothelial Carcinoma; BRCA, Breast invasive carcinoma; CESC, Cervical squamous cell carcinoma and endocervical adenocarcinoma; CHOL, Cholangial carcinoma; COAD, Colon adenocarcinoma; DLBC, Lymphoid Neoplasm Diffuse Large B-cell Lymphoma; ESCA, Esophageal carcinoma; GBM, Glioblastoma multiforme; HNSC, Head and Neck squamous cell carcinoma; KICH, Kidney Chromophobe; KIRC, Kidney renal clear cell carcinoma; KIRP, Kidney renal papillary cell carcinoma; LAML, Acute Myeloid Leukaemia; LGG, Brain Lower Grade Glioma; LIHC, Liver hepatocellular carcinoma; LUAD, Lung adenocarcinoma; LUSC, Lung squamous cell carcinoma; OV, Ovarian serous cystadenocarcinoma; PAAD, Pancreatic adenocarcinoma; PCPG, Pheochromocytoma and Paraganglioma; PRAD, Prostate adenocarcinoma; READ, Rectum adenocarcinoma; SARC, Sarcoma; SKCM, Skin Cutaneous Melanoma; STAD, Stomach adenocarcinoma; TGCT, Testicular Germ Cell Tumours, THCA, Thyroid carcinoma; THYM, Thymoma; UCEC, Uterine Corpus Endometrial Carcinoma; UCS, Uterine Carcinosarcoma (figure generated from the Gene Expression Profiling Interactive Analysis (GEPIA) web server, which was developed by Tang *et al*, 2017[179]).

Aside from the GEPIA web server data, it is worth noting that an inverse relationship between PD and lung cancer has been suggested and PD patients have a 44% reduced risk of developing lung cancer[180].

DJ-1 may promote cancer progression through several mechanisms. One of the main ways it does this is through its protective role as an oxidative stress sensor; DJ-1 protects cancer cells against oxidative stress insults via the Nrf2 signalling pathway [**Figure 10**][181]. Its mechanism of action is the same as described in **Section 1.3.2**; DJ-1 activates Nrf2 which is also overexpressed in various cancers. Furthermore, DJ-1 promotes cancer cell survival and even chemoresistance by detoxifying drugs and upregulating drug efflux pumps including ABC transporters via its regulation of proteins such as Nrf2[133,182].

Another way that DJ-1 facilitates cancer progression is through repressing apoptosis of cancer cells[182]. As discussed in the **Section 1.2.1**, PTEN is a tumour suppressor which inhibits PI3K signalling by dephosphorylating phosphatidylinositol (3,4,5)-triphosphate ($PIP_3$) to phosphatidylinositol (4,5)-bisphosphate ($PIP_2$), inhibiting AKT activation. Without PTEN, the PI3K pathway is continuously activated, allowing cancer cells to proliferate and evade apoptosis. DJ-1 acts as an oncogene and inhibits PTEN expression, thereby enabling cancer cell survival due to apoptosis evasion[133,182]. Furthermore, DJ-1 can additionally regulate MAPK signalling, specifically the mitogen-activated protein kinase/extracellular signal-regulated kinase 1 (MEKK1-SEK1-JNK1) pathway, resulting in reduced oxidative stress induced-apoptosis[133,183]. c-Jun N-terminal kinase 1 (JNK1) is a protein kinase acting downstream of this pathway and plays a role in inducing apoptosis[133,184]. It phosphorylates proapoptotic proteins Bad and BCL-2 interacting mediator of cell death (Bim) which interact with anti-apoptotic protein, BCL-2[185,186]. Bad and Bim bind to the BH3 domain of BCL-2, neutralising its capacity to prevent apoptosis[187,188,189]. DJ-1 is known to inhibit JNK1 activation by binding to MEKK1, isolating it in the cytoplasm, rendering MEKK1 unable to trigger the cascade which leads to JNK1 activation[133]. This allows cancer cells to avoid apoptosis.

DJ-1 can also sequester death domain associated protein (Daxx) in the nucleus and inhibit cytoplasmic stress-responsive effector apoptosis signal-regulating kinase 1 (ASK1) activation, which triggers apoptosis through activating JNK and p38[133]. ASK1 is usually bound to thioredoxin-1 (Trx1), however under oxidative stress conditions, ASK1 dissociates from Trx1 which leads to apoptosis[190]. DJ-1 inhibits ASK1 dissociation from thioredoxin-1 (Trx1), therefore inhibiting apoptosis[191].
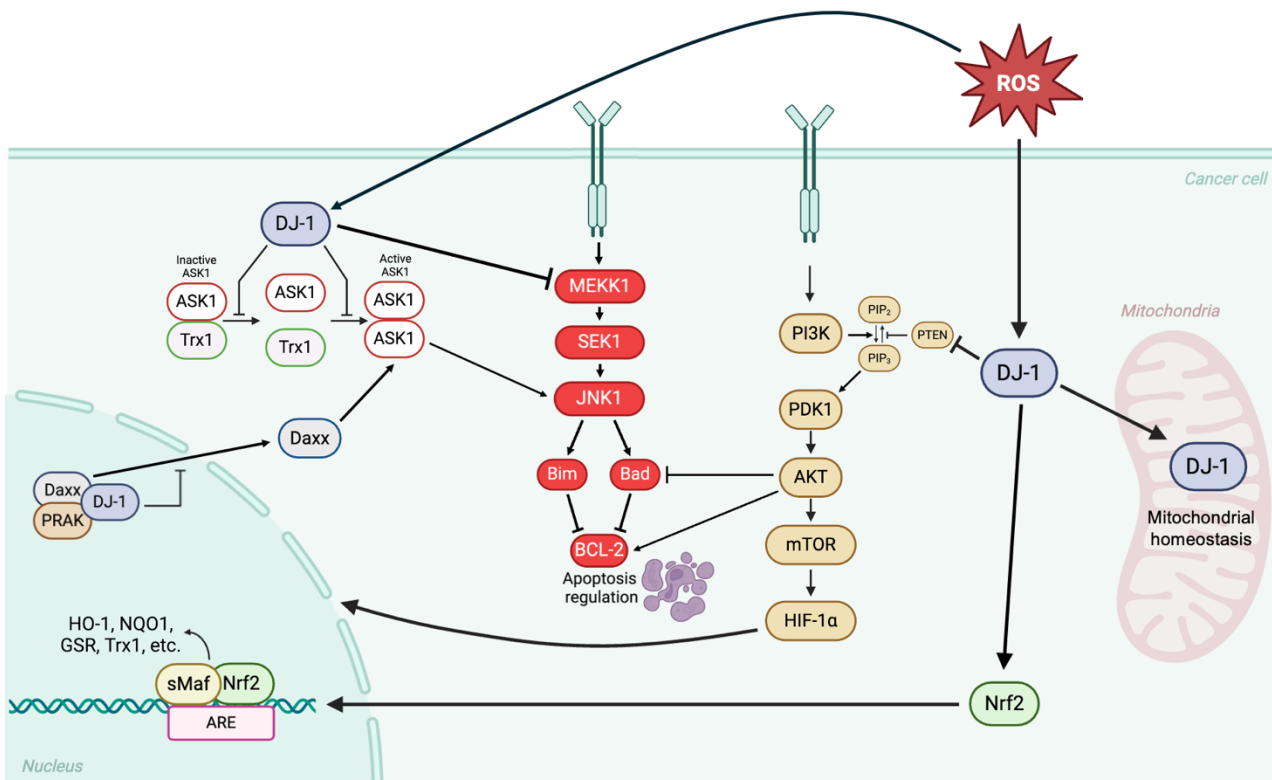
**Figure 10 – Key signalling pathways and interactions of DJ-1 in cancer.** Oxidative stress activates DJ-1 causing it to interact with the Nrf2 pathway, leading to production of cytoprotective genes, protecting the cancer cell. Activated DJ-1 translocates into the mitochondria where it plays an antioxidant role in mitochondrial homeostasis. DJ-1 also inhibits PTEN in the PI3K pathway, meaning that the pathway is continuously activated, allowing the cancer cell to proliferate and evade apoptosis. DJ-1 also inhibits apoptosis of cancer cells by sequestering Daxx in the nucleus and inhibiting MEKK1 activity. Furthermore, DJ-1 inhibits ASK1 activation which leads to a decrease in JNK activation and therefore apoptosis (figure adapted from Biorender).

Another potential way that DJ-1 promotes cancer progression is by allowing cancer cells to adapt to hypoxic conditions[133]. Hypoxia inducible factor 1 subunit alpha (HIF-1$\alpha$) is a protein that regulates cell response to oxygen and acts downstream of the PI3K pathway[192]. In cancer, HIF-1$\alpha$ enables cancer cells to bypass the constraints imposed by hypoxic conditions through promoting angiogenesis and upregulating glycolytic enzymes, allowing cancer cells to generate energy effectively with restricted available oxygen[193,194]. It also promotes growth, metastasis and survival; for example, it allows for invasion of cancer cells and in certain cases promotes chemoresistance[193,194]. In colorectal cancer, DJ-1 increases HIF-1$\alpha$ expression[143]. Vasseur and colleagues (2009)[195] also found that DJ-1 knockdown in osteosarcoma cells decreased HIF-1$\alpha$ expression. They also discovered that DJ-1 is essential for AKT and mTOR activity both of which enhance stability of HIF-1$\alpha$. Therefore, since DJ-1 regulates PI3K signalling, it also regulates HIF-1$\alpha$ expression.
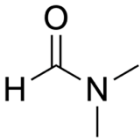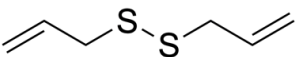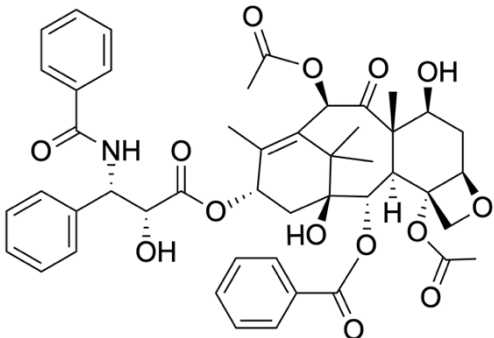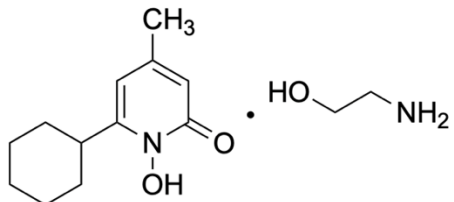
DJ-1 can also encourage epithelial to mesenchymal transition (EMT) through the Wnt signalling pathway and regulate the androgen receptor (AR) signalling pathway which plays a role in prostate cancer[133,196]. Furthermore, there is evidence that DJ-1 regulates non-canonical NF-κB signalling. In cancer, NF-κB allows for cell survival, growth and evasion of apoptosis, and DJ-1 has been found to control nuclear localisation of NF-κB through inhibiting cellular zinc finger anti-NF-κB (Cezanne)[133,197].

All the evidence discussed clearly demonstrates that DJ-1 is implicated in cancer progression and has functions in cell proliferation, survival, metastasis and even chemoresistance. This further indicates and suggests that DJ-1 could be a promising target for cancer therapy, and research is already underway in this area (see **Section 1.3.5**).

*1.3.5 Approaches to targeting DJ-1 in cancer*

Potential ways of targeting DJ-1 in cancer include inhibiting DJ-1 homodimer formation, disrupting its protein function or inhibiting DJ-1 expression by altering transcription or translation mechanisms[198]. DJ-1 expression can be inhibited by utilising siRNA, short-hairpin RNA (shRNA) or RNA interference (RNAi) mechanisms[198]. Studies involving the use of RNAi targeting DJ-1 in various cancers have been conducted, with many showing anti-tumour effects, however more research into safety and delivery efficiency is still needed[198]. Aside from RNAi technologies, several drug candidates targeting DJ-1 expression have also been studied [**Table 5**]. For instance, dimethyl fumarate (DMF) which is derived from fumaric acid, has shown some anti-tumour activity in cancers such as lung and melanoma, and has now been found to decrease DJ-1 expression in colorectal and ovarian cancer cells[182,199,200,201]. Paclitaxel, a common chemotherapy drug, was discovered to decrease DJ-1 expression in breast cancer cells, and diallyl disulfide (DADS) was found to decrease DJ-1 expression in leukaemia cells[182]. Ciclopirox olamine (CPX) which is used to treat fungal infections has also been confirmed to supress DJ-1 expression in colorectal cancer cells, causing increases in ROS and disrupting mitochondrial function[182].

**Table 5 – Drug candidates targeting DJ-1 expression in various cancers** (structures of drug candidates were drawn using ChemDraw)

| Drug candidate | Structure | Effect on DJ-1 expression in specific cancer type(s) |
|---|---|---|
| Dimethyl fumarate (DMF) | | Decreases DJ-1 expression in colorectal and ovarian cancer cells[199] |
| Diallyl disulfide (DADS) | | Decreases DJ-1 expression in leukaemia cells[202] |
| Paclitaxel | | Decreases DJ-1 expression in breast cancer cells[182] |
| Ciclopirox olamine (CPX) | | Decreases DJ-1 expression in colorectal cancer cells[203] |

As mentioned briefly in **Section 1.3.3**, certain mutations in DJ-1 have been shown to disrupt the dimeric structure of DJ-1 in PD, leading to its inactivation. These mutations cause DJ-1 to lose its antioxidant function[204]. Therefore, inhibiting DJ-1 homodimer formation in cancer cells could also possibly provide some anti-tumour effects, as functioning DJ-1 protects cancer cells against oxidative stress (see **Section 1.3.4**). Various isatin (1H-indole-2,3-dione) derivatives have been designed which specifically target the critical Cys106 residue of DJ-1 (which is responsible for the antioxidant function of DJ-1), disrupting the dimeric structure of DJ-1 and inhibiting its protein function[136]. Tashiro *et al* (2018)[136] reported that these compounds inhibited the guanine and deglycase detoxifying activities of DJ-1. Even though these compounds were designed to target DJ-1 in PD, they may also be beneficial in a cancer setting, as it is thought that high glycation levels can correlate with DJ-1 overexpression, and that DJ-1 deglycase activity plays a role in promoting cancer cell survival[133]. Chen *et al* (2021)[205] tested one of the isatin derivatives called 5-fluoro-1-(2-phenylethyl)-1H-indole-2,3-dione (also known as

STK793590) [**Figure 11**] for anticancer activity in mice injected with human lung cancer cells and found that STK793590 inhibited tumour growth. They also designed another STK-derived compound called 1,1'-(Decane-1,10-diyl)bis(5-fluoroindoline-2,3-dione) (also known as DM10) [**Figure 11**], which showed higher inhibition of tumour and cancer cell growth compared to STK793590. These results are promising and support the evidence that DJ-1 is involved in cancer progression. Previous work in the O'Connell lab involved testing STK793590 in human skin melanoma cell lines and found mild inhibitory effects on cell proliferation. This project aims to further extend this research with drug combination experiments both in 2D and 3D models of melanoma.
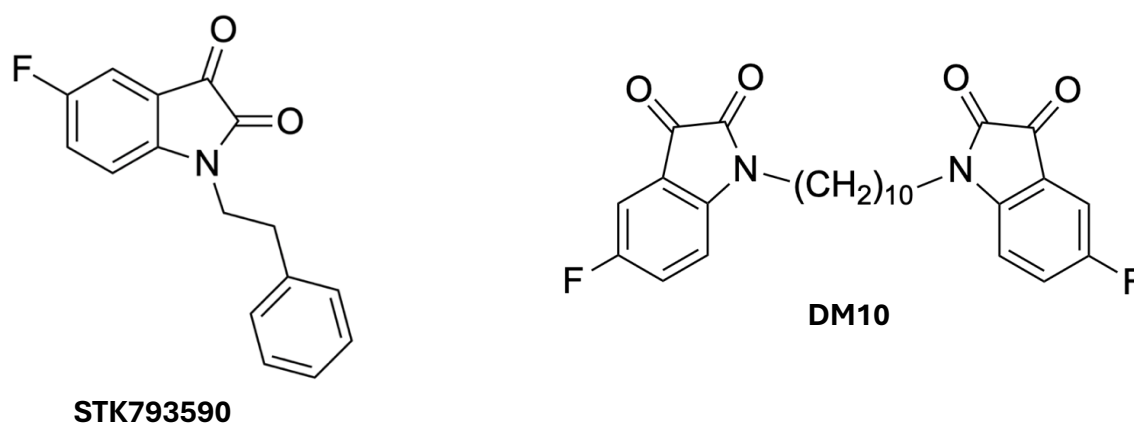


**STK793590**

**DM10**

**Figure 11 – Structures of STK793590 and DM10.** STK793590 has a molecular weight of 268.11 g/mol and DM10 has a molecular weight of 470.49 g/mol (structures were drawn using ChemDraw).

*1.3.6 DJ-1 in melanoma*

In light of the above, it is unequivocal that DJ-1 is involved in cancer progression. Nevertheless, research concerning DJ-1 in relation to melanoma is limited. As mentioned previously in **Section 1.3.4**, there is some evidence that DJ-1 may be overexpressed in melanoma, suggesting that there is some involvement of DJ-1 in the pathophysiology of melanoma, yet investigations into the potential mechanisms underlying this involvement are sparse. DJ-1 has been studied in uveal melanoma[178,206]; however, less investigations have been conducted in skin melanoma, emphasising a need for novel discoveries in this particular area. Previous work in the O'Connell lab has explored DJ-1 expression in various cancer cell lines and found DJ-1 to be overexpressed in a panel of human skin melanoma cell lines. Effects of DJ-1 knockdown using siRNA and targeted peptides was explored in 2D cell models. The research conducted for this project extends this work to further explore the role of DJ-1 in cancer and broaden into 3D models of melanoma.

*1.3.7 Melanoma tissue models for drug discovery*

Studying potential drug targets such as DJ-1 in various tissue models is warranted to gain a better understanding of diseases such as melanoma. Melanoma *in vitro* and *in vivo* tissue models are essential for discovery and translational research in the development of cutting-edge therapeutics. They improve our understanding of melanoma by allowing closer study of signalling pathways, leading to novel target discoveries and better predictions of therapeutic mechanisms of action and response[207]. *In vitro* melanoma models can include 2D cell culture, 3D cell culture, *ex vivo* models, melanoma-on-a-chip, or patient-derived xenografts[208]. *In vivo* melanoma models involving animals can include xenograft, syngeneic or genetically engineered mouse models[207,208]. Melanoma can also be modelled using non-murine models, such as zebrafish or xenopus, allowing for high-throughput *in vivo* screening[207,209,210]. The research presented here involved studying DJ-1 in a 3D *in vitro* melanoma model as well as in a 2D *in vitro* model.

A common type of lab model used in melanoma research is a 2D *in vitro* model[208]. Different melanoma cell lines can be cultured separately or in co-culture with other cell types as monolayers in flasks[208]. The cells are passaged and used in various experiments. High-throughput screening, repeatability, ease of use, and affordability are some advantages of 2D models[208]. This project utilised 2D melanoma models which were generated using the A375 human skin melanoma cell line. Aside from 2D *in vitro* melanoma models, 3D *in vitro* melanoma models are becoming increasingly popular. This type of model enables the formation of complex, 3D structures of melanomas which more accurately mimic *in vivo* tissue structure, behaviour and the tumour microenvironment due to the presence of extracellular matrix elements[208,211]. They also provide a more ethical alternative to using animal models[211]. In comparison to 3D cell culture, 2D cell culture has limitations. For example, 2D cell culture is not fully representative of the cell environment due to lack of extracellular matrix elements, not as physiologically relevant and differences in drug bioavailability and resistance can be seen[208,211]. On the other hand, 3D tissue culture can facilitate enhanced cell-cell interactions across multiple dimensions and allow for improved prediction of drug activity[211].

There are different types of 3D model methods used in melanoma research; however common ones include generating 3D structures or tumouroids from melanoma cell lines or resected melanomas via the 'hanging drop' method, low or non-adherent methods or the 3D basement membrane method[208,212,213]. The 'hanging drop' method involves suspending cells in small drops of media on the underside of a petri dish lid[211,214]. Gravity causes the cells to aggregate and form 3D structures naturally. Low or non-adherent methods involve growing cells in specially designed plates (such as ultra-low adherence plates, also known as ULA plates) with a surface that reduces adhesion of cells, forcing the cells to aggregate together and form spheroids[212,215]. These plates replicate the way

cells naturally cluster in tissues. The 3D basement membrane method involves seeding cells in a basement membrane containing components such as collagen, laminin, fibronectin and growth factors[211,216]. Matrigel Matrix is an example of a basement membrane used in 3D models[208,212,216]. This technique allows for spontaneous formation of tumouroids when culturing any type of cancer cells. All three methods discussed here were investigated as part of this project.

**1.4 Aims**

1. Study the intracellular expression and role of DJ-1 in a 2D *in vitro* model of A375 melanoma cells using siRNA technology and a DJ-1 inhibitor.

2. Develop and optimise 3D *in vitro* models of A375 melanoma cells to study DJ-1 function more closely and examine their advantages and disadvantages for use in the lab.

3. Test an inhibitor targeting DJ-1 in the most appropriate 3D *in vitro* melanoma model chosen from Aim 2.

# 2. Materials and Methods

## 2.1 Reagents

### 2.1.1 General reagents

Dimethylsulfoxide (DMSO) and staurosporine were purchased from Sigma Aldrich (Dorset, UK). STK793590 (5-fluoro-1-(2-phenylethyl)-1H-indole-2,3-dione)[136] was synthesised in Professor Mark Searcey's lab (School of Chemistry, Pharmacy and Pharmacology, University of East Anglia, UK). Vemurafenib was obtained from Tocris Bio-techne (Bristol, UK) and hydrogen peroxide ($H_2O_2$) was obtained from Thermo Fisher Scientific. All consumables and any other reagents and solvents were obtained from Thermo Fisher Scientific, unless stated differently.

## 2.2 Cell culture

### 2.2.1 Cell media preparation

RPMI-1640 and phosphate buffered saline (PBS) were purchased from Sigma-Aldrich. L-Glutamine, penicillin streptomycin and heat-inactivated foetal bovine serum (FBS) were obtained from Gibco (Leicestershire, UK). Cell culture media (RPMI-1640) was supplemented with 10% fetal bovine serum (FBS), 100 U/mL penicillin, 100 µg/mL streptomycin and 2 mM L-glutamine. Completed media was stored at 4 °C.

### 2.2.2 Cell lines and passaging

A375 cells were obtained from the European Collection of Authenticated Cell Cultures (ECACC, Salisbury, UK) whereas MEL501, SK-MEL-28 and UACC 1273 cell lines were kindly supplied by Dr Antoni Ribas (University of California Los Angeles, USA). All cells were washed in phosphate buffered solution (PBS), detached with TrypLE Express and sustained and passaged in T75 tissue culture flasks as described in **Table 6**. The cells were maintained at 37 °C and 5% $CO_2$ in a humidified environment. Cell culture media and PBS were pre-warmed to 37 °C before use. TrypLE Express (Gibco, Leicestershire, UK) was kept at room temperature.

**Table 6 – Cell line culture conditions**

| Cell line | Origin | Mutations | Culture media | Adherent (Yes/No) | Passage procedure |
|---|---|---|---|---|---|
| A375 | Malignant epithelial melanoma cells obtained from a 54-year-old female | BRAF$^{V600E}$ | RPMI-1640 | Y | Passaged every 3-4 days in a 1:20 dilution once at 70-80% confluency |
| MEL501 | Malignant melanoma cells obtained from a female patient | BRAF$^{V600E}$ NRAS | RPMI-1640 | Y | Passaged every 3-4 days in a 1:5 dilution once at 70-80% confluency |
| UACC 1273 | Malignant melanoma cells obtained from a 54-year-old female | BRAF$^{V600E}$ | RPMI-1640 | Y | Passaged every 3-4 days in a 1:10 dilution once at 70-80% confluency |
| SK-MEL-28 | Malignant melanoma cells obtained from a 51-year-old male | BRAF$^{V600E}$ NRAS | RPMI-1640 | Y | Passaged every 3-4 days in a 1:20 dilution once at 70-80% confluency |

*2.2.3 Cell counting*

Cell density was established by counting with a Neubauer hemocytometer (Thermofisher). 10 μL of cell suspension was loaded into the counting chamber and the hemocytometer was inspected under light microscopy. An average was taken of the total number of counted cells in all four of the large squares of the hemocytometer. The cell density was then calculated using this equation:

Cell density (cells/mL) = Average cell count x 10,000

*2.2.4 Freezing cells*

Freezing media consisting of 10% DMSO Hybri-Max™ (Sigma-Aldrich) in FBS was made and kept on ice. Cells were detached using TrypLE Express once they were 70-80% confluent and then centrifuged at 1200 rpm for 5 mins. The supernatant was removed, and the cell pellet was resuspended in 1 mL of cold freezing media. The resulting suspension was then transferred into a sterile cryovial and briefly kept on ice before freezing gradually in a cotton wool packed box at -80 °C. Cryovials were then transferred to liquid nitrogen storage.

*2.2.5 Defrosting cells*

Cryovials with cells were defrosted at room temperature and then centrifuged at 2000 rpm for 5 mins. Following this, the supernatant was discarded, and the cell pellet was resuspended in 8 mL of appropriate media which was pre-warmed to 37 °C. The cell suspension was then moved to a T25 flask and cultured at 37 °C and 5% $CO_2$ in a humidified environment. Once the cells were 70-80% confluent, they were detached with

TrypLE Express and transferred into a T75 flask, where they were maintained at 37 °C and 5% $CO_2$ in a humidified environment. The cells were then passaged as normal as explained in **Table 6**.

## 2.3 Immunofluorescence

### 2.3.1 General DJ-1 antibody staining protocol

A375 cells were seeded onto glass coverslips (sterilised in 70% ethanol) in 12-well plates at a density of $1x10^5$ cells/mL and left to incubate overnight at 37 °C and 5% $CO_2$. Following this, the media was removed, and the cells were washed twice in 1 mL of ice-cold PBS. 0.5 mL of 4% paraformaldehyde (PFA) in PBS was then added to the cells and the plate was put on ice and put into the fridge for 1 h at 4 °C. After this, the PFA was removed, and the wells were washed twice in 1 mL of PBS. Next, 400 μL of 0.1% Triton X-100 in PBS was added to each well and the plate was left to rest at room temperature for 30 mins. The Triton X-100 was then removed, and the wells were washed twice in 1 mL of PBS. The primary antibody (rabbit anti-human DJ-1, Cell Signaling Technology, London, UK) was diluted 1:100 and 400 μL was added to the correct wells on the plate. 400 μL of PBS was added to all the other wells. The plate was then incubated at 4 °C overnight. The following day the plate was taken out of the fridge and all the wells were washed twice in 1 mL of PBS. The secondary antibody (Alexa Fluor™ 488 goat anti-rabbit IgG, Invitrogen, Paisley, UK) was diluted 1:100 and 400 μL was added to the correct wells on the plate. The plate was covered in aluminium foil and left to incubate at room temperature for 1 h in the dark. Following this, the wells were washed twice in 1 mL of PBS. On an individual basis, each coverslip was then taken out of each well on the plate and an aspirator pump was used to remove any excess PBS. 20 μL drops of VECTASHIELD® Antifade Mounting Medium with 1.5 μg/mL DAPI (4',6-diamidino-2-phenylindole) (Vector Laboratories) was added to the glass slides and then the coverslips were inverted and placed on top of the drops. Clear nail varnish was used to seal the coverslips. The slides were then imaged on the Zeiss LSM980-Airyscan2 confocal microscope (Zeiss, Cambridge, UK) at 60x magnification. The excitation and emission wavelengths chosen were 352/455 nm and 493/517 nm for DAPI and Alexa Fluor™ 488 secondary antibody respectively.

## 2.4 Western blotting

### 2.4.1 Reagents

NuPage™ MOPS SDS Running Buffer (20X), NuPage™ Novex 4-12% Bis-Tris gels, NuPage™ Antioxidant and 10% NuPage™ Sample Reducing Agent (10X) were purchased from Invitrogen (Hertford, UK). Novex™ Tris-Glycine SDS Sample Buffer (2X) and Novex™ ECL Chemiluminescent Substrate Reagent Kit were obtained from Invitrogen. PageRuler™

Prestained Protein Ladder (10-180 kDa) and filter paper for western blotting were obtained from Thermo Fisher Scientific (Leicestershire, UK). Immobilon®-PsQ PVDF membrane was purchased from Millipore (Dorset, UK). Marvel Original Dried Skimmed Milk Powder was acquired from Premier International Foods (Dublin, Ireland).

### 2.4.2 Sample preparation

A375 cells were seeded onto 6-well plates at densities of $5 \times 10^5$ cells/mL for treatments and $1.25 \times 10^5$ cells/mL for siRNA transfections. Plates were then incubated overnight at 37 °C and 5% $CO_2$. The following day the plates were treated with DMSO or 50 μM STK793590 for 3 h followed by 1 mM hydrogen peroxide ($H_2O_2$) for 4 h. If siRNA transfection for 72 h was being carried out, the siRNA transfection protocol described in **Section 2.6.2** was followed after cell plating and overnight incubation.

### 2.4.3 Preparing whole cell extracts

A 1:1 dilution of Tris-Glycine SDS Sample Buffer (2X) with PBS was prepared. The media in each of the wells on the plate was removed and discarded. 1 mL of cold PBS was used to wash each of the wells before being removed. Following this, 200 μL of the 1:1 SDS Sample Buffer and PBS dilution made earlier was added to each well on the plate. Once the solution in a well became viscous and had been mixed with a pipette, it was transferred into an Eppendorf tube and put on ice. This was carried out for each well. After this process was finished, the Eppendorf tubes were wrapped in parafilm and boiled for 5 mins. The tubes were centrifuged for 10 secs at 2500 rpm and placed on ice. The samples were stored at -80 °C.

### 2.4.4 Gel electrophoresis and transfer

The concentration and A260/280 ratio for the purity of each protein sample was established using the NanoDrop® ND-1000 spectrophotometer (Labtech, Uckfield, UK). The NanoDrop® ND-1000 spectrophotometer was blanked with SDS buffer prior to measuring any sample purity. A ratio of approximately 1.7 was considered pure. The NanoDrop® ND-1000 utilises the Beer-Lambert law shown below to determine the protein concentration in mg/mL:

$$A = \varepsilon b C$$

$A$ = absorbance (AU) $\qquad\qquad\qquad\qquad\qquad$ (Proteins absorb light at 280 nm)

$\varepsilon$ = extinction coefficient ($M^{-1}$ $cm^{-1}$)

$b$ = length of light path (cm)

$C$ = concentration (M)

Samples of each treatment were made with equivalent concentrations of protein to ensure that the volume of protein later loaded onto the gel was consistent across all

samples. This was conducted by diluting the samples with the 1:1 SDS Sample Buffer and PBS solution made when preparing whole cell extracts (see **Section 2.4.3**). Once this was done, NuPage™ reducing agent was added to each sample. The samples were vortexed and centrifuged for 10 secs at 2500 rpm.

The gel chamber was then prepared. The NuPage™ Novex 4-12% Bis-Tris gel (12-well gel) was removed from its plastic packaging, rinsed with Milli-Q Ultrapure water from the PURELAB® Flex (UK) and locked into the X-Cell SureLock Mini-Cell Electrophoresis System (Invitrogen) rig. The middle chamber was filled to the top with 1X MOPS SDS running buffer [**Appendix 5.1.2**]. 1X MOPS SDS running buffer was also added to 2/3 of the outer chamber. 500 μL of the NuPage™ antioxidant was added into the middle chamber and the comb was removed. After rinsing each well, 5 μL of the PageRuler™ Prestained Protein Ladder was loaded onto one of the wells on the gel, ensuring that its position would line up alongside the samples added later. The samples were then heated for 5 mins at 95 °C and loaded onto the gel, which was run at 150 V until the samples passed through the stacking gel and then at 200 V until they reached the bottom of the gel.

Before the transfer was started, a Polyvinylidene Difluoride (PDVF) membrane was placed in methanol for 30 secs to activate it, then rinsed in Milli-Q Ultrapure water and placed in 1X transfer buffer [**Appendix 5.1.2**] and left to shake at 100 rpm on a digital orbital shaker (Fisherbrand) for approximately 20 mins. Six spacing pads were also left to shake at 100 rpm in 1X transfer buffer for 20 mins. Once the gel had finished running, it was removed from the rig and cut, placed next to the PVDF membrane and sandwiched in filter paper before placing between the space pads in an XCell II Blotting module (Invitrogen). The module was inserted into the X-Cell SureLock Mini-Cell Electrophoresis System rig and locked into place. The middle chamber was filled with 1X transfer buffer to cover the spacing pads and the outer chambers were filled up to ¾ with Milli-Q Ultrapure water. The transfer was then run for 1 h at 33 V. After this, the membrane was stained with Ponceau S staining solution [**Appendix 5.1.2**] to check that the transfer was successful. Finally, the membrane was washed in Milli-Q Ultrapure water and placed into blocking buffer (5 % milk/TBST see **Appendix 5.1.2**) for 30 mins on the digital orbital shaker at 100 rpm, before being incubated overnight at 4 °C.

*2.4.5 Immunoblotting*

The membrane was removed from the fridge and incubated in primary rabbit anti-DJ-1 or anti-β-tubulin monoclonal antibody (both obtained from Cell Signaling Technology, London, UK) diluted 1:6000 or 1:1000 in blocking buffer respectively, for 1 h 30 mins to 2 h at room temperature on a tube roller. After this, the membrane was rinsed in 1X TSBT [**Appendix 5.1.2**] followed by three 5-minute washes in blocking solution on the orbital shaker at 100 rpm. This was then followed by three 5-minute washes in 1X TBST at 100 rpm on the orbital shaker. Next, the membrane was incubated in secondary anti-rabbit

HRP-conjugated antibody (Abcam, Cambridgeshire, UK) also diluted in blocking buffer (1:1000 in 5 mL) for 40 mins at room temperature on the tube roller and the membrane was washed as before. The Novex™ ECL Chemiluminescent Substrate Reagent Kit was brought to room temperature before use. The membrane was blotted with filter paper to remove excess TBST and the substrate reagent from the kit was mixed and added to the blot for 1 min according to the manufacturer's instructions. Excess substrate reagent was blotted off and the membrane was subsequently viewed using the ImageQuant LAS 4000 chemiluminescent camera (General Electric, Buckinghamshire, UK). Densitometry of western blots was calculated using ImageJ.

If a membrane required re-probing, the antibodies were stripped from it using 1X stripping solution [**Appendix 5.1.2**] for 10 mins on the orbital shaker at 100 rpm. Fresh 1X stripping solution was added to the membrane after having discarded the old solution and the process was repeated again for another 10 mins. Following this, two 10-minute washes in 1X PBS [**Appendix 5.1.2**] were performed and then two 5-minute washes in 1X TBST at 100 rpm. Finally, the membrane was placed in blocking buffer for 30 mins at 100 rpm. Re-probing of the membrane with antibodies was later carried out using the same methodology described above.

## 2.5 MTS cell viability assay

A375 cells were seeded in 96-well plates at densities of $5x10^4$ cells/mL with the final total volume being 100 $\mu$L in each well. The plates were left overnight in the incubator at 37 °C and 5% $CO_2$ to allow adherence of cells. The next day the cells were treated with DMSO or concentrations of STK793590 (30 $\mu$M, 50 $\mu$M) and Vemurafenib (0.1 $\mu$M, 1 $\mu$M) alone or in combination and left in the incubator for 72 h. Following this, 10 $\mu$L of CellTiter 96 Aqueous One Solution Cell Proliferation Assay Reagent (Promega, Hampshire, UK) was added to each well and left to incubate for approximately an hour. A POLARstar Optima microplate reader (BMG Labtech, Aylesbury, UK) was used to measure the absorbance at 490 nm after having seen a red/brown colour change. Cell viability was determined by normalising the absorbance of the treated wells to that of the control.

## 2.6 siRNA transfection

### 2.6.1 Reagents

DharmaFECT 2 Transfection Reagent, ON-TARGETplus Non-Targeting Pool siRNA, ON-TARGETplus PARK7 SMARTPool siRNA and Dharmacon™ siGLO™ Red Transfection Indicator were obtained from Dharmacon (Colorado, USA).

**Table 7 – Sequences of Dharmacon ON-TARGETplus siRNA SMARTpool**

| Gene | Target sequences |
|---|---|
| On-TARGETplus Non-targeting siRNA Pool | UGG UUU ACA UGU CGA CUA A |
| | UGG UUU ACA UGU UGU GUG A |
| | UGG UUU ACA UGU UUU CUG A |
| | UGG UUU ACA UGU UUU CCU A |
| ON-TARGETplus PARK7 SMARTPool siRNA | CAA CAC ACC CUC UUG CUA A |
| | GAA AUA GGU UUU GGA AGU A |
| | GCC GUG AUG UGG UCA UUU G |
| | GGG ACC AGC UUC GAG UUU G |

*2.6.2 Standard siRNA transfection protocol*

A375 cells were seeded in 6-well plates or 96-well plates using antibiotic-free media at densities of $5 \times 10^5$ cells/mL. They were left to incubate overnight at 37 °C and 5% $CO_2$. The next day, siRNA treatments and DharmaFECT 2 Reagent were made ready in serum-free media for transfection as shown in **Table 8** according to the manufacturer's recommendations. siRNA treatments were made from 20 μM stocks of ON-TARGETplus Non-Targeting Pool, ON-TARGETplus PARK7 SMARTPool siRNA (see **Table 7** for sequences) or RNase-free $H_2O$. These were then left to stand for 5 mins at room temperature. 1:1 solutions of the siRNA treatments and DharmaFECT 2 Reagent were then made, combined together, and left to stand for 20 mins at room temperature. Following this, antibiotic-free media was added to the siRNA/DharmaFECT 2 Reagent mixes to make up the total transfection volume in each well to be either 100 μL or 2000 μL as shown in **Table 8**. The old media in each of the wells was removed and replaced with the siRNA/DharmaFect 2 Reagent solutions. The cells were left to incubate at 37 °C and 5% $CO_2$ for 24, 48 or 72 h before RNA or protein extraction.

**Table 8 – siRNA transfection recipes**

| | Diluted siRNA (μL/well) | | Diluted DharmaFECT 2 (μL/well) | | | |
|---|---|---|---|---|---|---|
| Plate type | Volume of siRNA (μL) | Volume of serum-free media (μL) | Volume of DharmaFECT Reagent (μL) | Volume of serum-free media (μL) | Complete medium (μL)/well | Total transfection volume (μL/well) |
| 6-well | 10 | 190 | 5 | 195 | 1600 | 2000 |
| 96-well | 0.5 | 9.5 | 0.25 | 9.75 | 80 | 100 |

## 2.6.3 Assessment of siRNA uptake into cells

A375 cells were seeded onto glass coverslips (sterilised in 70% ethanol) in 12-well plates at a density of $1 \times 10^5$ cells/mL and left to incubate overnight at 37 °C and 5% $CO_2$ in a humidified environment. The next day siRNA transfection was carried out following the same protocol as described in **Section 2.6.2**, however it was modified to accomodate for Dharmacon™ siGLO™ Red Transfection Indicator. 1:1 solutions of siGLO™ Red and siRNA were made up in serum-free media before continuing as normal with the rest of the standard siRNA transfection protocol. Cells were then left to incubate at 37 °C and 5% $CO_2$ for 24 h. The next day, the media was removed, and the cells were washed twice in 1 mL of PBS. 0.5 mL of 4% PFA in PBS was then added to the cells and the plate was put on ice and put into the fridge for 1 h at 4 °C. After this, the PFA was removed, the wells were washed twice in 1 mL of PBS and then 300 µL of 14.3 µM DAPI was added to each well. The plate was left to rest for 10 mins at room temperature in a dark cupboard. Following this, the DAPI was removed, and the wells were washed twice in 1 mL of PBS. Next, DPX mounting media from Thermo Fisher Scientific was used to adhere the glass coverslips with the cells onto glass slides. The slides were then left in the fridge overnight to dry and harden. The next day the slides were imaged using the Zeiss LSM980-Airyscan2 confocal microscope (Zeiss, Cambridge, UK) at 60x magnification. The excitation and emission wavelengths chosen were 352/455 nm and 577/603 nm for DAPI and Dharmacon™ siGLO™ Red Transfection Indicator respectively.

## 2.6.4 MTS cell viability assay after siRNA transfection

A375 cells were seeded in 96-well plates at a density of $5 \times 10^4$ cells/mL in antibiotic-free media and left to incubate overnight at 37 °C and 5% $CO_2$ in a humidified environment. The next day siRNA transfection was conducted using the same protocol as described in **Section 2.6.2**. The cells were then left to incubate at 37 °C and 5% $CO_2$ for either 48 or 72 h. Following this, the cells were treated with DMSO and Vemurafenib (at 1 µM final well concentration) for 72 h. 10 µL of CellTiter 96 Aqueous One Solution Cell Proliferation Assay Reagent (Promega) was then added to each well and a POLARstar Optima microplate reader (BMG Labtech, Aylesbury, UK) was used to measure the absorbance at 490 nm after having seen a red/brown colour change. Cell viability was calculated by normalising the absorbance of the treated wells to that of the control.

## 2.7 RT-qPCR

### 2.7.1 Reagents

TRI-reagent® was purchased from Invitrogen. 2-propanol, 1-bromo-chloro-propane, ethanol, SYBR® Green JumpStart™ Taq ReadyMix™ and custom-made primers (see **Table 9**) were obtained from Sigma Aldrich. The High-Capacity cDNA Reverse Transcription kit

and RNase Inhibitor were obtained from Applied Biosystems. PCR grade water, DNA Away decontaminant and filter pipette tips were obtained from Thermo Fisher Scientific.

**Table 9 – Primer sequences for RT-qPCR**

| Gene | Forward (5'-3') | Reverse (5'-3') |
|------|-----------------|-----------------|
| NFE2L2 | AAC CAC CCT GAA AGC ACA GC | TGA AAT GCC GGA GTC AGA ATC |
| NQO1 | GCG AGA CCT TGT GAT ATT CCA G | TCC TAT GAA CAC TCG CTC AAA CC |
| HO-1 | GCG AGA CCT TGT GAT ATT CCA G | TGT TGC GCT CAA TCT CCT CCT |
| DJ-1 | GGA GAC GGT CAT CCC TGT AGA T | GCT ACA CTG TAC TGG GTC TTT TCC A |
| GAPDH | AAC AGC TCA AGA TCA TCA GC A | TGC TAA GCA GTT GGT GGT GC |

## 2.7.2 Sample preparation

A375 were seeded in 6-well plates at a density of $5 \times 10^5$ cells/mL and left to incubate overnight at 37 °C and 5% $CO_2$. The following day the cells were treated with 50 μM STK793590 for 3 h and then 1 mM hydrogen peroxide ($H_2O_2$) for 4 h or with non-targeting (NT) siRNA and DJ-1 targeting siRNA for 72 h or with combinations of siRNA and 1 mM hydrogen peroxide. After treatment or transfection, the media was removed, and cells were washed in 1 mL of cold PBS. Alternatively following transfection of cells, media was changed, and the cells were left to incubate for another 24, 48, or 72 h before the media was removed and cells washed in 1 mL of cold PBS. Following the cold PBS wash, 1 mL of Tri-Reagent was then added to the cells and left to stand for 5 mins at room temperature. The lysed cells were collected and transferred into Eppendorf tubes which were kept on ice. The samples were then stored at -80 °C.

## 2.7.3 RNA extraction

Samples in Tri-Reagent were defrosted and 100 μL of 1-bromo-3-chloro-propane (BCP) was added to each sample. Each sample was shaken by hand for 10 secs and then left to incubate at room temperature for 10 mins. Following this, the samples were centrifuged for 20 mins at 12000 x g at 4 °C. The top aqueous layer from each sample was then transferred to fresh Eppendorf tubes and 500 μL of 2-propanol was added. The samples were vortexed for 10 secs and incubated at room temperature for 10 mins. They were then centrifuged for 15 mins at 12000 x g at 4 °C. The supernatants were removed and discarded, and 1 mL of 70% ethanol was added to each tube. The samples were vortexed gently using 6x1 sec pulses and then centrifuged for 10 mins at 12000 x g at 4 °C. After this, the ethanol supernatant was removed, and any remnants were left to evaporate at room temperature. Once all the ethanol remnants had evaporated, 20 μL of nuclease-free water was added to each sample. The samples were stored at -80 °C.

## 2.7.4 cDNA synthesis

The concentration and purity of each RNA sample was firstly established using the NanoDrop® ND-1000 spectrophotometer (Labtech, Uckfield, UK). The purity of RNA was measured using the A260/280 and A260/230 ratios, where a value between 1.8 and 2 was considered pure. RNA absorbs light at 260 nm, and its concentration in ng/μL was determined using the Beer-Lambert law as described in **Section 2.4.4**. If needed, the samples were then diluted to 200 ng/μL with nuclease-free water. 200 ng of RNA was made up in 5 μL of nuclease-free water. The High-Capacity cDNA Reverse Transcription Kit (Applied Biosystems) was used to make a cDNA synthesis Mastermix solution consisting of 32% nuclease-free water, 10% reverse transcriptase, 20% 10X RT buffer, 20% random hexamers, 10% RNase inhibitor and 8% dNTPs. 5 μL of the prepared cDNA synthesis Mastermix was then added to the RNA samples and mixed. Following this, the samples were placed in a PTC-100 Thermal Peltier Cycler (Biorad, Hertfordshire, UK) for 10 mins at 25 °C, 2 h for 37 °C, 5 mins at 85 °C, and then held at 4 °C up until removal. The samples were stored at -20 °C.

## 2.7.5 RT-qPCR

The RT-qPCR Mastermixes were made with 26.67% nuclease-free water, 66.67% SYBR Green and 6.67% forward and reverse primers for each gene of interest (primer sequences are shown in **Table 9**). 5 μL of cDNA was mixed with 15 μL of appropriate RT-qPCR Mastermix for each sample in 0.1 mL tubes. For each gene, samples were run in triplicate and non-template controls (NTCs) which were made up using nuclease-free water. Samples were put into the QIAGEN Rotor-gene Q Series 5 Plex (QIAGEN, Manchester, UK) and cycled on a two-step melt program. The settings for the program were: 95 °C for 2 minutes followed by 40 cycles of 95 °C for 15 secs then 60 °C at 40 secs, and a melt curve stage ramping from 60-94 °C. The $2^{-\Delta\Delta Ct}$ method shown below was used to determine relative gene expression using the resulting cycle threshold (Ct) values as analysed by the QIAGEN Rotor-gene Q Series Software 2 (GAPDH was used as the housekeeping gene).

$2^{-\Delta\Delta Ct}$ method calculations:

ΔCt = Ct (gene of interest) – Ct (housekeeping gene)

ΔΔCt = ΔCt (treatment condition) – ΔCt (control/untreated condition)

Relative gene expression = $2^{-\Delta\Delta Ct}$

**2.8 Tumouroids**

*2.8.1 Culturing tumouroids using the 'hanging drop' method*

A375 cells were detached with TrypLE Express and then counted. The cell suspension volume needed was calculated as relative to the total number of drops being made along with seeding densities of 0.1, 0.5 or $1x10^4$ cells/well. Following this, the calculated volume of cell suspension was centrifuged at 2500 rpm for 5 mins, and the supernatant was removed, however, 5 $\mu$L was left behind. The cell pellet was then resuspended in fresh media whose volume had been calculated using this equation: volume of media needed = 10 $\mu$L/drop x total number of drops wanted. The lid of a petri dish was inverted and 10 $\mu$L drops of cell suspension were then deposited onto the bottom of the lid. The bottom part of the petri dish was filled with 15 mL of PBS to serve as a hydration chamber. Following this, the lid of the petri dish with the drops was then inverted and put on top of the bottom half. The petri dish was incubated at 37 °C and 5% $CO_2$ in a humidified environment for 12 days and checked every 3 days for tumouroid formation. Images were taken using the Invitrogen EVOS XL Core Imaging System at 10x magnification and Image J was used to calculate the area of the tumouroids.

*2.8.2 Culturing tumouroids using Matrigel*

12-well plates with Menzel glass coverslips sterilised in 70% ethanol were prepared. Matrigel® Membrane Matrix (Corning, New York, USA) was defrosted and kept on ice. A375 cells were seeded at 0.1, 0.5, or $1x10^4$ cells/well. After seeding, the calculated volume of cell suspension was centrifuged at 2500 rpm for 5 mins, and the supernatant was removed, however, 5 $\mu$L was left behind. The cell pellet was resuspended in the 5 $\mu$L of remaining supernatant and Matrigel® Membrane Matrix was added whose volume had been calculated using this equation: volume of Matrigel needed = 10 $\mu$L/well x total number of wells. The cell suspension was mixed with the Matrigel® Membrane Matrix gently with a pipette to avoid introduction of bubbles. 10 $\mu$L of the cell suspension/Matrigel® Membrane Matrix solution was then transferred onto the glass coverslips in each of the wells, and the plate was incubated for 30 mins at 37 °C and 5% $CO_2$. 100 $\mu$L of pre-warmed media was then dropped on top of the cell suspension/Matrigel® Membrane Matrix globules in each well. The plate was incubated at 37 °C and 5% $CO_2$ in a humidified environment over 9 or 12 days and the media was changed every 3 days. Images were taken using the Invitrogen EVOS XL Core Imaging System at 20x magnification and Image J was used to calculate the area of the tumouroids.

*2.8.3 Matrigel tumouroid treatment*

A375 cells were cultured following the same methodology as detailed in **Section 2.8.2** at a seeding density of $0.1x10^4$ cells/well. On day 4 of culturing, the tumouroids were treated

with DMSO, STK793590 (50 $\mu$M) and Vemurafenib (1 $\mu$M) alone or in combination. The tumouroids were then treated continuously over the next 4 days with the same compounds. However, before treating the tumouroids each time, it was ensured that the old media in the wells was replaced with fresh media excluding day 4 treatment. Images of tumouroids were taken using the Zeiss Observer 7 microscope (Zeiss, Cambridge, UK) at 10x with 2.5x tube lens magnification, with the incubation chamber set at 37 °C and 5% $CO_2$ in a humidified environment on days 0, 3, 4, 7 and 9. The tile region for each well was verified before image acquisition was started. Image J was used to calculate the area of the tumouroids.

### 2.8.4 Assessment of cell viability/cytotoxicity for tumouroids cultured in Matrigel

On day 9 of culturing tumouroids, one vial of calcein-AM and one vial of ethidium homodimer-1 from the LIVE/DEAD™ Viability/Cytotoxicity kit (Invitrogen) for mammalian cells were defrosted. Calcein-AM fluoresces green when interacting with live cells and ethidium homodimer-1 fluoresces red when interacting with dead cells. Calcein-AM can cross cell membranes and is enzymatically modified by esterases to calcein, causing these to fluoresce green when bound to calcium. Ethidium cannot cross cell membranes, meaning that it can only enter cells when cell membrane integrity is lost. Once inside the cell, ethidium homodimer-1 binds to DNA, fluorescing red[217]. A 2 $\mu$M calcein-AM solution and 4 $\mu$M ethidium homodimer-1 solution was made up in PBS, vortexed and the tube wrapped in aluminium foil. The old media in each of the wells with tumouroids was removed and replaced with 100 $\mu$L of the prepared solution and incubated for 45 mins at 37 °C and 5% $CO_2$. Following this, the tumouroids were imaged using the Zeiss Observer 7 microscope (Zeiss, Cambridge, UK) at 10x with 2.5x tube lens magnification, with the incubation chamber set at 37 °C and 5% $CO_2$ in a humidified environment. The tile region for each well was verified before image acquisition was started. The excitation wavelengths chosen were 494/517 nm FITC/GFP and 528/617 nm RFP for calcein-AM and ethidium homodimer-1 respectively.

### 2.8.5 Culturing tumouroids using ultra-low adherence plates

A375 cells were detached with TrypLE Express and then counted. The cells were then seeded in 96-well Ultra-Low Attachment U-bottom Costar plates (Corning) at densities of 0.1, 0.2 or 0.5x$10^4$ cells/well in 100 $\mu$L or 200 $\mu$L of medium per well. The plate was wrapped in parafilm before being centrifuged for 10 mins at 1000 g and 21 °C. It was then placed in the incubator and tumouroids were allowed to grow over 9 or 12 days at 37 °C and 5% $CO_2$ in a humidified environment. 50 $\mu$L or 100 $\mu$L media changes were conducted every 3 days and images were taken using the Invitrogen EVOS XL Core Imaging System at 4x magnification. Image J was used to calculate the area of the tumouroids.

*2.8.6 Ultra-low adherence tumouroid treatment*

A375 cells were cultured following the same protocol described in **Section 2.8.5** at a seeding density of $0.1 \times 10^4$ cells/well in 200 μL of medium per well. On day 4 of culturing, the tumouroids were treated with either DMSO, Vemurafenib (1 μM or 10 μM) and staurosporine (1 μM or 5 μM) or DMSO, STK793590 (30 μM or 50 μM) and Vemurafenib (0.1 μM or 1 μM) alone or in combination. Treatment was carried out only once or continuously over the next 4 days. For the one-time treatment of drugs, 100 μL media changes were conducted every 3 days, whereas for the continuous treatment 100 μL media changes were carried out before every treatment excluding day 4 treatment. Images of tumouroids were taken using the Zeiss Observer 7 microscope (Zeiss, Cambridge, UK) at 10x with 2.5x tube lens magnification with the incubation chamber set at 37 °C and 5% $CO_2$ in a humidified environment on days 0, 3, 4, 7 and 9. The tile region for each tumouroid was verified before image acquisition was started. Image J was used to calculate the area of the tumouroids.

*2.8.7 Assessment of cell viability/cytotoxicity for tumouroids cultured in ultra-low adherence plates*

The protocol for measuring cell viability/cytotoxicity for low-adherence-cultured tumouroids was the same as described in **Section 2.8.4**, however the LIVE/DEAD™ solution was made up of a 4 μM calcein-AM solution and an 8 μM ethidium homodimer-1 solution in PBS, with 200 μL of this being added to the wells. Tumouroids were imaged at 2.5x or 10x with 2.5x tube lens magnifications. The tile region for each tumouroid was verified before image acquisition was started. LIVE/DEAD ratios were calculated using ImageJ.

## 2.9 Statistical analysis

Data was analysed using GraphPad Prism 10 and Image J was used to analyse all microscopy images. Normality and lognormality tests were done using the Shapiro-Wilks test. Datasets found to be non-significant by the Shapiro-Wilks test were analysed using one-way ANOVA and post-hoc analysis was conducted using Dunnett's multiple comparison test or Tukey's test where appropriate as shown in figure legends. Datasets found to be significant in the Shapiro-Wilks test were analysed using a non-parametric Kruskal-Wallis test with post-hoc analysis done via Dunn's multiple comparison test or Tukey's test, as indicated in figure legends. Experiments were conducted to N=3 unless stated otherwise and presented as the mean ± SEM (P*≤0.05, P**≤0.01, P***≤0.001, P****≤0.0001).

# 3. Results

## 3.1 Role of DJ-1 in melanoma

### 3.1.1 DJ-1 protein expression in melanoma cell lines

DJ-1 is overexpressed in specific cancers (see **Figure 9**)[133,177,178,179]. Previous work from the O'Connell lab has found high and varied expression in a panel of human melanoma cell lines[218]. To verify DJ-1 expression in human melanoma cells, 4 melanoma cell lines were studied. Protein expression was measured by western blot analysis [**Figure 12**].

**Figure 12A and B** show that each of the 4 melanoma cell lines expressed DJ-1 protein, and that SK-MEL-28 had the highest protein expression, whereas UACC 1273 had the lowest expression. The A375 and MEL501 melanoma cell lines displayed similar DJ-1 protein expression and higher expression than the UACC 1273 melanoma cell line. These results confirm previous results from the O'Connell lab. Previous work in the lab also demonstrated that SK-MEL-28 cells had a slow proliferation rate and therefore A375 cells were chosen for further research.
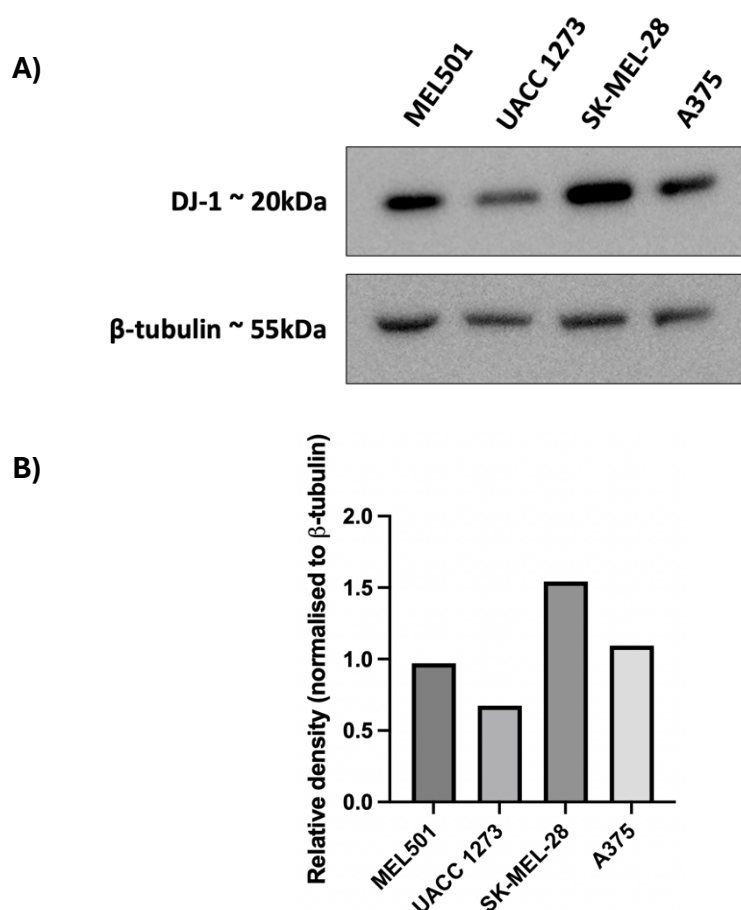


**Figure 12 – DJ-1 protein expression in human melanoma cell lines.** DJ-1 protein expression was studied by western blot analysis using whole cell lysates made from $1 \times 10^6$ cells of each cell line. **A)** Western blot images of DJ-1 expression in melanoma cell lines, with β-tubulin used as the loading control. Representative of one independent experiment (N=1). **B)** Densitometry analysis of western blot images in **A**. Representative of one independent experiment (N=1).

## 3.1.2 Location of DJ-1 protein in melanoma cells

DJ-1 expression in A375 cells was then examined by immunofluorescence microscopy. **Figure 13** indicates once again that DJ-1, as shown in green, is clearly expressed in A375 cells, validating the previous results in **Figure 12**. Interestingly, DJ-1 is present in both the cytoplasm and nuclei of these cells.
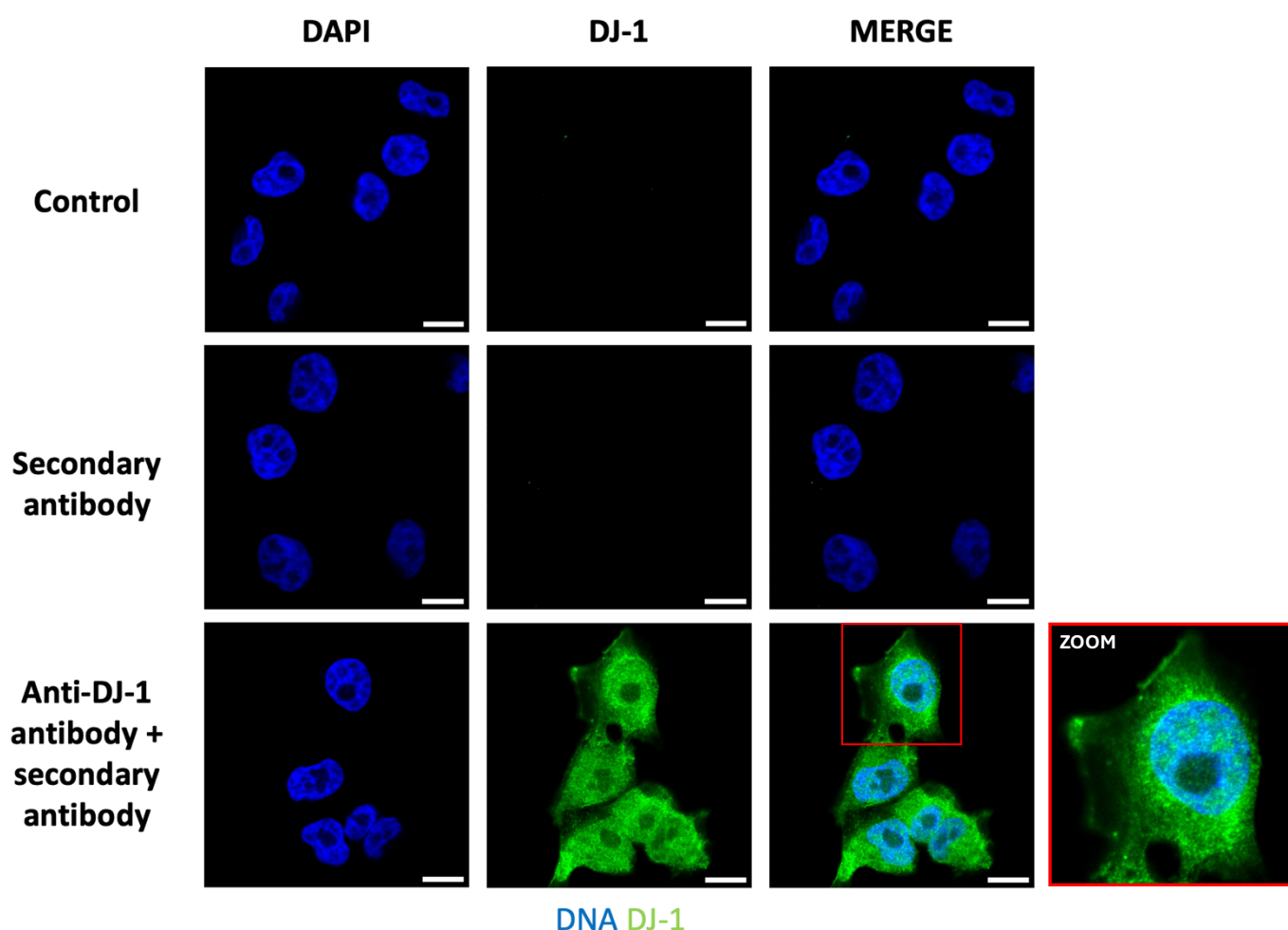


**Figure 13 – DJ-1 localisation in A375 cells.** Cells were seeded overnight onto glass coverslips at a density of $1\times10^5$ cells/mL, fixed with PFA and incubated with Triton X-100. Following this, cells were incubated overnight with anti-DJ-1 antibody and then with secondary antibody for 1 h. Glass coverslips were fixed onto glass slides with VECTASHIELD® Antifade Mounting Medium with DAPI. The control was untreated A375 cells (no antibodies). In blue is DAPI and in green is DJ-1. DJ-1 protein is present in both the nuclei and cytoplasm of A375 cells. Images were taken on the confocal microscope with analysis completed in ImageJ. A zoomed in section of the anti-DJ-1 antibody + secondary antibody image is indicated by the red box on the right-hand side. Representative of 1 independent experiment (N=1). Scale bar 100 μm.

## 3.1.3 Validation of DJ-1 knockdown in A375 cells with siRNA

To investigate the role of DJ-1 in A375 cells, knockdown of DJ-1 was achieved by utilising siRNA technology. A375 cells were transfected with 25 nM DJ-1 siRNA (siDJ-1) for 24 h and with Dharmacon™ siGLO red transfection indicator, after which the cells were fixed and viewed by confocal microscopy. This was conducted to determine if siRNA was being taken up by the cells. **Figure 14A** shows that siGLO was successfully taken up into the cells when A375 cells were transfected with either 25 nM non-targeting (NT) siRNA (NT-siRNA) or 25 nM siDJ-1. **Figure 14B** indicates that cells transfected with 25 nM NT-siRNA had the highest uptake.
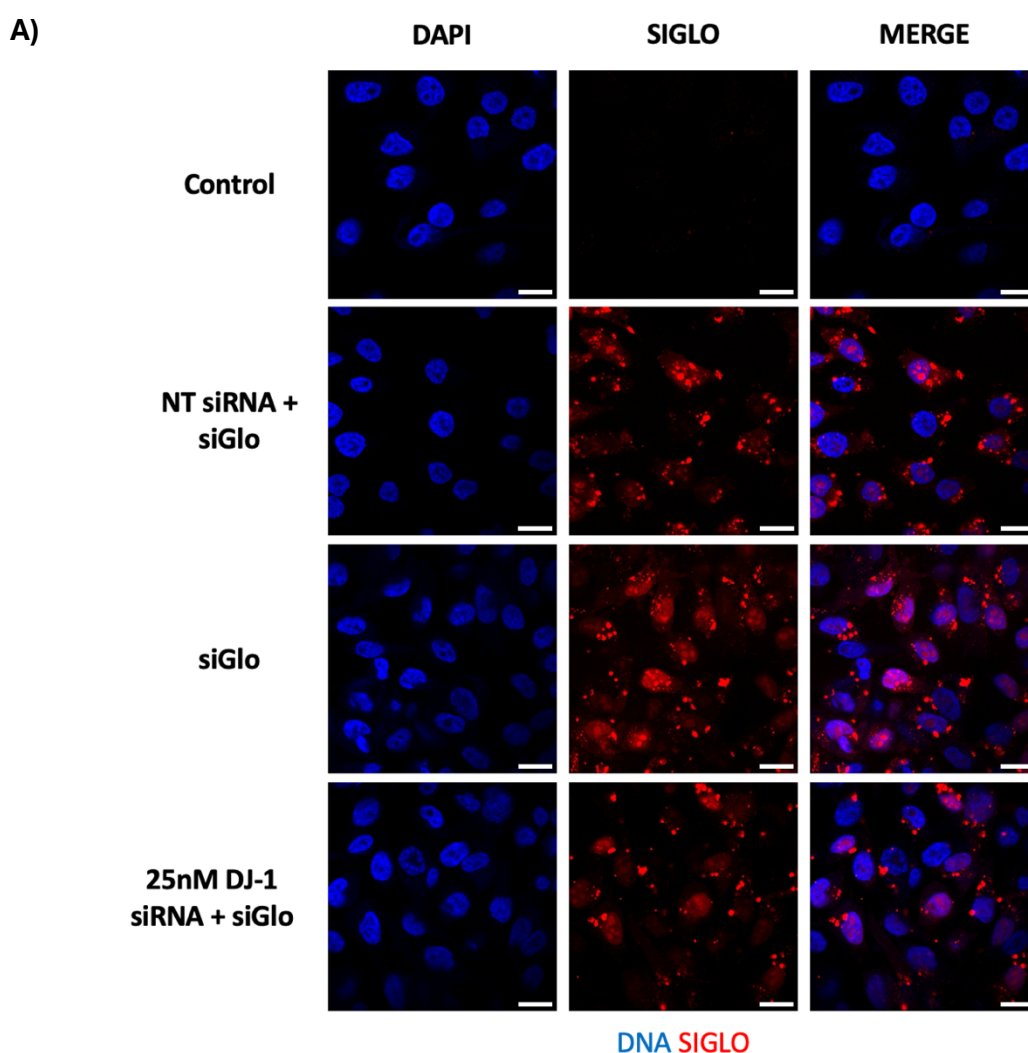


**B)**

| Sample | Average % uptake |
|---|---|
| 25nM NT siRNA + siGlo | 66.8 |
| siGlo | 41.3 |
| 25nM DJ-1 siRNA + siGlo | 36.2 |

**Figure 14 – Visualisation and efficiency of siRNA uptake by A375 cells.** A375 cells ($1 \times 10^5$ cells/mL) were seeded overnight and transfected with 25 nM non-targeting (NT) siRNA or DJ-1 targeting siRNA in addition with siGLO red transfection indicator, or siGLO red transfection indicator on its own for 24 h. All conditions

had DharmaFECT reagent added to them excluding the control. Cells were fixed and stained with DAPI and then viewed under a confocal microscope. The control cells were only treated with DAPI (no siRNA or siGLO). **A)** Confocal microscope images showed successful siRNA uptake by A375 cells. DAPI is in blue and siGLO is in red. Images are representative of one independent experiment (N=1). Scale bar 100 μm. **B)** Calculated average siRNA and siGLO percentage uptake in A375 cells. Representative of one independent experiment (N=1).

Following visualisation of siRNA uptake, DJ-1 mRNA expression was measured by RT-qPCR following knockdown. A375 cells were treated with 100 nM siDJ-1 or NT-siRNA for 72 h, based on previous optimisation in the O'Connell lab. **Figure 15A** shows that DJ-1 knockdown was successfully achieved; DJ-1 mRNA expression was inhibited by 66%. Further inhibition of DJ-1 mRNA was not achieved most likely due to the results seen in **Figure 14A and B**, as not all the cells were taking up the siDJ-1.

Following this, DJ-1 protein expression after siRNA knockdown was examined. A375 cells were transfected with 5, 25 or 100 nM siDJ-1 for 72 h and protein expression was then analysed via western blot. The results in **Figure 15B** demonstrate that DJ-1 protein expression was dramatically decreased after transfection with 5, 25 and 100 nM siDJ-1 compared to the untreated and non-targeting controls. These knockdown results confirm previous results from the O'Connell lab, which yielded the same outcomes.
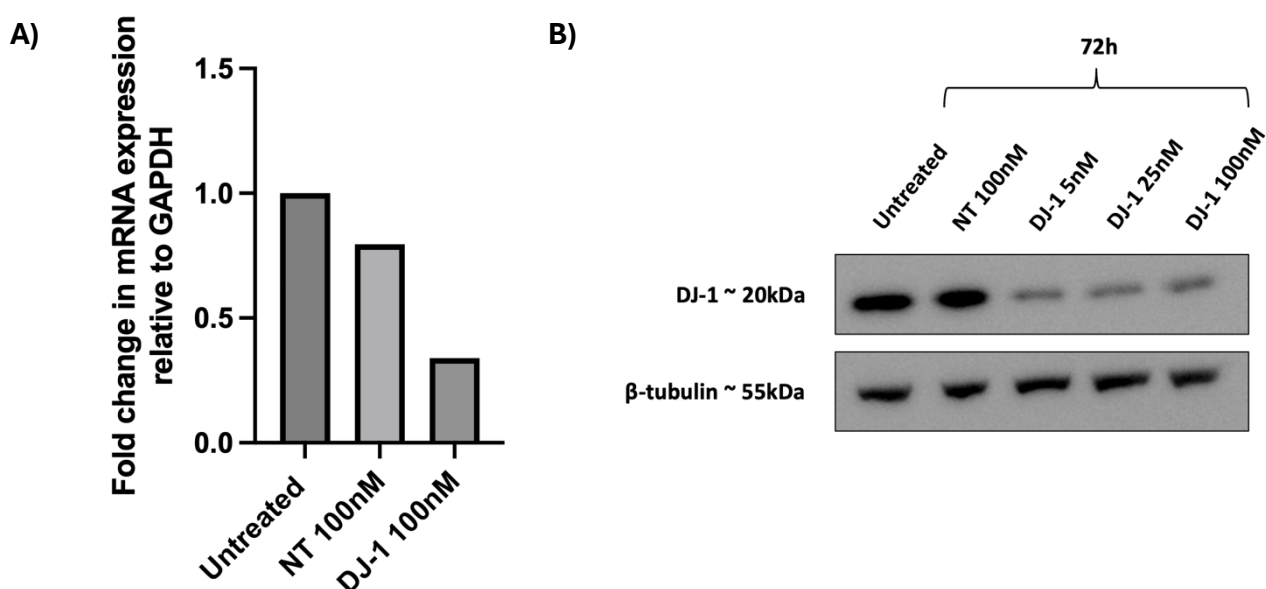


**Figure 15 – siRNA knockdown of DJ-1 mRNA and protein expression in A375 cells. A)** A375 cells ($1\times10^6$) were seeded overnight and then transfected with 100 nM DJ-1 or non-targeting (NT) siRNA for 72 h. DJ-1 mRNA expression was analysed by RT-qPCR. Results were normalised to GAPDH and presented as fold mRNA expression relative to untreated control (N=1). **B)** Cells ($1\times10^6$) were transfected with 100 nM NT-siRNA and 5-100 nM siDJ-1 for 72 h. β-tubulin was used as the loading control (N=1).

### 3.1.4 DJ-1 knockdown effects on cell proliferation

Once DJ-1 knockdown was successfully conducted and validated, the next stage involved investigating whether DJ-1 plays a role in A375 cell proliferation, as sustaining proliferative signalling is a crucial hallmark of cancer[5,6]. This was explored via MTS assay. A375 cells were treated with 5-100 nM NT-siRNA or siDJ-1for 72 h after which cell viability was assessed. **Figure 16** shows that 5 nM and 25 nM siDJ-1 had no significant effects on A375 cell viability compared to their NT controls; however, 100 nM siDJ-1 had a small but statistically significant reduction on cell viability (12.4%, p≤0.01).
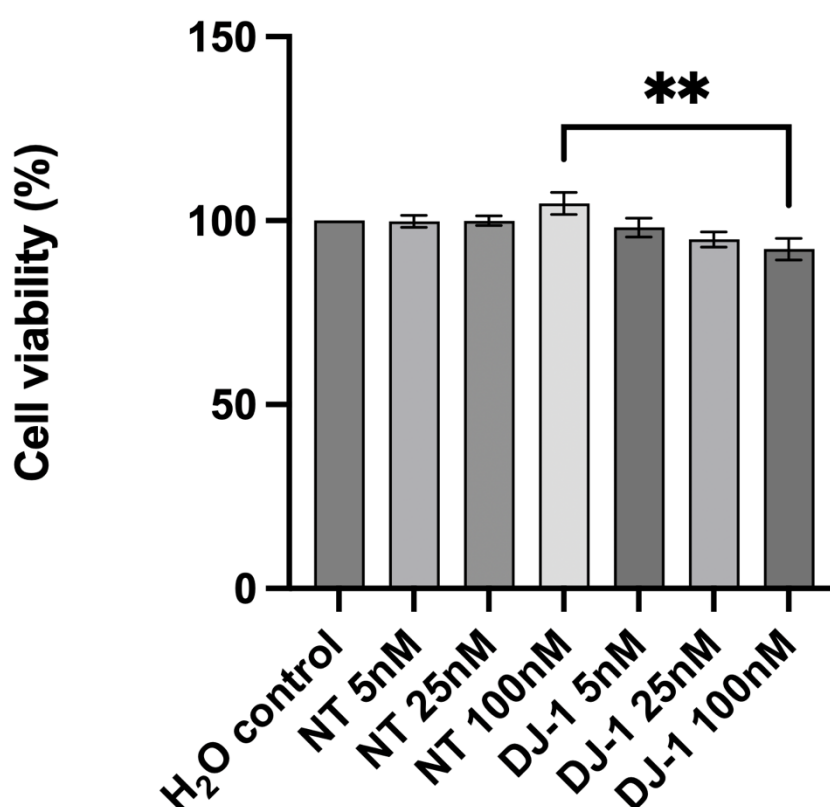


**Figure 16 – DJ-1 knockdown by siRNA decreases A375 cell viability.** A375 cells ($5x10^4$ cells/mL) were seeded overnight and then transfected with 5-100 nM non-targeting (NT) or DJ-1 targeting siRNA for 72 h. The water ($H_2O$) control did not contain any siRNA (data was normalised to the $H_2O$ control). Cell viability was measured via MTS assay. Statistical analysis was by one-way ANOVA and post-hoc analysis via Dunnett's multiple comparisons test (P*≤0.05, P**≤0.01, P***≤0.001, P****≤0.0001). Data is shown as mean ± SEM, N=3.

$BRAF^{V600E}$ mutations are present in A375 cells[219]. This study assessed whether DJ-1 knockdown enhanced the sensitivity of cells to vemurafenib, a BRAF inhibitor currently employed in the treatment of metastatic melanoma[107]. A375 cells were treated with 100 nM siDJ-1 for 72 h, followed by 72 h treatment with 1 µM vemurafenib. Cell viability was measured via MTS assay. **Figure 17** shows that vemurafenib on its own significantly inhibited cell viability (14.1%, P≤0.05). Vemurafenib in combination with 100 nM NT-

siRNA resulted in a similar inhibition (16%, P≤0.05). DJ-1 knockdown followed by vemurafenib treatment had no significant effects on A375 cell viability. Interestingly, though, 100 nM DJ-1 knockdown on its own had no effect on A375 cell viability either, contradicting the results which were obtained in **Figure 17**. To dispel doubts whether this phenomenon occurred due to cells recovering their expression of DJ-1, experiments investigating DJ-1 mRNA levels at 24, 48 or 72 h timepoints post 72 h transfection were carried out. However, DJ-1 siRNA caused knockdown at all these timepoints following 72 h transfection (see **Appendix 5.2**). Although the results in **Figure 17** contradict those presented in **Figure 16**, the differing experimental settings (difference in timepoints) preclude a direct comparison between the two.
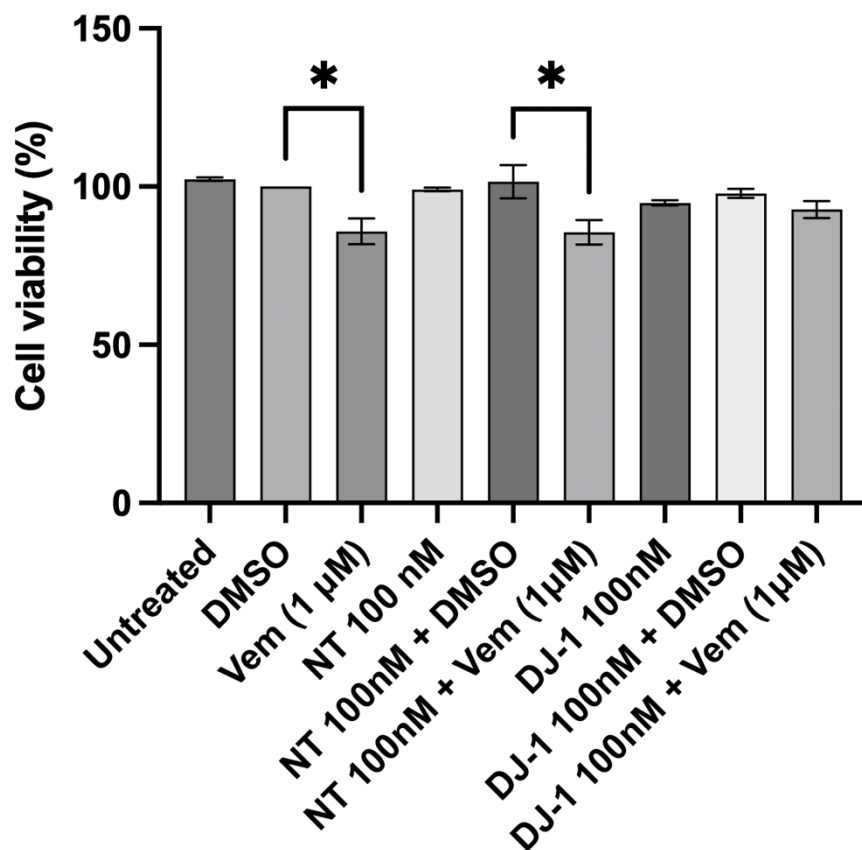


**Figure 17 – DJ-1 knockdown by siRNA followed by vemurafenib treatment has no effect on A375 cell viability.** A375 cells ($5 \times 10^4$ cells/mL) were seeded overnight and then 100 nM non-targeting (NT) or DJ-1 targeting siRNA was added to the cells for 72 h. The media in the wells was then changed and cells were treated with DMSO or 1µM vemurafenib for a further 72 h. Cell viability was measured via MTS assay and data was normalised to the DMSO control. Statistical analysis was by one-way ANOVA and post-hoc analysis via Tukey's test (P*≤0.05, P**≤0.01, P***≤0.001, P****≤0.0001). Data is shown as mean ± SEM, N=3.

### 3.1.5 DJ-1 knockdown effects on the Nrf2 signalling pathway

Both DJ-1 and Nrf2 are sensors of oxidative stress. Since DJ-1 has been reported to activate Nrf2[137,138,140,181], the effects of DJ-1 knockdown on the Nrf2 and its downstream target genes, HO-1 and NQO1, were explored next, both under normal conditions and in response to $H_2O_2$-induced oxidative stress. A375 cells were treated with 100 nM NT-siRNA or siDJ-1 for 72 h. Following this, cells were treated with 1mM hydrogen peroxide ($H_2O_2$) for 4 h to induce oxidative stress and gene expression was assessed by RT-qPCR.

**Figure 18A-C** shows that under $H_2O_2$ oxidative stress conditions and normal conditions DJ-1 knockdown had no significant effects on DJ-1, NQO1 or Nrf2 mRNA expression compared to NT controls. DJ-1 mRNA levels following DJ-1 knockdown with 100 nM siDJ-1 decreased by 65.4% and 64.9% under $H_2O_2$ oxidative stress conditions and normal conditions compared to NT controls respectively, indicating a clear difference even though these were insignificant. No difference between normal and oxidative stress conditions is as expected as $H_2O_2$ does not induce DJ-1 gene expression but causes oxidation of it which affects its function. Slight increases in Nrf2 mRNA expression were seen when $H_2O_2$ was added to the cells, however these were also insignificant.
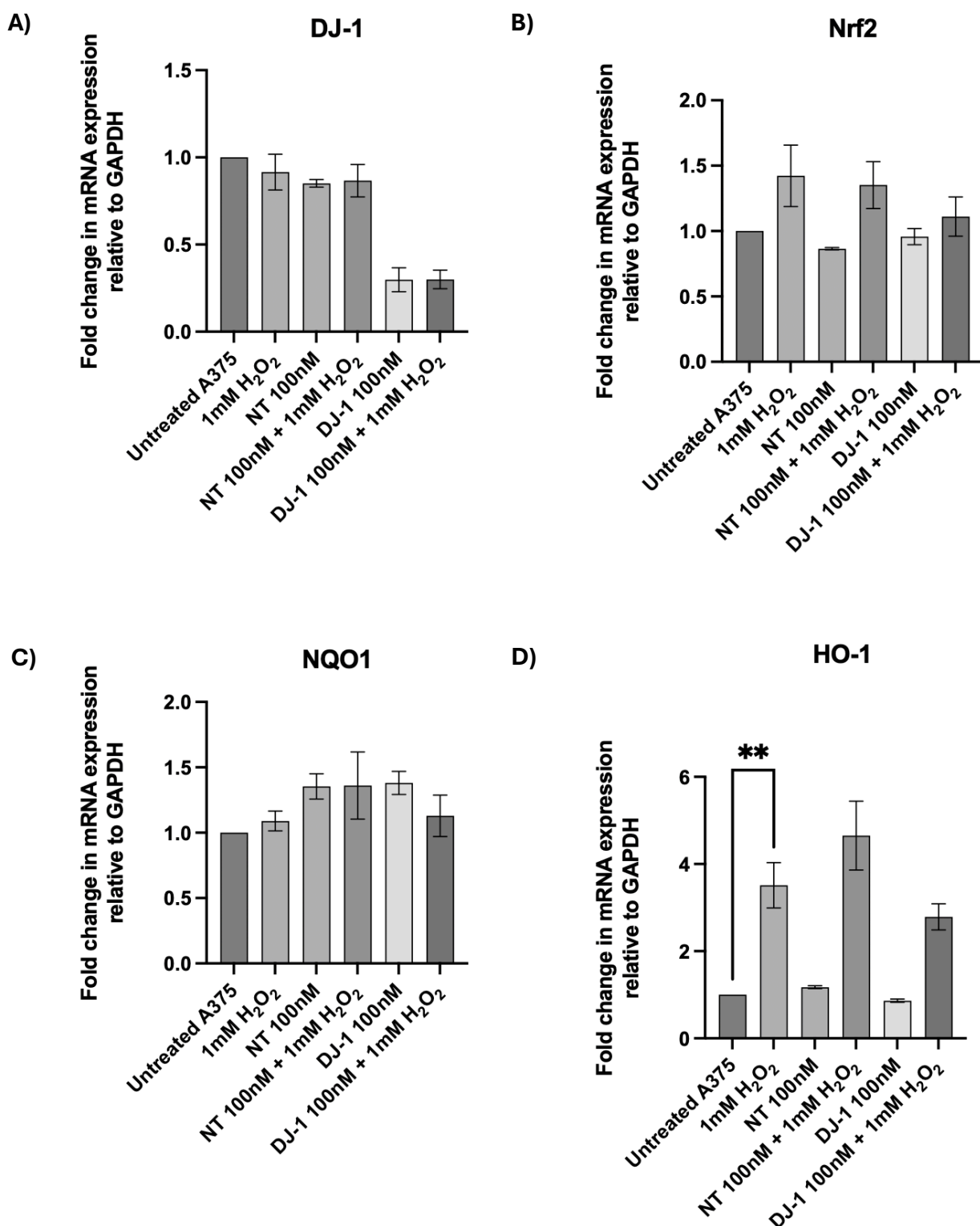
**Figure 18 – Effects of DJ-1 knockdown on DJ-1, HO-1, NQO1 and Nrf2 mRNA expression under normal and oxidative stress induced conditions.** A375 cells ($1\times10^6$) were seeded into 6-well plates and incubated for 24 h before treatment with 100nm non-targeting (NT) siRNA or 100 nM DJ-1 targeting siRNA for 72 h. Following this the cells were treated with 1 mM hydrogen peroxide ($H_2O_2$) for 4 h. Next, total RNA was extracted and reverse transcribed and mRNA expression for DJ-1, HO-1, NQO1 and Nrf2 measured by RT-qPCR. **A)** DJ-1 **B)** Nrf2 **C)** NQO1 **D)** HO-1. Results were normalised to GAPDH and presented as fold expression increase in mRNA relative to the untreated control. Representative of three independent experiments (N=3) and statistical analysis was done by Kruskal-Wallis and post-hoc analysis via Dunn's

multiple comparisons for **A)** and one-way ANOVA and post-hoc analysis via Tukey's test for **B)**, **C)** and **D)** (P*≤0.05, P**≤0.01, P***≤0.001, P****≤0.0001). Data is shown as mean ± SEM.

DJ-1 knockdown under normal conditions had no significant effects on HO-1 mRNA expression compared to the non-targeting control (**Figure 18B**). The 1 mM $H_2O_2$ control showed a statistically significant increase in HO-1 mRNA expression compared to the untreated control, suggesting that oxidative stress induced by $H_2O_2$ triggers HO-1 mRNA expression. In the presence of oxidative stress (1 mM $H_2O_2$), there was a 40.1% reduction in HO-1 mRNA expression with 100 nM siDJ-1 compared to the NT control, potentially suggesting that DJ-1 knockdown influences HO-1 production however only under oxidative stress conditions. Even so, this reduction was not statistically significant.

### 3.1.6 Targeting DJ-1 in melanoma with STK793590

STK793590 is a small molecule inhibitor of DJ-1 and an isatin (1H-indole-2,3-dione) derivative discovered by Tashiro *et al* (2018)[136] (see **Section 1.3.5**). Its mechanism of action involves binding to the critical Cysteine-106 residue of the DJ-1 homodimer, impairing DJ-1 function. The anti-cancer effects of STK793590 have not been widely studied, therefore we investigated its effect in melanoma.

Previous work in the O'Connell lab demonstrated that STK793590 mildly inhibited A375 cell proliferation when compared with the BRAF inhibitor, vemurafenib, and cytotoxic antibiotic chemotherapy, doxorubicin. Consequently, we explored whether the combination of STK793590 with an additional drug would enhance the inhibitory effect on A375 cell proliferation (this had not been tested before). For this experiment, vemurafenib was chosen to combine with STK793590. A375 cells were treated with different combinations of 30 µM or 50 µM STK793590 and 0.1 µM or 1 µM vemurafenib. DMSO was used as the control and cell proliferation was assessed via MTS assay.

**Figure 19** shows that 30 µM STK793590 had no effect on A375 cell viability. 50 µM STK793590 resulted in a 18% decrease in A375 cell viability compared to the DMSO control, however the decrease was insignificant. Furthermore, 0.1 µM vemurafenib had no effect on cell viability whereas 1 µM vemurafenib resulted in a significant 26% decrease in cell viability. 30 µM STK793590 in combination with 0.1 µM vemurafenib had no effect on cell viability, however in combination with 1 µM vemurafenib, a 5% decrease in cell viability was seen, yet it was insignificant. 50 µM STK793590 in combination with 0.1 µM vemurafenib resulted in a significant 46% decrease in cell viability whereas 50 µM STK793590 in combination with 1 µM vemurafenib resulted in a significant 58% decrease in cell viability. These results indicate that both combinations have greater effects on cell viability compared to vemurafenib treatment alone.
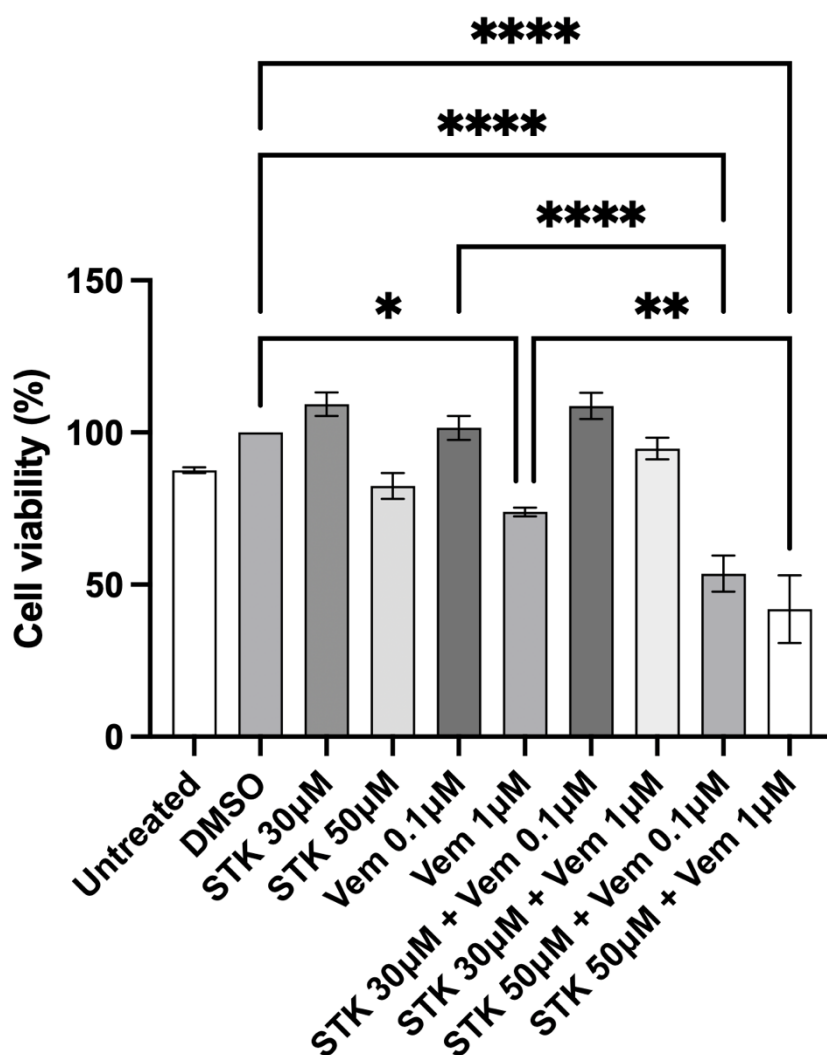
**Figure 19 – STK793590 in combination with vemurafenib reduces A375 cell viability.** A375 cells (5x10⁴ cells/mL) were seeded into a 96-well plate and treated with STK793590 (30 µM, 50 µM) and vemurafenib (0.1 µM, 1 µM) alone or in combination. Cell viability was measured via MTS assay and data was normalised to the DMSO control. Data presented is from three independent experiments (N=3) and statistical analysis was conducted by one-way ANOVA and post-hoc analysis via Tukey's test (P*≤0.05, P**≤0.01, P***≤0.001, P****≤0.0001). Data is shown as mean ± SEM.

We next investigated the effects of STK793590 on mRNA expression of DJ-1 and Nrf2 along with its antioxidant downstream genes HO-1 and NQO1 under both normal and oxidative stress conditions. A375 cells were treated with 50 µM STK793590 for 3 h, followed by treatment with 1 mM hydrogen peroxide ($H_2O_2$) for 4 h to induce oxidative stress. Total RNA was then extracted, reverse transcribed and mRNA expression of DJ-1, Nrf2, NQO1 and HO-1 was measured via RT-qPCR. 50 µM STK793590, 1 mM $H_2O_2$ and the combination of the two had no significant effects on mRNA expression of DJ-1, NQO1 and Nrf2 (**Figure 20A, C, D**). For HO-1 mRNA expression, low relative expression was seen for the untreated control, DMSO control and 50 µM STK793590 (**Figure 20B**), however, higher HO-1 mRNA expression levels were observed for DMSO + 1 mM $H_2O_2$, 50 µM STK793590

+ 1 mM $H_2O_2$ and 1 mM $H_2O_2$ alone. This indicates that $H_2O_2$ treatment increases in HO-1 mRNA expression. Compared to the 1 mM $H_2O_2$ on its own, DMSO + 1 mM $H_2O_2$ and 50 µM STK793590 + 1 mM $H_2O_2$ had higher HO-1 mRNA expressions, but these were unsignificant.
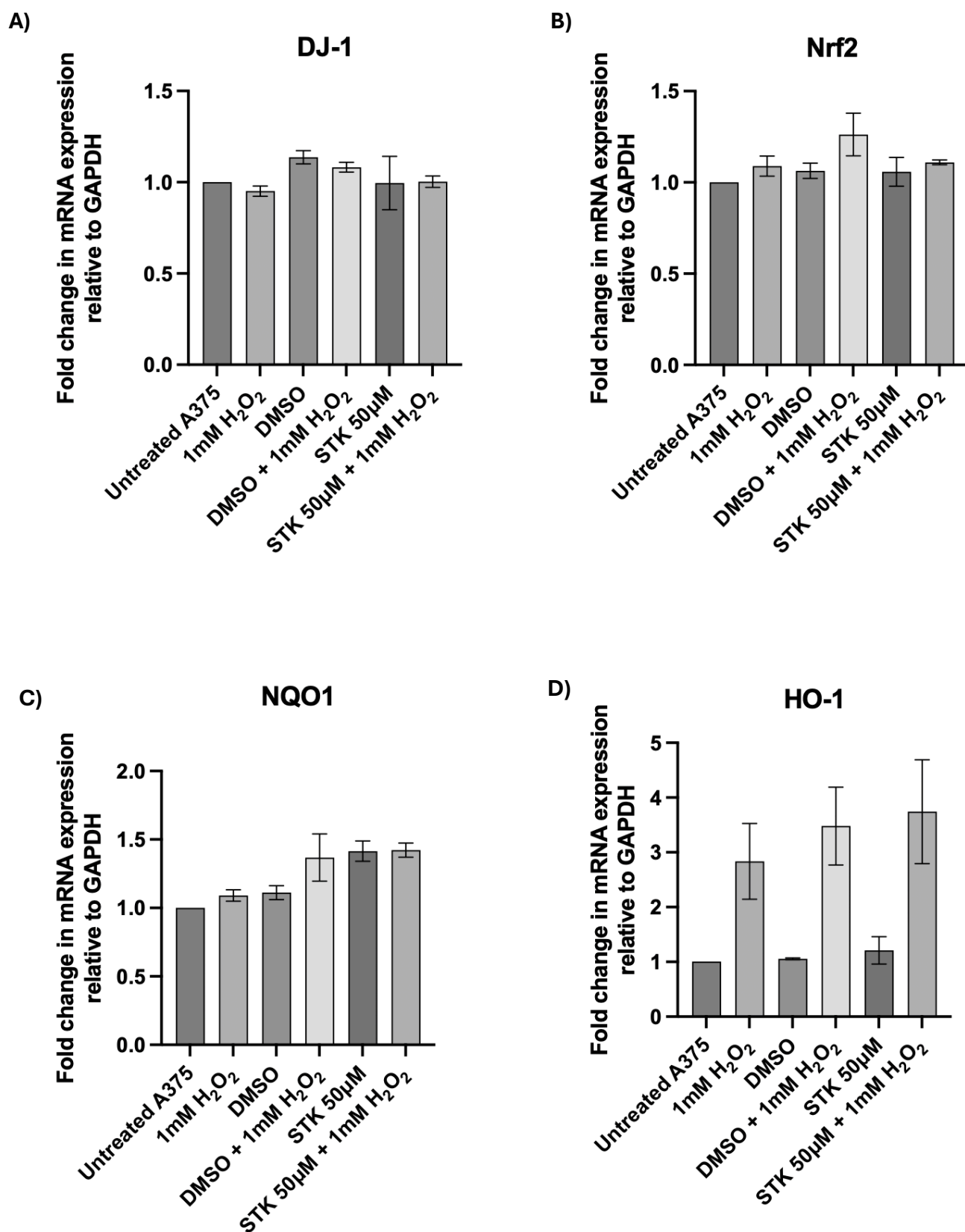
**Figure 20 – Effects of STK793590 on DJ-1, HO-1, NQO1 and Nrf2 mRNA expression under normal and oxidative stress induced conditions.** A375 cells ($1 \times 10^6$) were seeded into 6-well plates and incubated for 24 h before treatment with 50 μM STK793590 for 3 h. Following this the cells were treated with 1 mM

hydrogen peroxide ($H_2O_2$) for 4 h. Next, total RNA was extracted and reverse transcribed and mRNA expression for DJ-1, HO-1, NQO1 and Nrf2 measured by RT-qPCR. **A)** DJ-1 **B)** Nrf2 **C)** NQO1 **D)** HO-1. Results were normalised to GAPDH and presented as fold expression increase in mRNA relative to the untreated control. Representative of three independent experiments (N=3) and statistical analysis was done by one-way ANOVA and post hoc analysis via Tukey's test (P*≤0.05, P**≤0.01, P***≤0.001, P****≤0.0001). Data is shown as mean ± SEM.

## 3.2 Development and optimisation of 3D melanoma models

### *3.2.1 Development and optimisation of a Matrigel Matrix model*

Thus far, experiments for this project have been performed utilising 2D cell culture. 2D cell culture is known to have limitations in comparison to 3D cell culture as discussed in Section **1.2.3**. Several 3D models have been described for melanoma cancer. In the following section, three are compared in order to decide which would be the most advantageous for investigating DJ-1 in 3D culture. The first 3D model investigated involved seeding cells in a Matrigel Matrix basement membrane.

Different seeding densities ($0.1 \times 10^4$, $0.5 \times 10^4$, and $1 \times 10^4$ cells/well) were prepared, resuspended in Matrigel Matrix and transferred onto glass coverslips in a 12-well plate as 10 µL drops. 100 µL of media was evenly distributed on top of each Matrigel Matrix drop and the plate was incubated at 37 °C and 5% $CO_2$ in a humidified environment over 12 days. Media over the Matrigel Matrix drops was changed every 3 days.

**Figure 21A** shows A375 tumouroid growth in Matrigel Matrix over 9 days at the 3 different seeding densities mentioned above. By day 6, 3D tumouroid structures formed from all three seeding densities, with the largest average tumouroid area formed from $1 \times 10^4$ cells/well (3973.26 µm$^2$) (**Figure 21B**). However, by day 9 it was very difficult to decipher tumouroid structures at all three seeding densities due to overgrowth of the cell monolayer on the glass coverslips (**Figure 21A**). From the few tumouroids that could be deciphered, areas did decrease in size slightly for $0.1 \times 10^4$ and $1 \times 10^4$ cells/well by day 9 (**Figure 21B**). No further changes in tumouroid growth were observed for any of the seeding densities past day 9 of culture.

The main issue faced with this method included 2D monolayer overgrowth of A375 cells on the glass coverslips due to their high proliferation rate, which caused difficulties in observing 3D tumouroid structures.
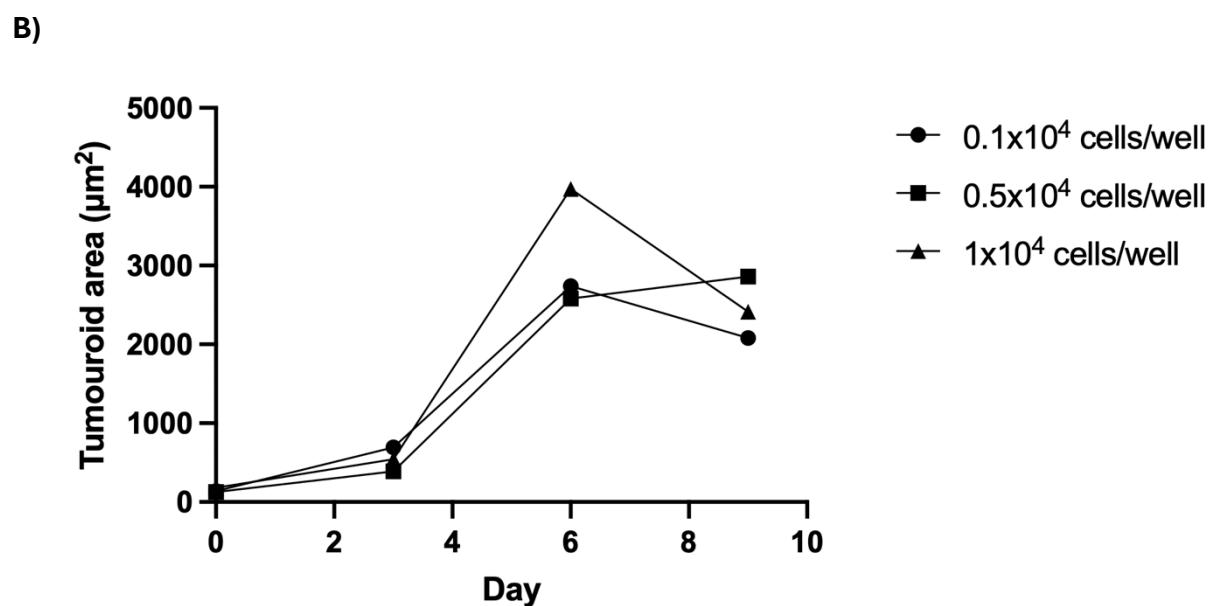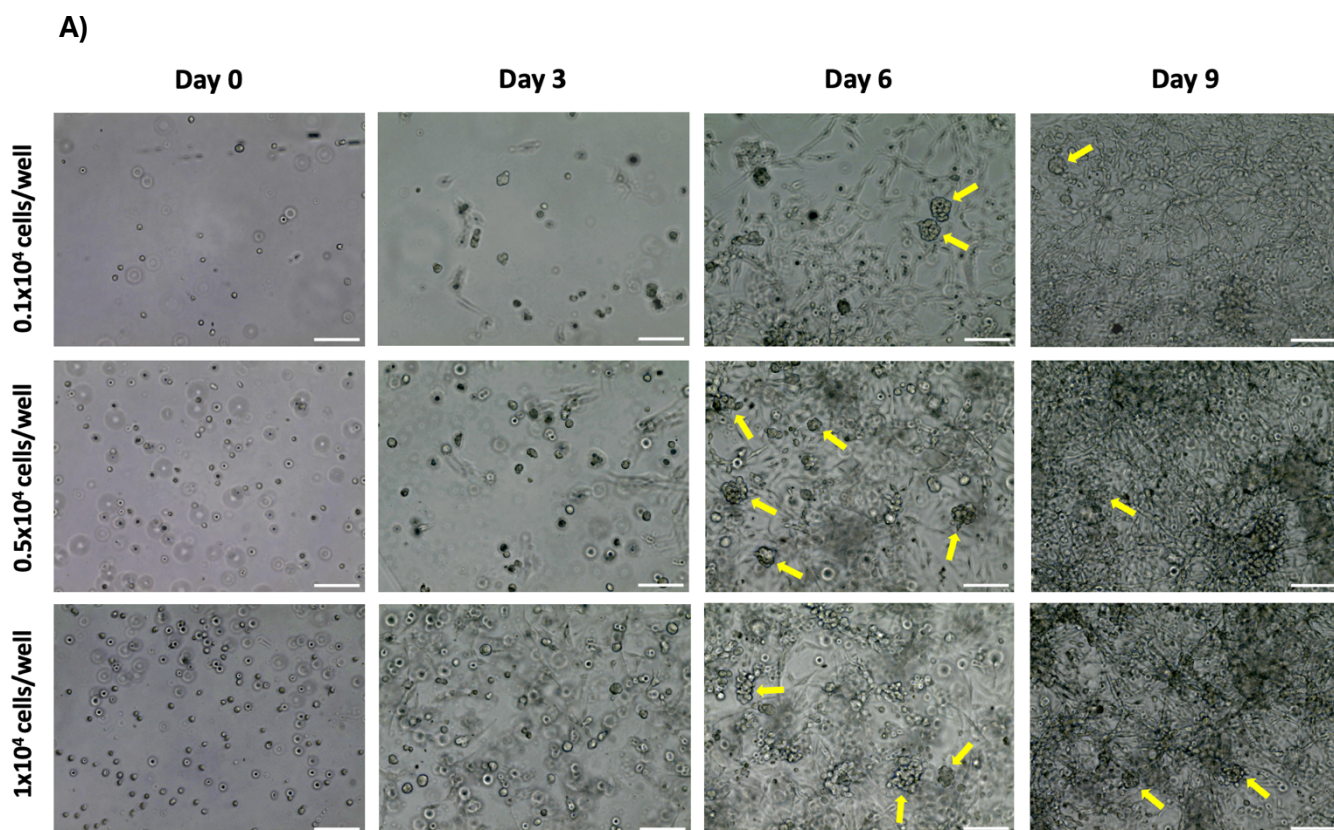
**Figure 21 – A375 3D tumouroid generation in Matrigel Matrix.** A375 cells were suspended in Matrigel Matrix at seeding densities of 0.1x10$^4$, 0.5x10$^4$ and 1x10$^4$ cells/well in 12-well plates and left to incubate over 12 days. **A)** Representative EVOS white light microscopy images of tumouroids from days 0, 3, 6 and 9 of culture. Images were taken every 3 days. Some of the tumouroids that formed are indicated by yellow arrows. Images are representative of one independent experiment (N=1) done in duplicate and were analysed in ImageJ. Scale bar 100 μm. **B)** Average growth of tumouroids at seeding densities 0.1x10$^4$, 0.5x10$^4$ and 1x10$^4$ cells/well on days 0, 3, 6 and 9 corresponding to **A**. Representative of one independent experiment (N=1) and analysed using ImageJ.

*3.2.2 Development and optimisation of a 'hanging drop' model*

The second 3D model investigated involved culturing cells via the 'hanging drop' method. A375 cell suspensions of seeding densities $0.1\times10^4$, $0.5\times10^4$, and $1\times10^4$ cells/drop were prepared. These were centrifuged, the supernatants removed (however leaving 5 μL behind) and cell pellets resuspended in fresh media. 10 μL drops of each were then transferred onto the underside of a petri dish lid, which was inverted and incubated at 37 °C and 5% $CO_2$ in a humidified environment for 12 days.

**Figure 22A** shows that tumouroids were formed over 9 days at the three seeding densities mentioned above. It took 3 days for cells to settle and by day 9, large 3D A375 tumouroid structures were formed from the larger seeding densities ($0.5\times10^4$ and $1\times10^4$ cells/drop) (**Figure 22A and B**). The tumouroid formed from $0.1\times10^4$ cells/drop by day 9 was smaller in comparison. In addition to this, the shapes of the structures varied between each of the seeding densities. Between days 3 and 6, the tumouroids formed from all three seeding densities increased in size; however, between days 6 and 9 their sizes decreased. No further changes were observed in the structures at any of the seeding densities past day 9 of culture.

One of the main issues that was faced with this 3D model was tumouroid disruption. For instance, if the petri dish was knocked whilst in the incubator some tumouroids broke apart. Replenishment of the media also disrupted the tumouroid structures. Transferring the tumouroids into a 96-well plate with the idea in mind to perform future experiments likewise resulted in the disruption of the tumouroid structures.

**A)**



**B)**
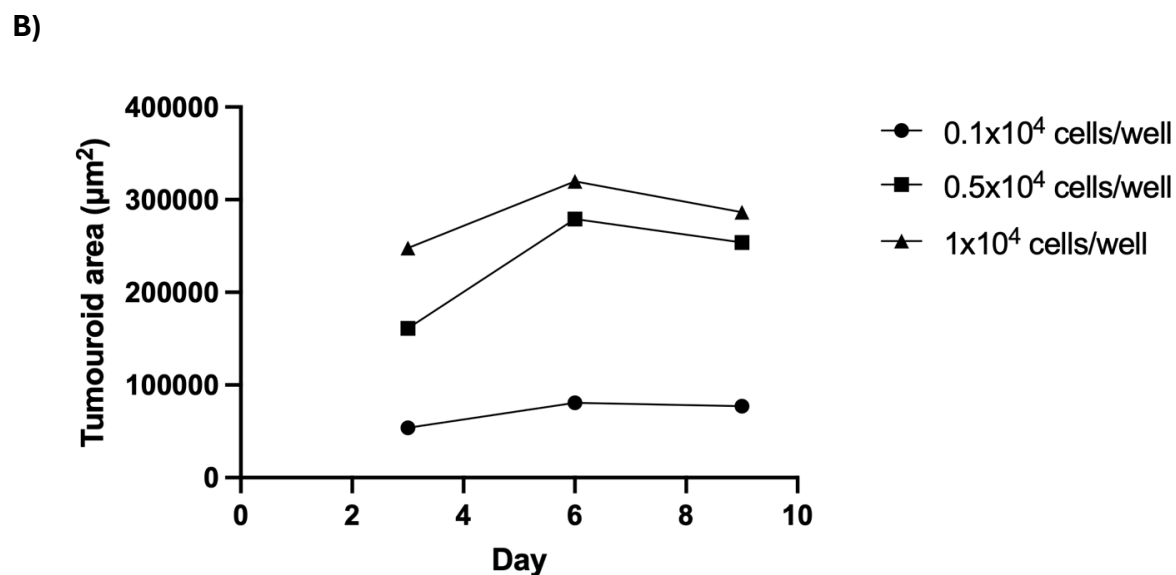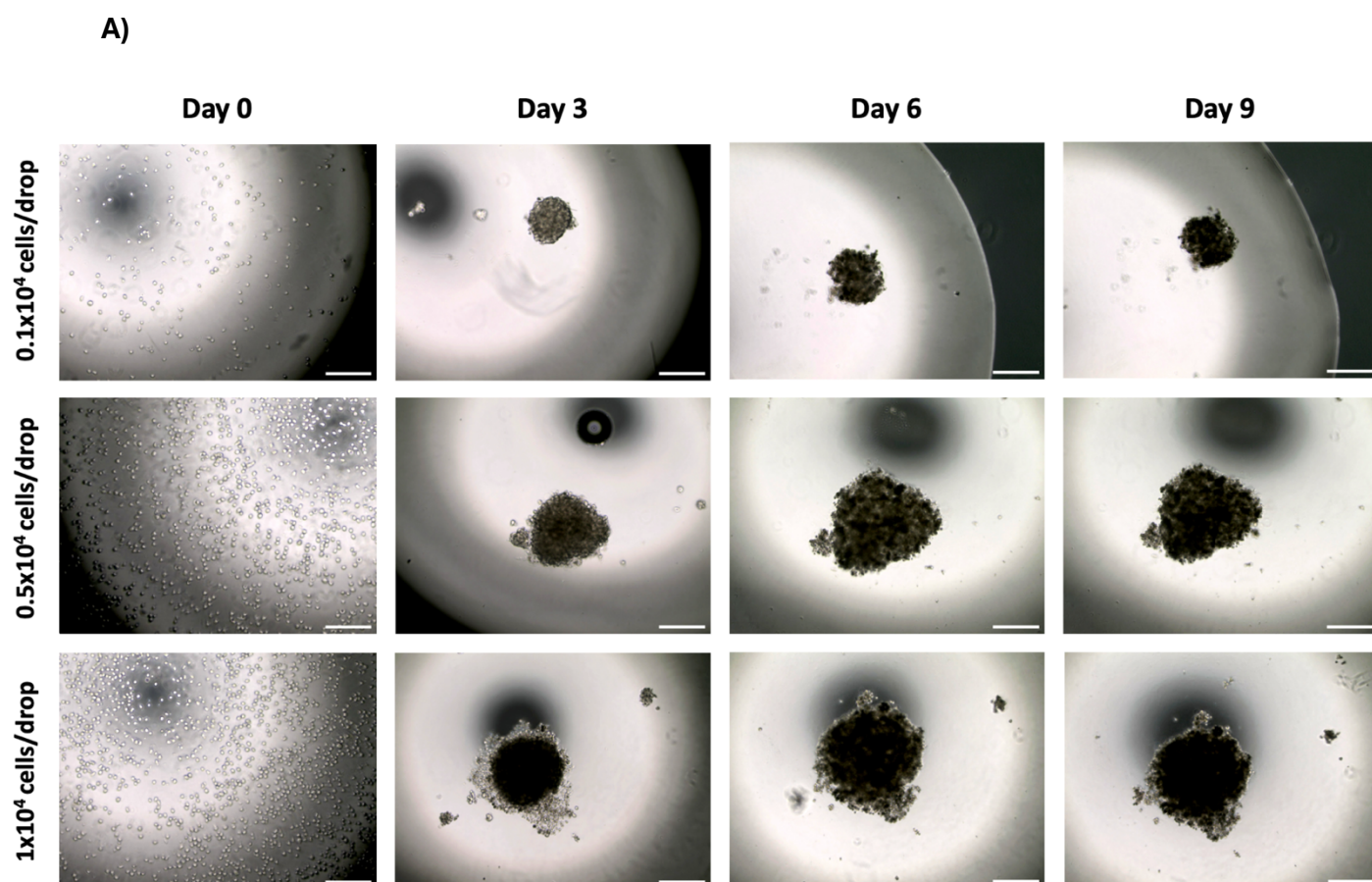


**Figure 22 – A375 3D tumouroid generation via the 'hanging drop' method.** A375 cells were cultured in 10 µL media drops on the underside of a petri dish lid. Seeding densities of $0.1\times10^4$, $0.5\times10^4$ and $1\times10^4$ cells/drop were used. Tumouroids were grown over 12 days. **A)** Representative EVOS white light microscopy images of tumouroids from days 0, 3, 6 and 9 of culture. Images were taken every 3 days. Images are representative of one independent experiment (N=1) done in duplicate and were analysed in ImageJ. Scale bar 100 µm. **B)** Growth of tumouroids at seeding densities $0.1\times10^4$, $0.5\times10^4$ and $1\times10^4$ cells/well on days 3,

6 and 9 corresponding to **A**. Representative of one independent experiment (N=1) and analysed using ImageJ.

### *3.2.3 Development and optimisation of a ULA model*

The final 3D model tested involved culturing cells in ultra-low adherence (ULA) plates. A375 cells were seeded in 96-well ULA U-bottom plates at densities of $0.1 \times 10^4$, $0.2 \times 10^4$ and $0.5 \times 10^4$ cells/well in 200 µL of media, spun down and incubated at 37 °C and 5% $CO_2$ in a humidified environment for 12 days. It was not possible to grow tumouroids at a seeding density of $1 \times 10^4$ cells/well (as was able for the previous two models), since the tumouroids would have grown too large, so it was opted to use a seeding density of $0.2 \times 10^4$ cells/well instead. Tumouroids were also cultured in 100 µL of media, but this resulted in disruption of the tumouroid structures during media changes, which were performed every 3 days.

**Figure 23A** shows A375 tumouroid formation and growth in ULA plates over 9 days at the three seeding densities mentioned above. It took 3 days for cells to settle and by day 9, large spherical 3D tumouroid structures formed from each seeding density, with $0.5 \times 10^4$ cells/well resulting in the largest tumouroid structure areas ($855598.29$ µm$^2$). It is further seen that for each seeding density tested, the size of the tumouroid structure increased as the days progressed starting from day 3 (**Figure 23A and B**). No further changes in tumouroid sizes at any of the three seeding densities were seen past day 9 of culture.

One of the main issues faced with this 3D model was dust getting inside the wells during plate centrifugation. The plates were parafilmed to try and avoid this but unfortunately dust contamination persisted. To avoid dust contamination in future experiments, centrifuging would be omitted, as the cells can also aggregate naturally in the plates.
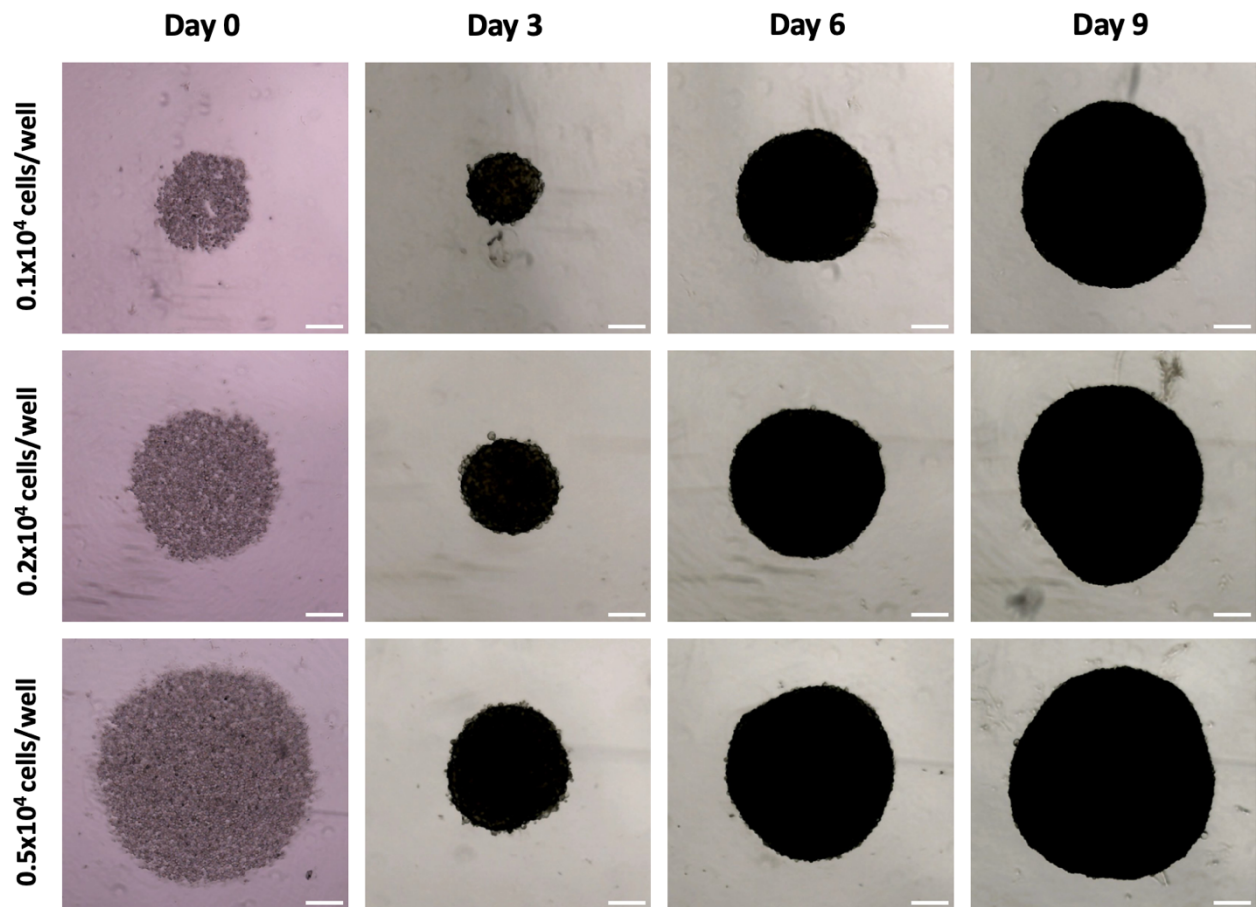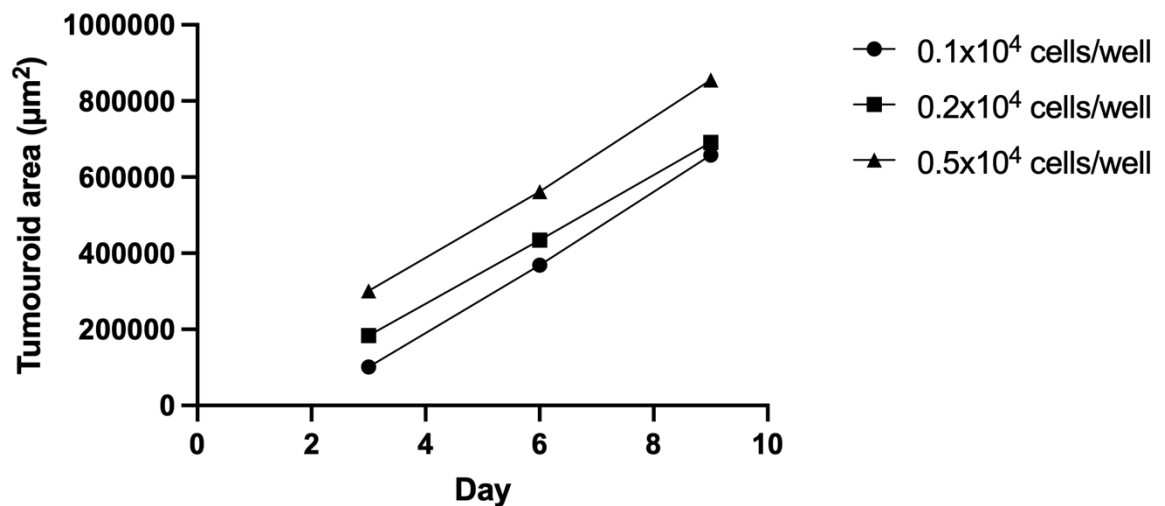
**Figure 23 – A375 ULA 3D tumouroid generation.** A375 cells were seeded in 96-well ULA U-bottom plates at densities of $0.1 \times 10^4$, $0.2 \times 10^4$ and $0.5 \times 10^4$ cells/well in 200 µL of media and left to incubate over 12 days. **A)** Representative EVOS white light microscopy images of tumouroids from days 0, 3, 6 and 9 of culture. Images were taken every 3 days. Images are representative of one independent experiment (N=1) done in triplicate and were analysed in ImageJ. Scale bar 100 µm. **B)** Growth of tumouroids at seeding densities $0.1 \times 10^4$, $0.2 \times 10^4$ and $0.5 \times 10^4$ cells/well on days 0, 3, 6 and 9 corresponding to **A**. Representative of one independent experiment (N=1) and analysed using ImageJ. Day 0 tumouroid area values were excluded

from graph to minimise any confusion about decrease in areas at the start of the experiment, due to cell settling time.

Various advantages and disadvantages of each examined 3D model became evident during the development and optimisation process (see **Section 4** for more detail). The Matrigel Matrix model had issues with overgrowth of A375 cells, making it difficult to observe and monitor tumouroids past day 6, however it was a model that had a biomimicry to the extra cellular matrix making it most representative of cell behaviour and tissue organisation. The 'hanging drop' model was the least expensive out of the 3 models, but there were issues with tumouroid structure disruption. Lastly, the ULA model had issues with dust contamination, however it was the model easiest to set up, there were no problems with tumouroid disruption, and it was easy to track and compare sizes of various tumouroids. Since the tumouroids also grew in a 96-well plate, this would later allow for easy high throughput experiments for closer study of DJ-1. As a result, the ULA model was concluded to be the best for culturing A375 tumouroids going forward.

### 3.2.4 Assessing ULA tumouroid response to drug treatment

Once the ULA method was chosen, the next stage assessed the impact of drug treatment on tumouroid growth. The goal of this stage was to determine if the tumouroids would react to general drug treatments so that future 3D experiments involving DJ-1 inhibitor, STK793590, could be carried out.

A375 cells were seeded in a 96-well ULA U-bottom plate at a density of $0.1 \times 10^4$ cells/well in 200 μL of media. $0.1 \times 10^4$ cells/well was chosen as the seeding density going forward as it provided tumouroids that were large enough, but not too large that any changes would go unnoticed (**Figure 23A**). The cells were left to incubate and settle for 3 days to allow for tumouroid formation and on day 4 of culture the tumouroids were treated with either DMSO (vehicle control), 1 μM or 5 μM staurosporine (STS) positive control or 1 μM or 10 μM vemurafenib. STS is a non-specific kinase inhibitor known to induce apoptosis in A375 cells, whereas vemurafenib is a BRAF inhibitor[107,220]. Day 4 was chosen as the treatment start day as by that point tumouroid formation could be confirmed by the appearance of a darker core and defined edges. The tumouroids were then left to incubate with media changes conducted every 3 days or treated everyday (continuously) with the drugs until day 9.

**Figures 24 and 25A** show that by day 9, A375 cells treated continuously with the DMSO control formed a large tumouroid (455599.8 μm$^2$). Following continuous treatment with 1 or 5 μM STS, A375 cells formed smaller tumouroids by days 7 and 9 in comparison to the DMSO control. The same was seen with 1 or 10 μM vemurafenib treatment. Interestingly, by day 9, 5 μM STS did not reduce A375 tumouroid growth more than 1 μM STS, suggesting

a non-concentration-dependent trend, however, STS most likely already reached its maximal response at both concentrations. On the other hand, 10 µM vemurafenib reduced A375 tumouroid growth more than 1 µM vemurafenib by day 9, indicating a concentration-dependent trend. Furthermore, 10 µM vemurafenib reduced A375 tumouroid growth to a similar extent as 1 and 5 µM STS. Corresponding phenomena are evident in the fold change results shown in **Figure 25B**. Cells disassociating or 'shedding' from the main tumouroid is also seen with 5 µM STS or 10 µM vemurafenib treatment (**Figure 24**). Results were similar when tumouroids were treated only once on day 4 with the two drugs [**Appendix 5.2**].
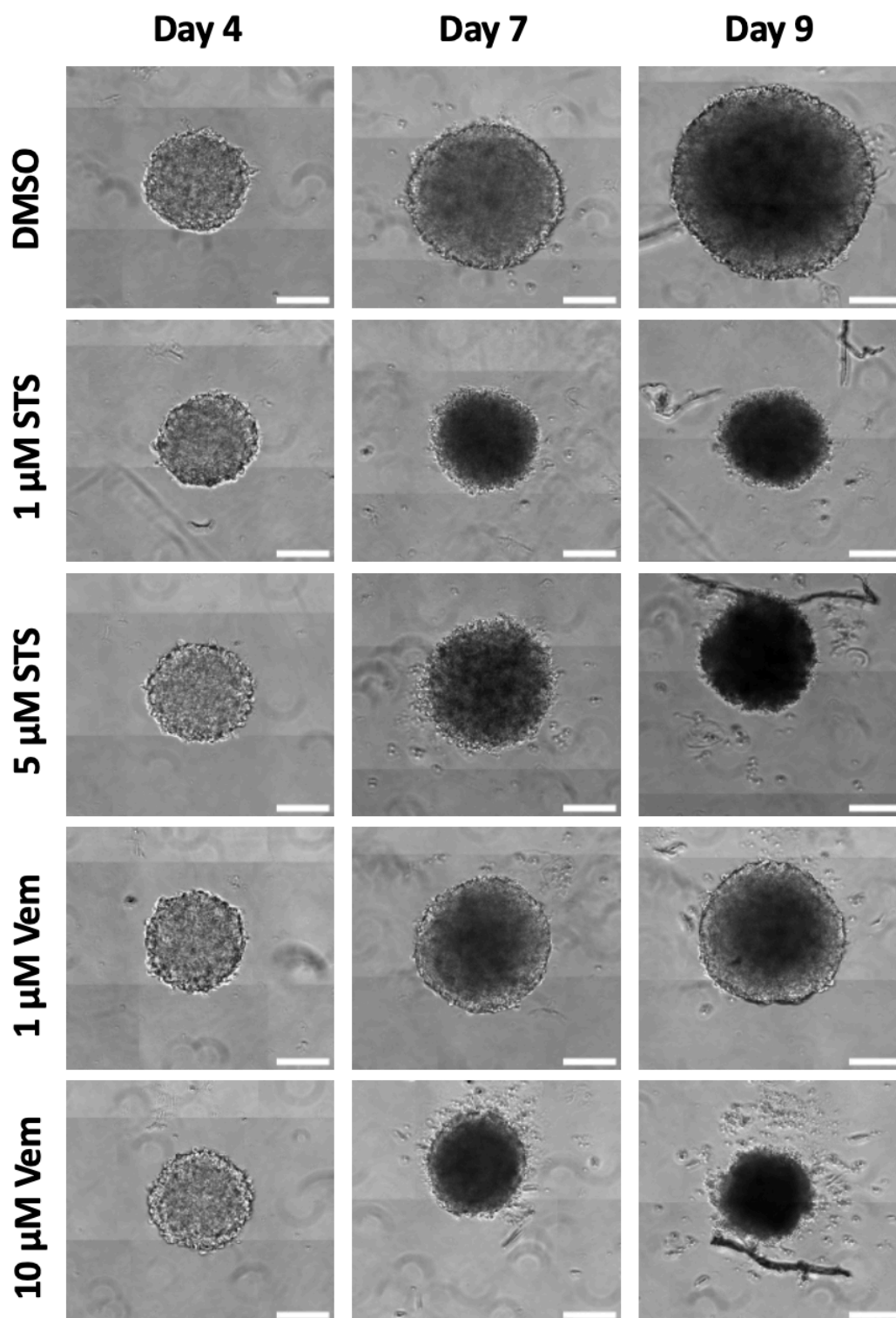
**Figure 24 – Vemurafenib and staurosporine (STS) reduce A375 ULA tumouroid growth.** A375 cells were seeded at a density of 0.1x10$^4$ cells/well in a 96-well ULA U-bottom plate and left to incubate and settle for 3 days to allow tumouroid formation. Continuous treatment with 1 μM or 5 μM staurosporine (STS) or 1 μM or 10 μM vemurafenib began on day 4, and tumouroids were treated every day until day 9. Zeiss Observer white light microscopy images from days 4, 7 and 9 of culture are shown here, are representative of one independent experiment (N=1) done in triplicate and were analysed in ImageJ. Scale bar 100 μm.
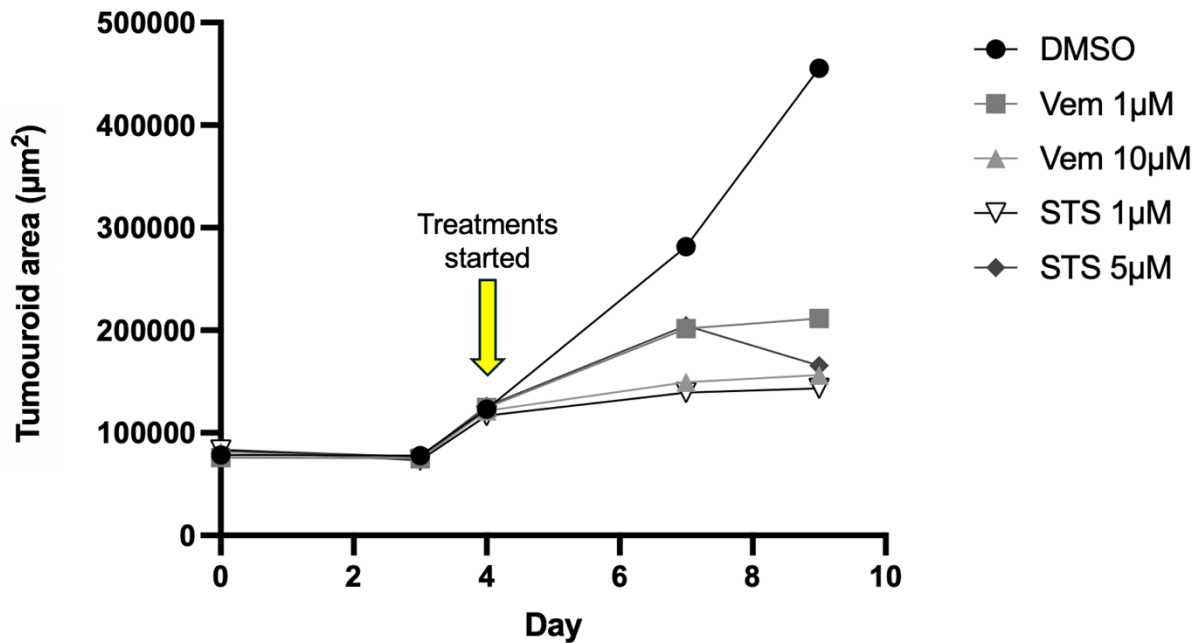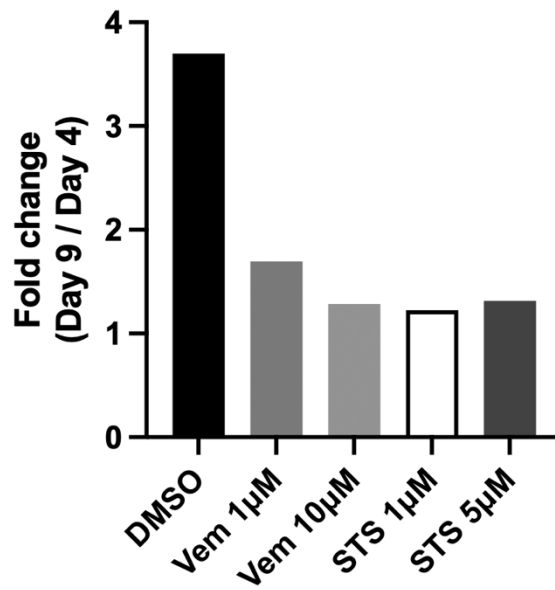
**Figure 25 – Effects of continuous vemurafenib and staurosporine (STS) treatment on A375 ULA tumouroid growth.** A375 cells were seeded at a density of $0.1 \times 10^4$ cells/well in a 96-well ULA U-bottom plate and left to incubate and settle for 3 days to allow tumouroid formation. Continuous treatment with 1 µM or 5 µM staurosporine (STS) or 1 µM or 10 µM vemurafenib began on day 4, and tumouroids were treated every day until day 9. **A)** Average area of tumouroid growth over 9 days with continuous treatment of 1 µM or 5 µM staurosporine (STS) or 1 µM or 10 µM vemurafenib beginning on day 4 of culture. Tumouroid area was calculated using ImageJ analysis of Zeiss Observer white light microscopy images. Results are presented as mean area ($\mu m^2$) and representative of one independent experiment (N=1). **B)** Fold change results from day 9 versus day 4 of growth of A375 tumouroids in **A**. Results are representative of one independent experiment (N=1).

This initial drug optimisation experiment confirmed that A375 ULA tumouroids react to drug treatment, allowing the project to pursue 3D experiments involving DJ-1 inhibitor, STK793590. **Figure 26** summarises the entire development and optimisation process for A375 ULA tumouroid STK793590 and vemurafenib combination experiments.
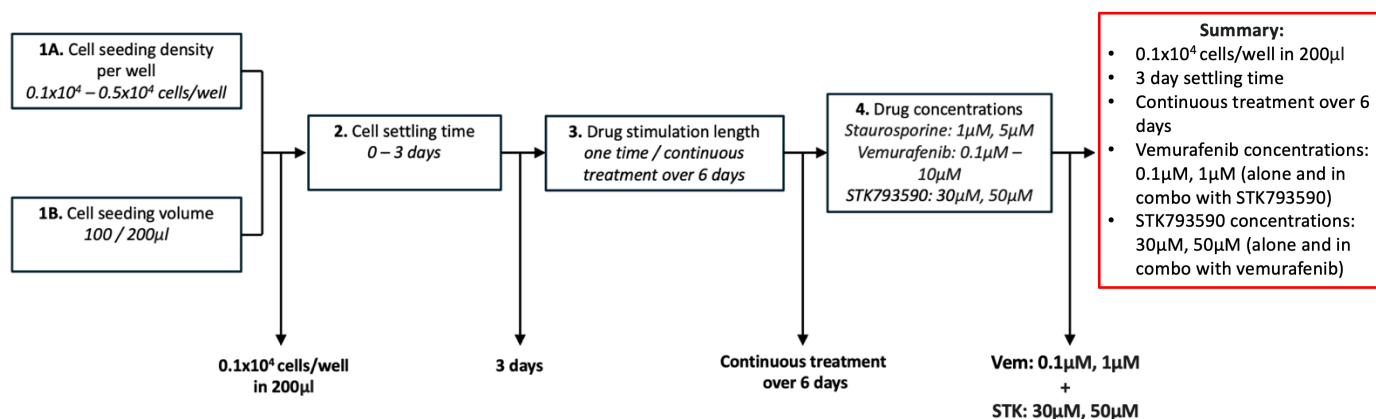


**Figure 26 – Development and optimisation process for A375 ULA tumouroids.**

### 3.3 Targeting DJ-1 in a 3D melanoma model

*3.3.1 Effects of STK793590 in combination with vemurafenib on ULA tumouroid growth*

In 2D cell culture, STK793590 in combination with vemurafenib significantly decreased A375 cell viability (**Figure 19**) and therefore this effect was next investigated in the tumouroids.

A375 cells were seeded in a 96-well ULA U-bottom plate at a density of $0.1 \times 10^4$ cells/well in 200 µL of media. On day 4 the tumouroids were treated with different combinations of 50 µM STK793590 and 0.1 µM or 1 µM vemurafenib. DMSO was included as the vehicle control. The tumouroids were then left to incubate until day 9, with media changes conducted every 3 days, or treated everyday (continuously) with the drugs until day 9.

**Figures 27 and 28A** show that by day 9, large tumouroid structures formed from A375 cells treated continuously with the DMSO control, 50 µM STK793590 or 0.1 µM vemurafenib. Cells treated with 1 µM vemurafenib resulted in a much smaller tumouroid in comparison, suggesting that this singular treatment had a larger inhibitory effect on tumouroid growth compared to the others. 50 µM STK793590 + 0.1 µM vemurafenib treated cells resulted in a larger sized tumouroid compared to 1 µM vemurafenib treated cells, however smaller than the tumouroids formed from the DMSO control, 50 µM STK793590 or 0.1 µM vemurafenib treated cells. 50 µM STK793590 + 1 µM vemurafenib treated cells resulted in a similar sized tumouroid to 1 µM vemurafenib treated cells.

**Figure 28B** shows that 50 µM STK793590 + 1 µM vemurafenib treated A375 cells exhibited the most statistically significant decrease in tumouroid growth compared to the rest of the conditions, however, no significant difference was seen between 1 µM vemurafenib and 50 µM STK793590 + 1 µM vemurafenib treated tumouroids. This suggests the combination is not more effective than vemurafenib on its own, contrasting the results obtained in the 2D culture experiment (**Section 3.1.6**). Interestingly, 50 µM STK793590 + 0.1 µM vemurafenib treated tumouroids showed a statistically significant decrease in tumouroid growth compared to 0.1 µM vemurafenib treated tumouroids, also seen in the 2D culture results in **Section 3.1.6**. Finally, cell 'shedding' is seen with 50 µM STK793590, 1 µM vemurafenib and the combination treatment (**Figure 27**).

Results for A375 ULA tumouroids treated continuously with 30µM STK793590 in combination with vemurafenib were also obtained, however no significant differences were seen to that of the results with 50µM STK793590 treatment [**Appendix 5.2**]. In addition to this, no significant differences were seen for one-time treatment of A375 ULA tumouroids treated with 30µM or 50µM STK793590 in combination with vemurafenib; the only differences seen were that some tumouroids grew to larger sizes by day 9 compared to continuously treated tumouroids [**Appendix 5.2**].
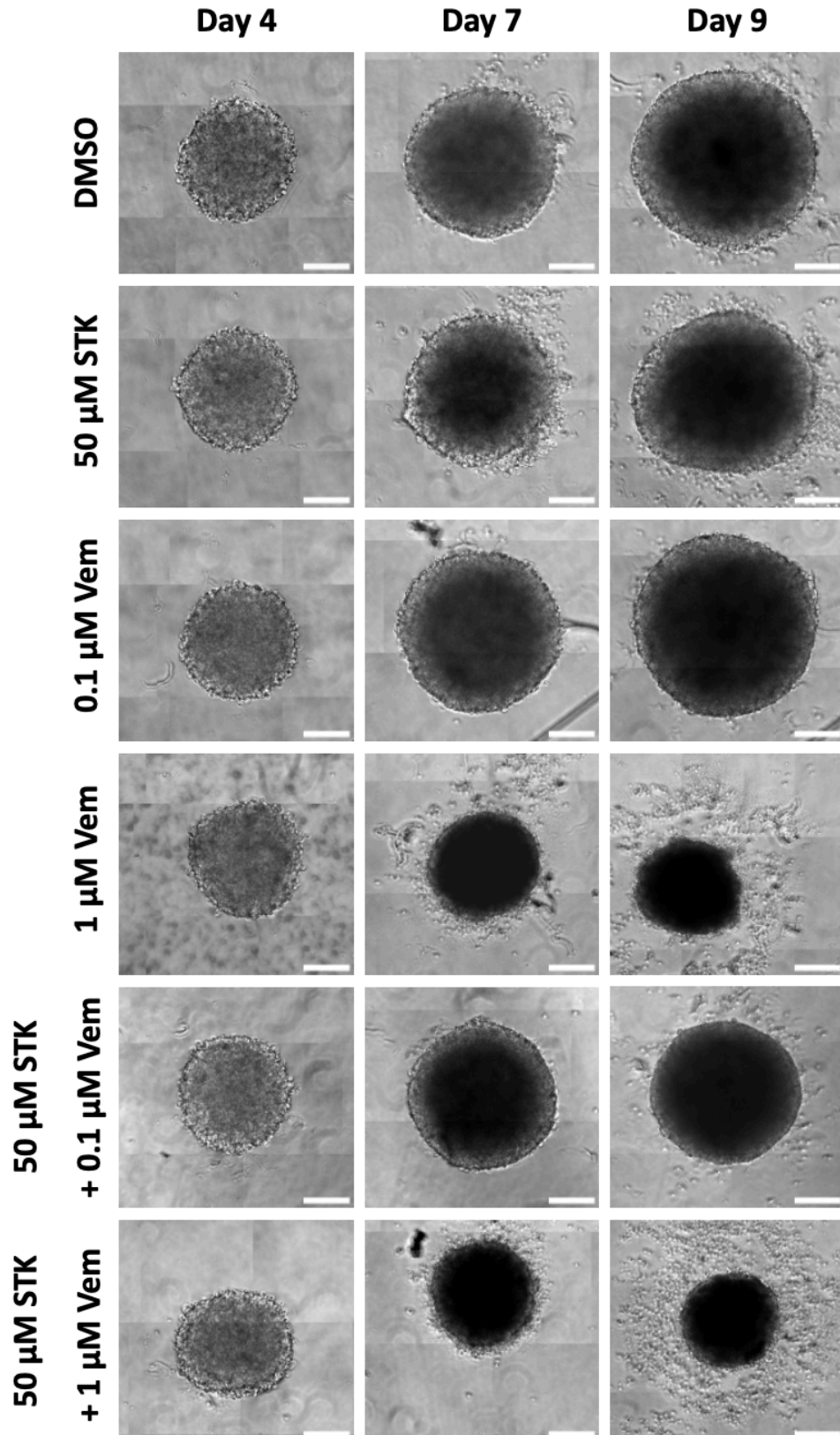
**Figure 27 – Continuous treatment of vemurafenib on its own and 50 µM STK793590 in combination with vemurafenib supress A375 ULA tumouroid growth.** A375 cells were seeded at a density of $0.1 \times 10^4$ cells/well in a 96-well ULA U-bottom plate and left to incubate and settle for 3 days to allow tumouroid formation. Continuous treatment with 0.1 µM or 1 µM vemurafenib or 50 µM STK793590 and combinations

of these treatments began on day 4, and tumouroids were treated every day until day 9. Zeiss Observer white light microscopy images from days 4, 7 and 9 of culture are shown here, are representative of three independent experiments (N=3) and were analysed in ImageJ. Scale bar 100 µm.

**A)**
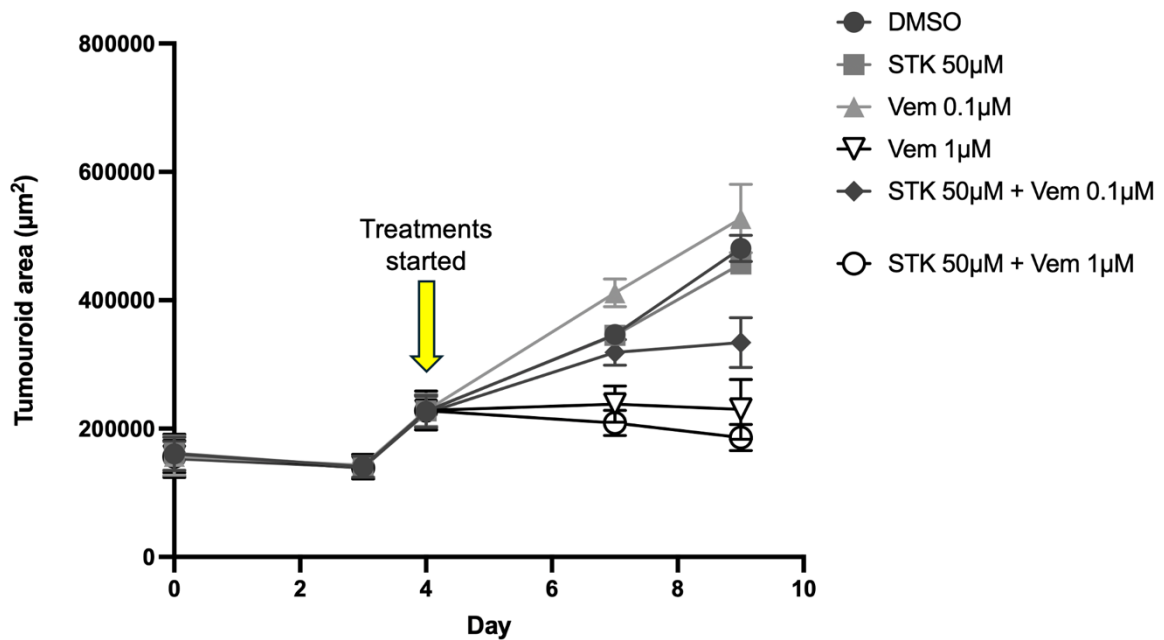


**B)**
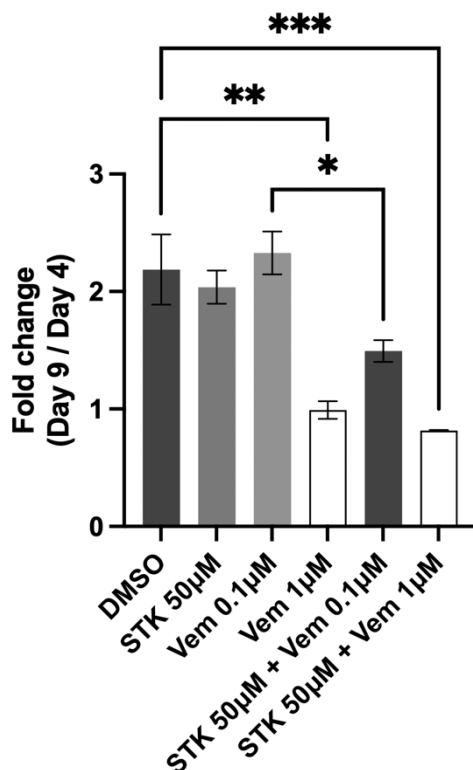


**Figure 28 – Effects of vemurafenib treatment and 50 µM STK793590 in combination with vemurafenib on A375 ULA tumouroid growth.** A375 cells were seeded at a density of $0.1\times10^4$ cells/well in a 96-well ULA U-bottom plate and left to incubate and settle for 3 days to allow tumouroid formation. Continuous treatment with 0.1 µM or 1 µM vemurafenib or 50 µM STK793590 and combinations of these treatments began on day 4, and tumouroids were treated every day until day 9. **A)** Average area of tumouroid growth

over 9 days with continuous treatment of 0.1 µM or 1 µM vemurafenib or 50 µM STK793590 and combinations of these treatments beginning on day 4 of culture. Tumouroid area was calculated using ImageJ analysis of Zeiss Observer white light microscopy images. Results are presented as mean area (µm$^2$) and representative of three independent experiments (N=3). Statistical analysis was done by one-way ANOVA and post-hoc analysis via Tukey's test (P*≤0.05, P**≤0.01, P***≤0.001, P****≤0.0001). Data is shown as mean ± SEM. **B)** Fold change results from day 9 versus day 4 of growth of A375 tumouroids in **A**. Results are representative of three independent experiments (N=3). Statistical analysis was done by one-way ANOVA and post-hoc analysis via Tukey's test (P*≤0.05, P**≤0.01, P***≤0.001, P****≤0.0001). Data is shown as mean ± SEM.

This experiment was also conducted in A375 Matrigel Matrix tumouroids however only with 50 µM STK793590 and 1 µM vemurafenib concentrations to compare to the ULA method [**Appendix 5.2**]. The results obtained showed that vemurafenib alone had the greatest effect in decreasing A375 Matrigel Matrix tumouroid growth. The combination resulted in larger Matrigel Matrix tumouroids compared to vemurafenib alone, in contrast to the ULA results.

### 3.3.2 Effects of STK793590 in combination with vemurafenib on cell viability of ULA tumouroids

Since STK793590, vemurafenib and combinations of these two drugs decreased A375 ULA tumouroid growth, the effects of these drugs on tumouroid cell viability were investigated. This was achieved via fluorescence microscopy. On day 9 of tumouroid culture, after treatments with STK793590 (30 µM or 50 µM) and vemurafenib (0.1 µM or 1 µM) had been completed, a LIVE/DEAD® viability/cytotoxicity dye was added to the tumouroids for 45 mins. Following this, the tumouroids were viewed under a fluorescence microscope to visualise live and dead cells.

**Figure 29** shows the results which were obtained for day 9 A375 ULA tumouroids after incubation with LIVE/DEAD® viability/cytotoxicity dye. The tumouroids had previously been treated with 50 µM STK793590, 0.1 µM or 1 µM vemurafenib and combinations of both drugs. **Figure 29** shows that there were live and dead A375 cells present in every tumouroid regardless of what they had been treated with. It is further seen that live A375 cells were concentrated around the outside of all the tumouroid structures, and that no green labelling was picked up in the cores of some of the larger tumouroids, suggesting that there were no live cells in the middle of these structures. A possible explanation for this could be that the calcein-AM was unable to permeate through to the cores of the tumouroids (red labelling of the tumouroids was not particularly high either, suggesting that ethidium homodimer-1 likewise struggled to permeate some of the tumouroids).

**Figure 30** indicates that 0.1 µM vemurafenib treated tumouroids had the highest ratio of live to dead cells, whereas 1 µM vemurafenib, and 50 µM STK793590 + 1 µM vemurafenib treated tumouroids had the lowest ratio of live to dead cells. This suggests that the least

cell death was occurring in 0.1 µM vemurafenib treated tumouroids, and that the most cell death was occurring in 1 µM vemurafenib and 50 µM STK793590 + 1 µM vemurafenib treated tumouroids. Similar LIVE/DEAD ratios were obtained for the DMSO control, 50 µM STK793590 and 50 µM STK793590 + 0.1 µM vemurafenib treated tumouroids. The result for 0.1 µM vemurafenib treated tumouroids is unforeseen as it would have been expected that they would have had more cell death occurring compared to the DMSO control. It is important to note that there are some limitations of the LIVE/DEAD image analysis which could have impacted the quantification of the tumouroids. For instance, the tumouroid images were taken as single focal plane images, meaning that cells above or below the focal plane were missed and due to heterogeneous viability across the core and periphery of the tumouroids, a biased LIVE/DEAD ratio could have been obtained. Errors from out-of-focus fluorescence and overlapping signals could also have been introduced, as well as skewed intensity-based measurements that depend on the chosen image slice.

Images and LIVE/DEAD ratios for tumouroids treated with 30 µM STK793590 in combination with vemurafenib were also obtained, however there were no significant differences to that of the results shown in **Figures 29 and 30** (see **Appendix 5.2**). This experiment was additionally conducted for A375 tumouroids cultured in Matrigel Matrix, however the images obtained could not be analysed properly due to background fluorescence being picked up from A375 cell monolayers growing on the surfaces of glass coverslips in the wells.
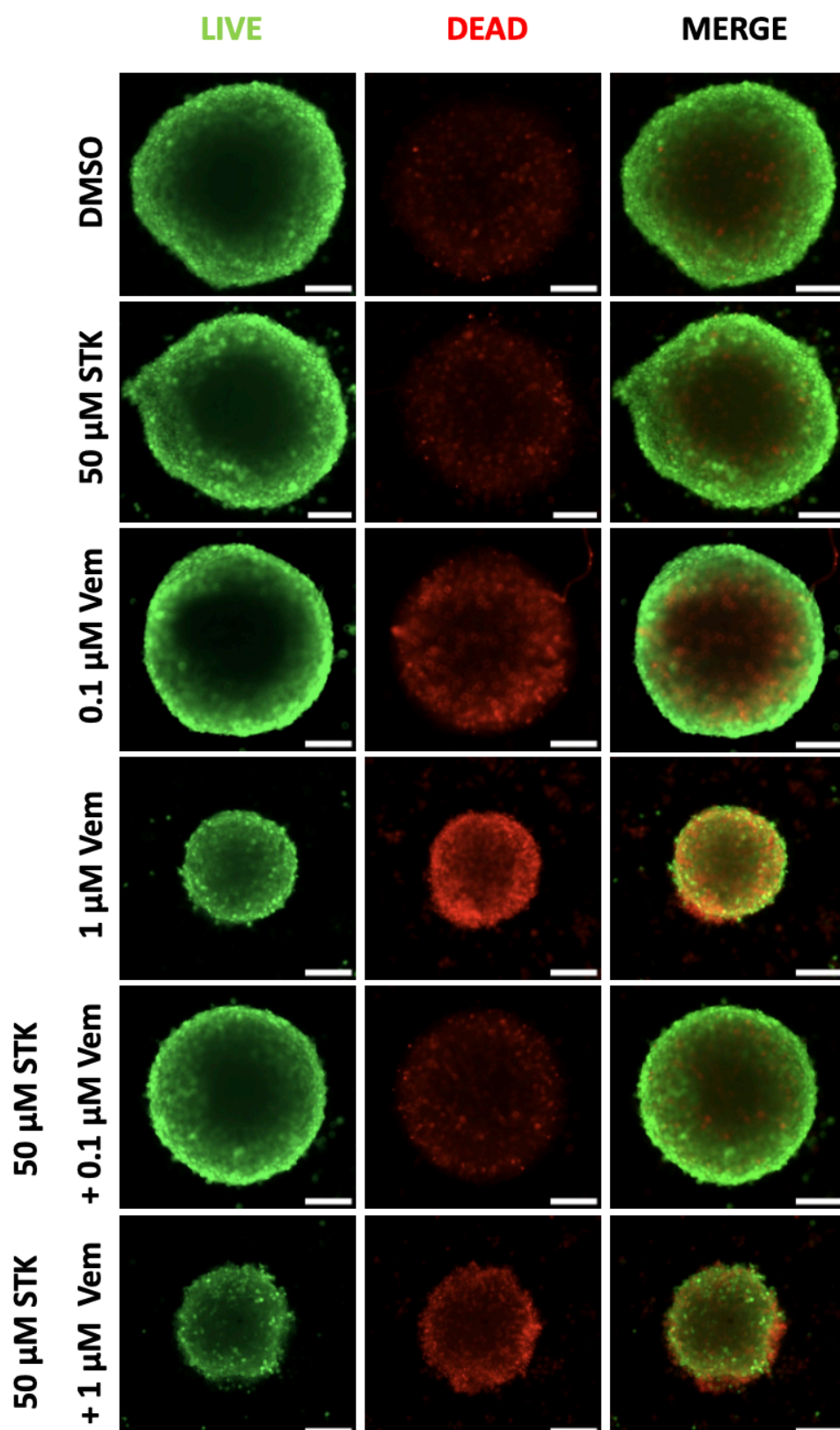
**Figure 29 – Effects of 50 µM STK793590 in combination with vemurafenib on A375 ULA tumouroid viability and cytotoxicity.** A375 cells were seeded at a density of 0.1x10⁴ cells/well in a 96-well ULA U-bottom plate and cultured for 3 days before being treated continuously with vemurafenib (0.1 or 1 µM) or STK793590 (50 µM) alone or in combination starting on day 4. They were left to incubate up to day 9 and

were treated every day. On day 9, the LIVE/DEAD® viability/cytotoxicity dye was incubated with the tumouroids for 45 mins and tumouroid viability and cytotoxicity was visualised via fluorescence microscopy. Zeiss Observer images were analysed in ImageJ and are representative of one independent experiment (N=1). Scale bar 100 µm.
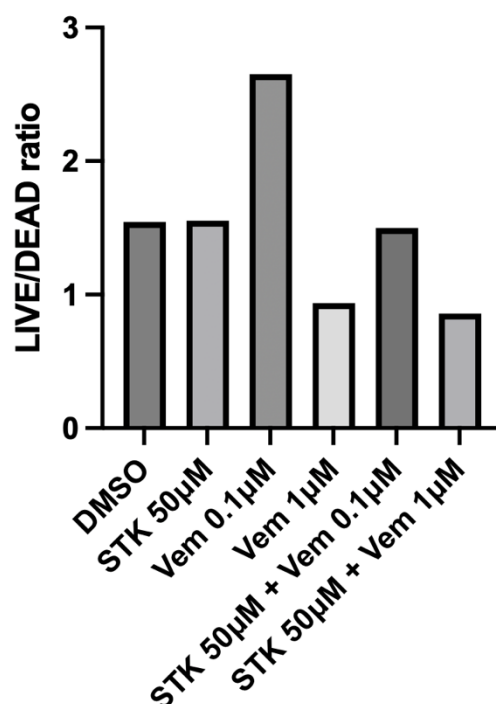


**Figure 30 – LIVE/DEAD ratio of 50 µM STK793590 in combination with vemurafenib on A375 ULA tumouroids.** A375 cells were seeded at a density of $0.1 \times 10^4$ cells/well in a 96-well ULA U-bottom plate and cultured for 3 days before being treated continuously with vemurafenib (0.1 or 1 µM) or STK793590 (50 µM) alone or in combination starting on day 4. They were left to incubate up to day 9 and were treated every day. On day 9, the LIVE/DEAD® viability/cytotoxicity dye was incubated with the tumouroids for 45 mins and tumouroid viability and cytotoxicity was visualised via fluorescence microscopy. LIVE/DEAD ratio was calculated using ImageJ. Results are representative of one independent experiment (N=1).

# 4. Discussion and Future Directions

Melanoma is the most lethal form of skin cancer. Immunotherapies or targeted chemotherapy, for example BRAF inhibitors, are given to patients in later stages of the disease to slow the spread, yet in many cases the melanoma becomes chemoresistant. Novel pharmacological strategies are therefore urgently needed to combat chemoresistance. DJ-1 (or PARK7) is a Parkinson's disease-associated protein and oxidative stress sensor, which can activate the redox-sensitive Nrf2 pathway. Recently, DJ-1 was reported to play a role in the progression of melanoma and chemoresistance, suggesting that it could be a novel therapeutic target for this cancer. There is also a current need to provide more precise representations of tumour microenvironment and biology through 3D tissue models (gaps in 3D melanoma DJ-1 research are also apparent). Therefore, this project aimed to investigate the role of DJ-1 and its potential as a therapeutic target in melanoma via 2D and 3D tissue models.

This project first explored DJ-1 protein expression in 4 different human melanoma cell lines. Results in **Figure 12** showed that the SK-MEL-28 cell line had the highest DJ-1 protein expression. A375 and MEL501 melanoma cell lines displayed similar DJ-1 protein expression lower than SK-MEL-28, yet higher than the UACC 1273 melanoma cell line. These findings correspond to work conducted by Quesnel *et al* (2024)[221], revealing SK-MEL-28 cells to be one of the highest DJ-1 expressing cell lines from a panel of investigated melanoma cell lines. They also discovered that A375 cells had less DJ-1 expression compared to SK-MEL-28 cells, further validating our results. Previous work conducted in the O'Connell lab additionally supported the results that were obtained. It is important to note that despite equal protein loading, DJ-1 expression varies between cell lines, representing the heterogenic nature of melanoma. Although DJ-1 expression in uveal melanoma cell lines was not investigated, it would be worth exploring this in any future work, as it has been reported that DJ-1 is highly expressed in metastatic uveal melanoma cells[178].

Visualising DJ-1 protein location was also conducted. Results in **Figure 13** demonstrated that DJ-1 is present in the cytoplasm and nuclei of A375 cells. This finding is supported by evidence from various studies confirming that DJ-1 is found in the cytoplasm, mitochondria and nuclei of various cells, including cancer cells[133,182,222,223]. There is additional evidence suggesting that DJ-1 location within cells changes in response to oxidative stress[133,223], however due to time constraints we were unable to study this in A375 cells. We would ensure to study this as part of any future work, potentially utilising confocal microscopy of pseudo-time images to track localisation of DJ-1, possibly in combination with mitochondrial and nuclear labelling. Furthermore, **Figure 13** shows that there is an uneven distribution of DJ-1 throughout each individual cell, with DJ-1 location presenting as peri-nuclear. This could suggest DJ-1's role as a transcriptional co-activator[141]. It can also be seen that DJ-1 is concentrated in certain points of A375 cell cytoplasmic protrusions, suggesting that DJ-1 may have a role in cell migration, and some studies have already explored this role, however in pancreatic cancer cells[133,224].

Following this experiment, DJ-1 knockdown was conducted in A375 cells. A375 cells were chosen to use for this as they had a higher proliferation rate compared to SK-MEL-28 cells, even though they expressed less DJ-1. It was found that DJ-1 knockdown decreased cell viability as shown in **Figure 16**, which is supported by Lago-Baameiro *et al*'s (2023)[206] work, which discovered that DJ-1 knockdown caused decreases in proliferation and invasion of uveal melanoma cells. Other research confirms that DJ-1 induces proliferation of cancer cells and suppresses apoptosis, suggesting that knockdown would thereby cause a decrease in cell proliferation/viability yet an increase in cell death[133,177]. In addition to this experiment, A375 cells were also treated with vemurafenib post DJ-1 knockdown, to determine any possible extra effects on cell viability. Results in **Figure 17** showed that there were no additional effects on A375 cell proliferation in the presence of vemurafenib following DJ-1 knockdown.

Knockdown experiments further revealed that siDJ-1 had no effect on mRNA levels of Nrf2 and two of its downstream target genes, NQO1 and HO-1 under both normal and oxidative stress conditions (see **Figure 18**). This finding was surprising, since DJ-1 is believed to enhance Nrf2 signalling by disrupting the interaction between Nrf2 and its negative regulator, Keap1. However, there is conflicting evidence surrounding this area of research. For instance, Clements *et al* (2006)[181] found that Nrf2 basal levels and Nrf2-dependent genes were affected by DJ-1 disruption in Huh7 cells derived from a male with hepatocellular carcinoma, whereas Gan *et al* (2012)[148] found the opposite to be true, however in neuronal cells. Gan *et al* (2012)[148] propose that the association between DJ-1 and Nrf2 is cell type specific, suggesting that this may also be true in melanoma. Aside from these results, hydrogen peroxide ($H_2O_2$) had no effect on mRNA levels of DJ-1 and Nrf2. These results are as expected since $H_2O_2$ predominantly alters DJ-1 and Nrf2 protein rather than directly modifying the genes themselves. A study conducted by Ning *et al* (2010)[225] also found that $H_2O_2$ had no effect on Nrf2 mRNA expression, supporting the results we obtained (although this was carried out in rat endothelial cells). No effect on NQO1 was also seen, which may or may not be as expected since there is evidence that $H_2O_2$ induces NQO1 expression, although the response may vary due to specific transcript variants or cell type[226,227]. However, $H_2O_2$ did cause a significant increase in HO-1 mRNA expression, which was as expected, as $H_2O_2$ is known to increase HO-1 expression[228,229].

This project also studied the role of DJ-1 in 2D using a DJ-1 inhibitor. The DJ-1 inhibitor used for this was STK793590, an isatin (1H-indole-2,3-dione) derivative discovered by Tashiro *et al* (2018)[136] (see **Section 1.3.5** for more detail). Previous work conducted in the O'Connell lab found that STK793590 inhibited A375 cell proliferation. This project investigated combining STK793590 with vemurafenib to determine whether this would have a greater inhibitory effect on A375 cell proliferation compared to vemurafenib alone. Vemurafenib was chosen as it is a BRAF inhibitor used in metastatic melanoma treatment, and A375 cells present with BRAF mutations[107,219]. Results in **Figure 19**

showed that STK793590 (50 µM) in combination with vemurafenib (1 µM) decreased cell proliferation by 58% compared to the DMSO control, and that this combination had a greater effect compared to 1 µM vemurafenib on its own (26% decrease in cell proliferation). The result obtained for 1 µM vemurafenib on its own corresponds to research done by Dratkiewicz *et al* (2019)[230]. STK793590 effects on mRNA expression of DJ-1 and Nrf2 along with its antioxidant downstream genes HO-1 and NQO1 under both normal and oxidative stress conditions were also explored. **Figure 20** results showed that STK793590 had no significant effects on mRNA expression of DJ-1, Nrf2, HO-1 or NQO1 under both normal and oxidative stress conditions. Protein expression of DJ-1 after STK793590 and $H_2O_2$ treatment were also obtained (see **Appendix 5.2**). Results indicated that STK793590 under normal or oxidative stress conditions (induced by $H_2O_2$) had no effects on DJ-1 protein levels, supporting the mRNA results. These results are surprising since STK793590 is thought to disrupt DJ-1 homodimer formation, rendering DJ-1 protein non-functional. Since non-functional proteins may be more susceptible to degradation, this can cause protein levels to drop[231].

To develop and optimise 3D *in vitro* models of melanoma for closer study of DJ-1, three 3D models involving culture of A375 cells were tested: the Matrigel Matrix model, the 'hanging drop' model and the ultra-low adherence (ULA) model (see **Section 3.2**). Various advantages and disadvantages of each examined 3D model became evident during the development and optimisation process (see **Table 10**). The Matrigel Matrix model allowed for many smaller sized tumouroids to form, which could potentially allow drugs to penetrate the centres/cores more easily as compared to the other models. It also presented a biomimicry to the extra cellular matrix, which the other models did not, therefore being more representative of cell behaviour and tissue organisation. Nevertheless, Matrigel Matrix is expensive and problems with A375 cell monolayer overgrowth on the glass coverslips occurred, making it difficult to analyse and keep track of individual tumouroids. In addition to this, the model was difficult to set up and work with due to the Matrigel Matrix solidifying quickly.

The 'hanging drop' model was cheap and simple to set up in comparison to the Matrigel Matrix model, however problems occurred with the tumouroid structures breaking up. The ULA model allowed for single uniform tumouroid shapes and sizes to form and as a result allowed easy analysis; it was easy to track and compare changes in growth. The model was also quick and easy to set up compared to the Matrigel Matrix method. Furthermore, there were no concerns about disrupting tumouroid structures (as compared to the 'hanging drop' model) and due to the tumouroids growing in a 96-well plate, this would later allow for easy high throughput experiments for closer study of DJ-1. However, this model was also expensive and dust contamination issues were encountered. In addition, the large size of the tumouroids formed may potentially hinder drug penetration into their cores, resulting in diminished therapeutic efficacy. Overall, results indicated that the ULA model proved to be the most favourable for continued

experiments involving DJ-1 as it had the simplest set-up and allowed for easy analysis of tumouroids. The ULA model was best suited for this project, however, groups conducting 3D experiments researching melanoma use various models depending on the experiment nature. For instance, Karimi *et al* (2023)[232] utilised 5D microplates for culture of human malignant melanoma WM266-4 tumouroids for development of positronium biomarkers, whereas Wagner and Koyasu (2020)[233] used a 'hanging drop' model to develop B16 melanoma tumouroids for co-culture experiments with immune cells to study tumour-immune cell interactions. Aside from these, Quesnel *et al* (2024)[221] utilised a 'hanging drop' model for SK-MEL-28 tumouroids when studying DJ-1 and $\alpha$-synuclein interactions in response to temozolomide treatment.

**Table 10 – Comparison of the advantages and disadvantages for 3D tumouroid models explored in this project**

| 3D tumouroid model | Advantages | Disadvantages |
|---|---|---|
| Matrigel Matrix | - Multiple tumouroids form<br>- Biomimicry to extra cellular matrix<br>- Potentially easier for drugs to get through as compared to ULA method since tumouroids are smaller in size | - Expensive<br>- Variation between the tumouroids in size and shape<br>- Inconsistent molecular composition<br>- Difficult to work with: had to work quickly when Matrigel Matrix was off the ice as it would solidify. Issues with overgrowth of A375 cell monolayers on glass coverslips were had which caused difficulties in visualising tumouroids |
| 'Hanging drop' | - Cheap<br>- Simple | - Variation between tumouroids in size and shape<br>- Tumouroids can break apart easily<br>- Difficult to work with: tumouroid structures were disrupted when petri dish was knocked, media changed or when attempting to transfer tumouroids into a 96-well plate |
| Ultra-Low Adherence (ULA) plate | - Uniform sizes and shapes (spheroids)<br>- Easy to compare sizes of tumouroids - easy analysis<br>- Easy and quick to set up<br>- High throughput | - Expensive<br>- Dust inside wells from plate centrifuge<br>- More difficult for drugs to penetrate all parts of a tumouroid (especially the core/centre), potentially resulting in lower drug efficacy |

The next stage of the optimisation process involved conducting initial drug test experiments in A375 ULA tumouroids, to determine whether they would respond to treatment. Results in **Figures 24 and 25** showed that A375 ULA tumouroids responded to both vemurafenib and staurosporine (STS) treatment; their growth was inhibited by both drugs. These results are supported by evidence that A375 cell proliferation is inhibited by

vemurafenib, and that STS treatment induces apoptosis in A375 cells, decreasing their viability, thereby suggesting inhibition of proliferation[220,234].

To study DJ-1 more closely in 3D, DJ-1 was targeted with a DJ-1 inhibitor in A375 ULA tumouroids. STK793590 was used as the DJ-1 inhibitor and was tested alone and in combination with vemurafenib, based on previous findings. Results in **Figure 28** showed that STK793590 (50 µM) in combination with vemurafenib (1 µM) significantly decreased A375 cell proliferation compared to the DMSO control, however, there was no significant difference between vemurafenib (1 µM) alone and the combination with STK793590 (50 µM) on cell proliferation. These results were different to what was obtained in our corresponding 2D experiment, which showed that there was a significant difference between vemurafenib (1 µM) treatment on its own and STK793590 (50 µM) in combination with vemurafenib (1 µM). These results suggest that the combination loses its effect in 3D. This type of finding is not uncommon, as it has been reported that certain drugs can lose their efficacy when tested in a 3D model. For instance, the PI3K inhibitor, LY294002, showed good efficacy in a 2D melanoma model, yet when it was tested in 3D, it lost its activity[235,236]. Findings such as these confirm the importance of testing drugs both in 2D and 3D models. There was, however, a difference seen between vemurafenib (0.1 µM) alone and vemurafenib (0.1 µM) in combination with STK793590 (50 µM) in both the 2D model and 3D model.

The variable results obtained between the two models do raise questions as to whether DJ-1 is a good target for melanoma. It could be that STK793590 might not be targeting DJ-1 as it is a small molecule, meaning that it is more likely to be non-specific. STK793590 could be inhibiting cell proliferation and tumouroid growth via another mechanism instead. Moreover, the 50 µM concentration used was quite high, leading to potential significant toxicity. One limitation of this 3D experiment is that the same concentrations of STK793590 and vemurafenib were used as in the 2D experiment, which may not have been strong enough to have an effect in the 3D model. Tumouroids can exhibit more resistance to anticancer drugs compared to the same cancer cells grown in monolayers, most likely since it is harder for drugs to penetrate all parts of a tumouroid[237]. 3D cultures can also affect metabolism, gene expression and cell-cell communication all of which can have an impact on drug efficacy[238].

In addition to this experiment, the effects of STK793590 or vemurafenib treatment alone or in combination were also tested on the viability and cytotoxicity of A375 ULA tumouroids. Results in **Figure 30** indicated that tumouroids treated with vemurafenib alone (1 µM) or STK793590 (50 µM) in combination with vemurafenib (1 µM) had the most cell death occurring. Vemurafenib is known to induce apoptosis in A375 cells as reported by Pérez *at al* (2023)[239], so this finding is as expected, however, STK793590 most likely had no additional effect on A375 cell death. Limitations of this experiment included labelling issues and potential LIVE/DEAD quantification issues due to tumouroid images being

single focal plane images. Aside from both 3D experiments involving STK793590 and vemurafenib, it would be interesting to study DJ-1 knockdown in a 3D model as part of future work.

This project aimed to study the role of DJ-1 in 2D and 3D models of melanoma to elucidate whether DJ-1 could be a potential therapeutic target. The siRNA experiments allowed for a better understanding of DJ-1's role in melanoma cell proliferation and in Nrf2 signalling, however other potential DJ-1 roles should also be studied in the future. The localisation experiment provided a better understanding into DJ-1's role in cell migration and transcription, nevertheless the experiment was only carried out under normal conditions. Testing and optimising three 3D melanoma models revealed different strengths and limitations of each model which were considered prior to selecting the most suitable one for further DJ-1 experiments. Experiments involving STK793590 and vemurafenib both in 2D and 3D revealed contradicting results, questioning whether STK793590 is targeting the DJ-1 homodimer. Future experiments validating STK793590 binding to the critical Cys106 residue of DJ-1 and uptake into A375 cells via fluorescence tagging and confocal microscopy need to be conducted. It would also be beneficial to study DM10 (see **Section 1.3.5**) activity in A375 cells, as Chen *et al* (2021)[205] discovered that DM10 had higher anti-tumour activity compared to STK793590. Effects of STK793590 on deglycase activity of DJ-1 in A375 cells should also be investigated, since Tashiro *et al* (2018)[136] originally reported that the inhibitor targets this activity.

Overall, contradicting data as to whether DJ-1 is a good target for melanoma cancer, was obtained during this project. Regardless of this, more research into DJ-1's role in melanoma and validation of experiments is warranted, as based on the literature, DJ-1 is involved in the progression of other cancer types (see **Section 1.3.4**), so it could be hypothesised that the same mechanisms also happen in melanoma [**Figure 31**]. With the increasing incidence of melanoma and chemoresistance, new targets need to be investigated. This project found evidence that DJ-1 could be a potential target for melanoma treatment in 2D models, however, in 3D models this was questioned and requires further investigation. As a result, further studies are needed to explore the broader functions of DJ-1 in skin melanoma.
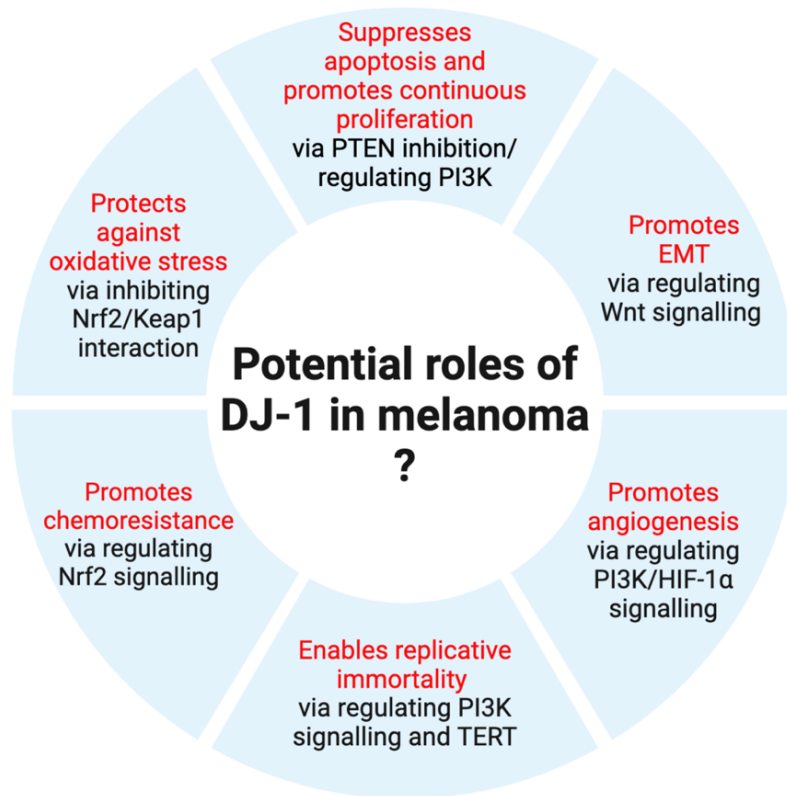
**Figure 31 – The potential roles of DJ-1 in melanoma.**

# 5. Appendix

## 5.1 Recipes and buffers

### 5.1.1 Media for cell culture

**Table 11 – Cell culture media supplementation**

| Type of media | Incomplete media | FBS | Penicillin/Streptomycin | L-Glutamine | DMSO |
|---|---|---|---|---|---|
| Complete RPMI | RPMI | 10% | 1% | 1% | N/A |
| Freezing media | N/A | 90% | N/A | N/A | 10% |
| Antibiotic free | RPMI | 10% | N/A | 1% | N/A |
| Serum free | RPMI | N/A | 1% | 1% | N/A |

### 5.1.2 Western blotting

**Table 12 – Western blot buffer compositions**

| Buffer or Reagent | Recipe |
|---|---|
| 1X MOPS running buffer | - 40 mL NuPage 20X MOPS SDS running buffer<br>- 760 mL deionised water |
| 10X Transfer buffer | - 24.26 g Tris Base<br>- 112.6 g Glycine<br>- 1 g SDS<br>- Top up to 1 L with deionised water |
| 1X Transfer buffer | - 100 mL 10x Transfer Buffer<br>- 700 mL deionised water<br>- 200 mL methanol |
| 20X TBST | - 48.4 g Tris Base<br>- 160 g NaCl<br>- 62 mL 5M HCl<br>- 20 mL Tween 20<br>- pH to 7.6 and top up to 1 L with deionised water |
| 1X TBST | - 50 mL 20X TBST<br>- 950 mL deionised water |
| Blocking solution (5% milk in TBST) | - 20 g skimmed milk powder<br>- 400 mL 1X TBST |
| 1X PBS | - 137 mM NaCl<br>- 2.7 mM KCl<br>- 8.2 mM $Na_2HPO_4$<br>- 1.47 mM $KH_2PO_4$ dissolved in 800 mL deionised water<br>- pH to 7.0 and top up to 1 L with deionised water |
| Ponceau S staining solution | - 2.5 mL glacial acetic acid dissolved in 40 mL deionised water<br>- 0.05 g Ponceau salt<br>- Top up to 50 mL with deionised water |
| 1X stripping solution | - 3 g glycine<br>- 0.2 g SDS<br>- 2 mL Tween 20 dissolved in 160 mL deionised water<br>- pH to 2.2 and top up to 200 mL with deionised water |

## 5.2 Results
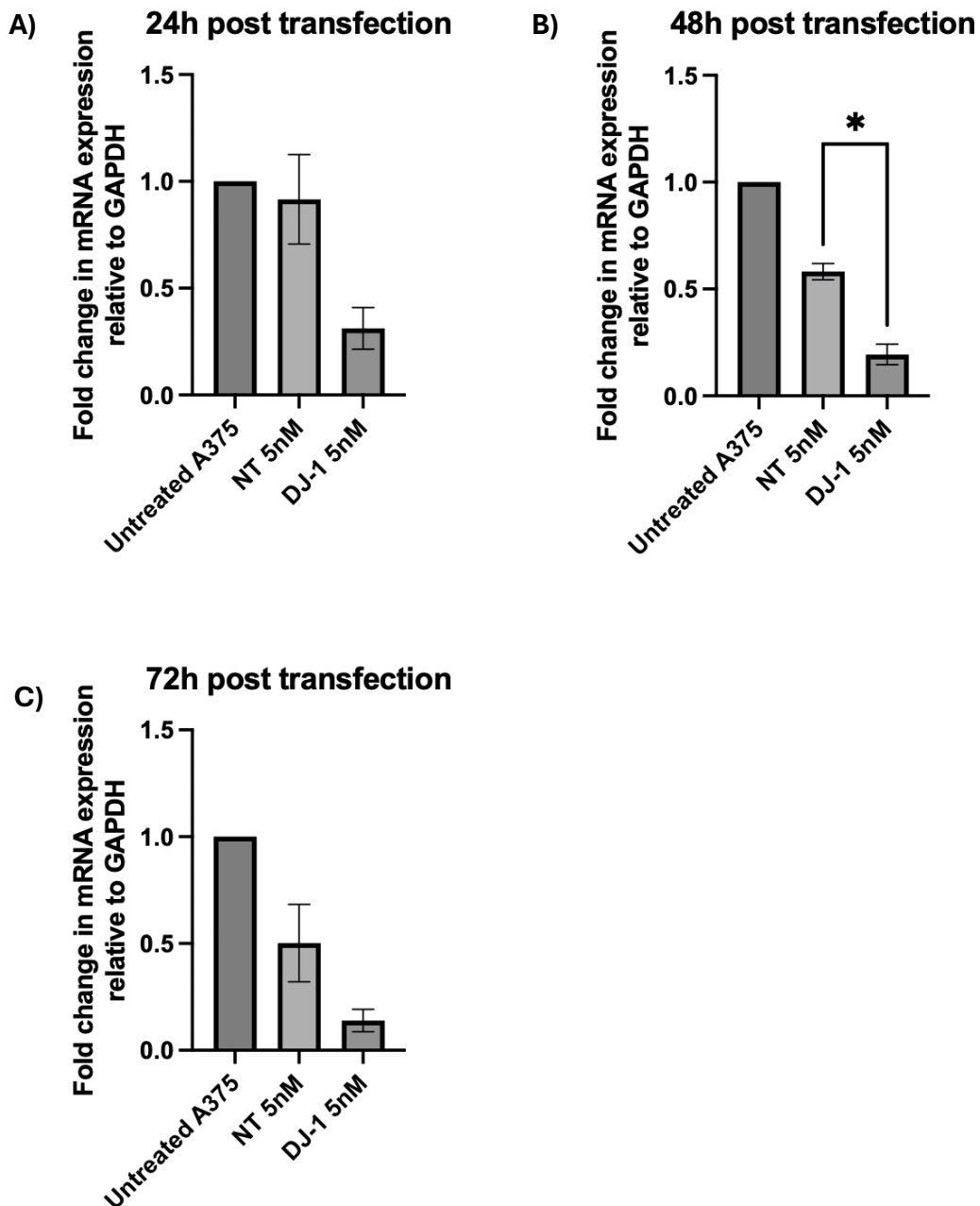


**Figure 32 – DJ-1 knockdown at 24, 48 or 72 h timepoints post 72 h transfection.** A375 cells (5x10$^4$ cells/mL) were seeded into a 96-well plate. After 24 h, 5 nM non-targeting (NT) or 5 nM DJ-1 targeting siRNA was added to the cells for 72 h. Following this, cells were left to incubate for an additional 24, 48 or 72 h. Next, total RNA was extracted and reverse transcribed and mRNA expression for DJ-1 measured by RT-qPCR. **A)** 24 h post transfection **B)** 48 h post transfection **C)** 72 h post transfection. Results are representative of two independent experiments (N=2) and statistical analysis was done by unpaired t-test (P*≤0.05, P**≤0.01, P***≤0.001, P****≤0.0001). Data is shown as mean ± SEM.
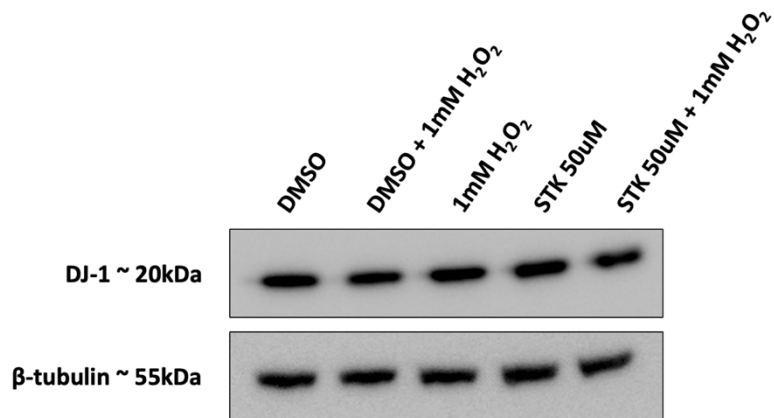
**Figure 33 – Effects of STK793590 on DJ-1 protein expression under normal and oxidative stress induced conditions.** DJ-1 protein expression was studied by western blot analysis using whole cell lysates made from $1 \times 10^6$ A375 cells. Before protein extraction, cells were treated with 50 μM STK793590 for 3 h before being treated with hydrogen peroxide ($H_2O_2$) for 4 h. β-tubulin was used as the loading control. Representative of 1 independent experiment (N=1).
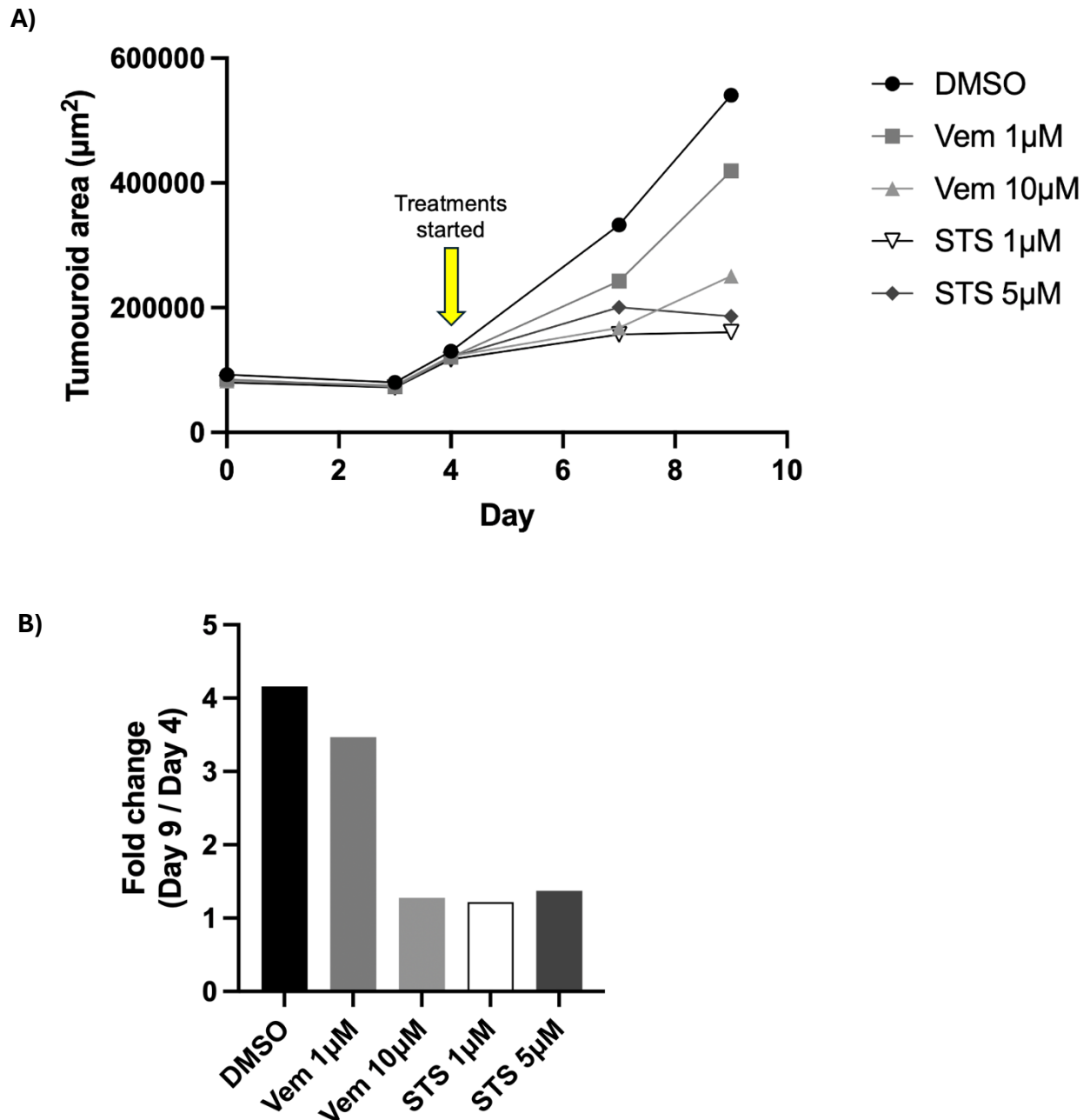
**Figure 34 – Effects of one-time vemurafenib and staurosporine (STS) treatment on A375 ULA tumouroid growth. A)** Average area of tumouroid growth over 9 days with one-time treatment of 1 µM or 5 µM staurosporine (STS) or 1 µM or 10 µM vemurafenib beginning on day 4 of culture. Tumouroid area was calculated using ImageJ analysis of Zeiss Observer white light microscopy images. Results are presented as mean area ($µm^2$) and representative of one independent experiment (N=1). **B)** Corresponding fold change results of A375 tumouroids in **A**. Results are representative of one independent experiment (N=1).
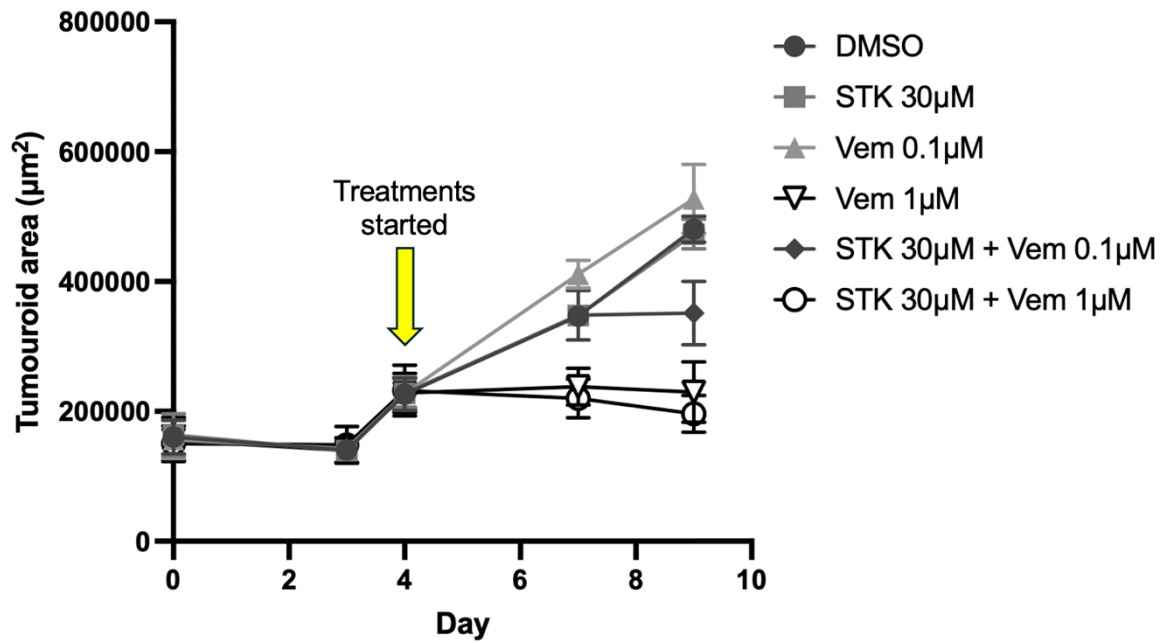
**Figure 35 – Effects of continuous vemurafenib treatment and 30 μM STK793590 in combination with vemurafenib treatment on A375 ULA tumouroid growth. A)** Average area of tumouroid growth over 9 days with continuous treatment of 0.1 μM or 1 μM vemurafenib or 30 μM STK793590 and combinations of these treatments beginning on day 4 of culture. Tumouroid area was calculated using ImageJ analysis of Zeiss Observer white light microscopy images. Results are presented as mean area (μm$^2$) and representative of three independent experiments (N=3). Statistical analysis was done by one-way ANOVA and post-hoc analysis via Tukey's test (P*≤0.05, P**≤0.01, P***≤0.001, P****≤0.0001). Data is shown as mean ± SEM. **B)** Corresponding fold change results of A375 tumouroids in **A**. Results are representative of

three independent experiments (N=3). Statistical analysis was done by one-way ANOVA and post-hoc analysis via Tukey's test (P*≤0.05, P**≤0.01, P***≤0.001, P****≤0.0001). Data is shown as mean ± SEM.
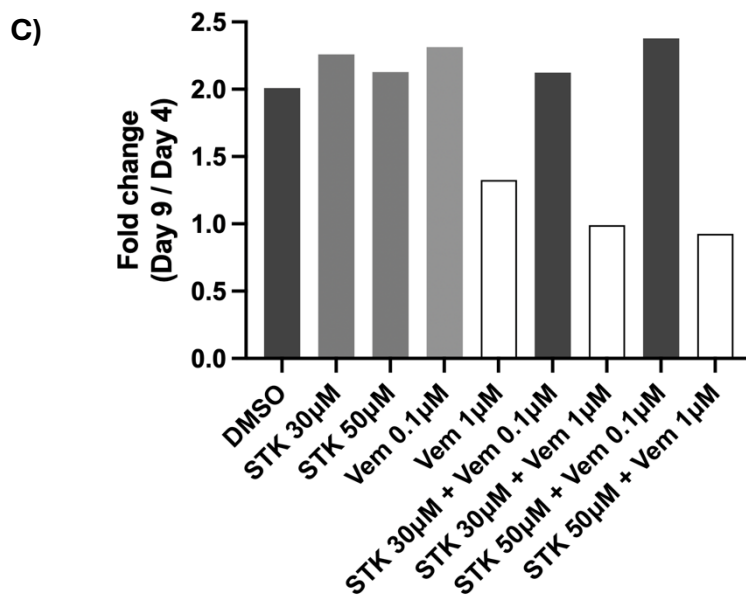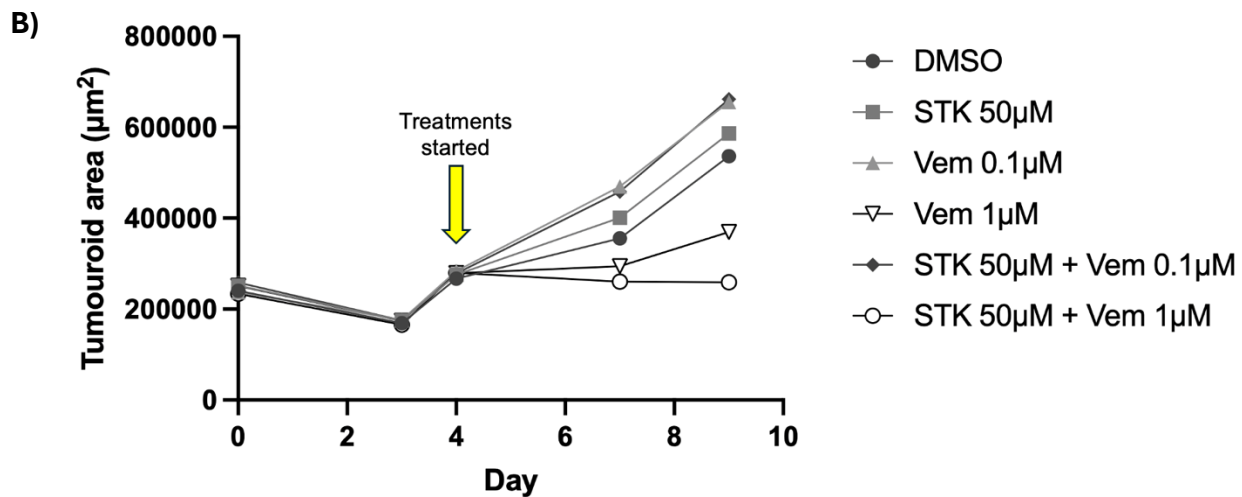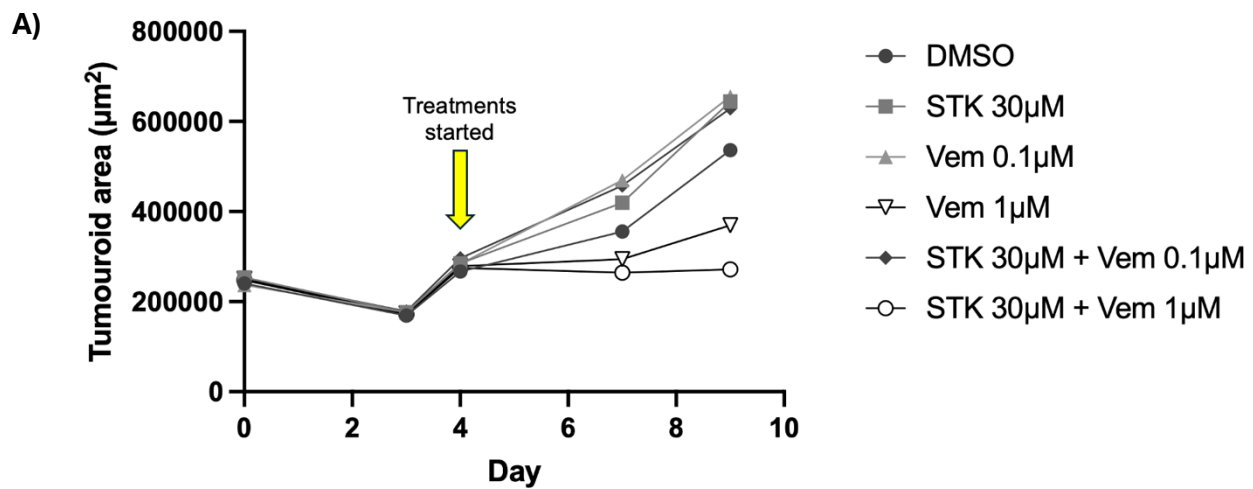
**Figure 36 – Effects of one-time vemurafenib treatment and STK793590 in combination with vemurafenib treatment on A375 ULA tumouroid growth. A)** Average area of tumouroid growth over 9 days with one-time treatment of 0.1 µM or 1 µM vemurafenib or 30 µM STK793590 and combinations of these treatments beginning on day 4 of culture. Tumouroid area was calculated using ImageJ analysis of Zeiss Observer white light microscopy images. Results are presented as mean area (µm$^2$) and representative of one independent experiment (N=1). **B)** Average area of tumouroid growth over 9 days with one-time treatment of 0.1 µM or 1 µM vemurafenib or 50 µM STK793590 and combinations of these treatments beginning on day 4 of culture. Tumouroid area was calculated using ImageJ analysis of Zeiss Observer white light microscopy images. Results are presented as mean area (µm$^2$) and representative of one independent experiment (N=1). **C)** Corresponding fold change results of A375 tumouroids in **A and B**. Results are representative of one independent experiment (N=1).
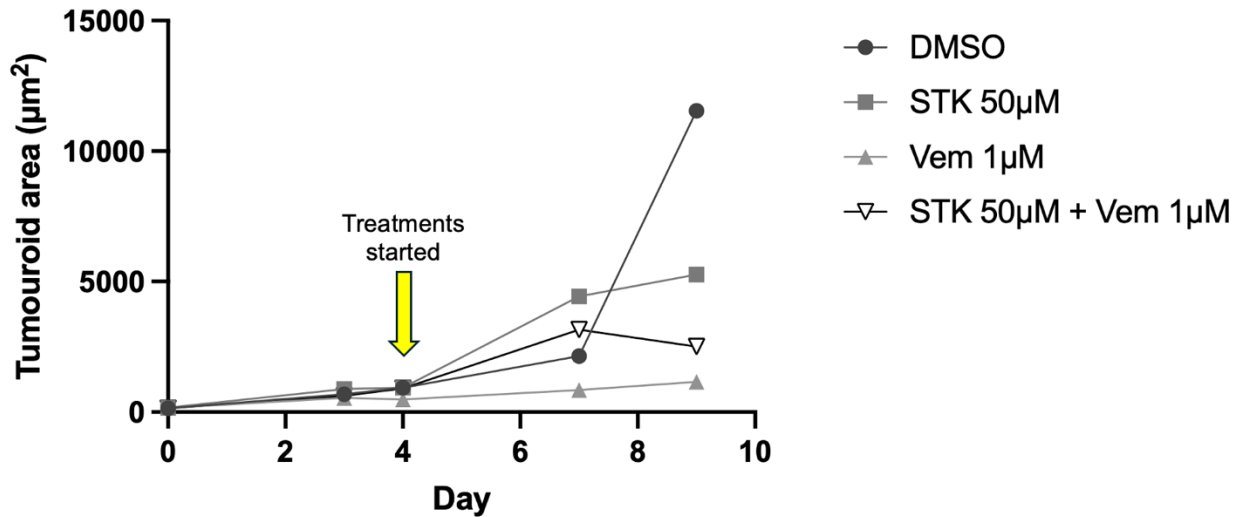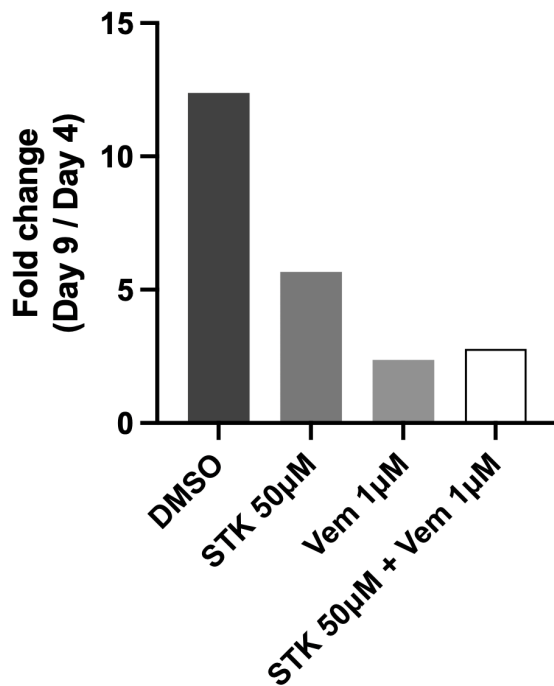
**Figure 37 – Effects of vemurafenib and STK793590 in combination with vemurafenib on A375 Matrigel Matrix tumouroid growth.** A375 cells were seeded at a density of $0.1 \times 10^4$ cells/well. **A)** Average area of tumouroid growth over 9 days with continuous treatment of 1 μM vemurafenib or 50 μM STK793590 and the combination of these treatments beginning on day 4 of culture. Average tumouroid area was calculated using ImageJ analysis of Zeiss Observer white light microscopy images. Results are presented as mean area ($\mu m^2$) and representative of one independent experiments (N=1). **B)** Corresponding fold change results of A375 tumouroids in **A**. Results are representative of one independent experiments (N=1).
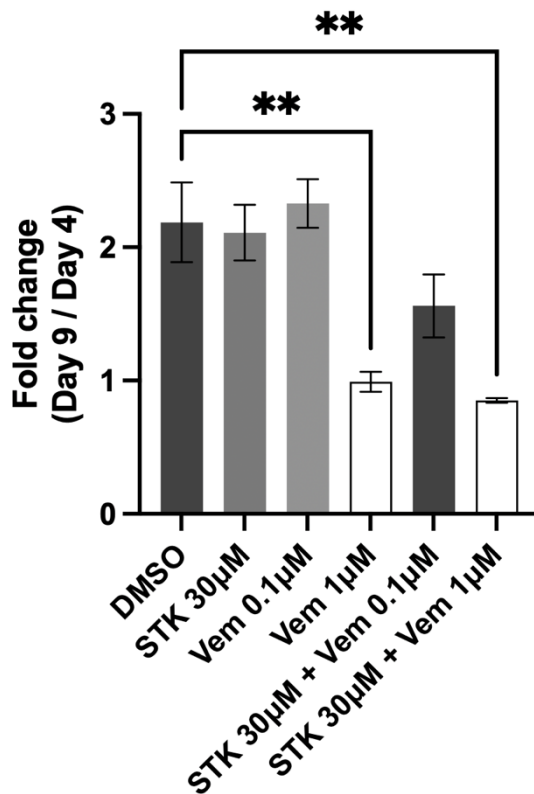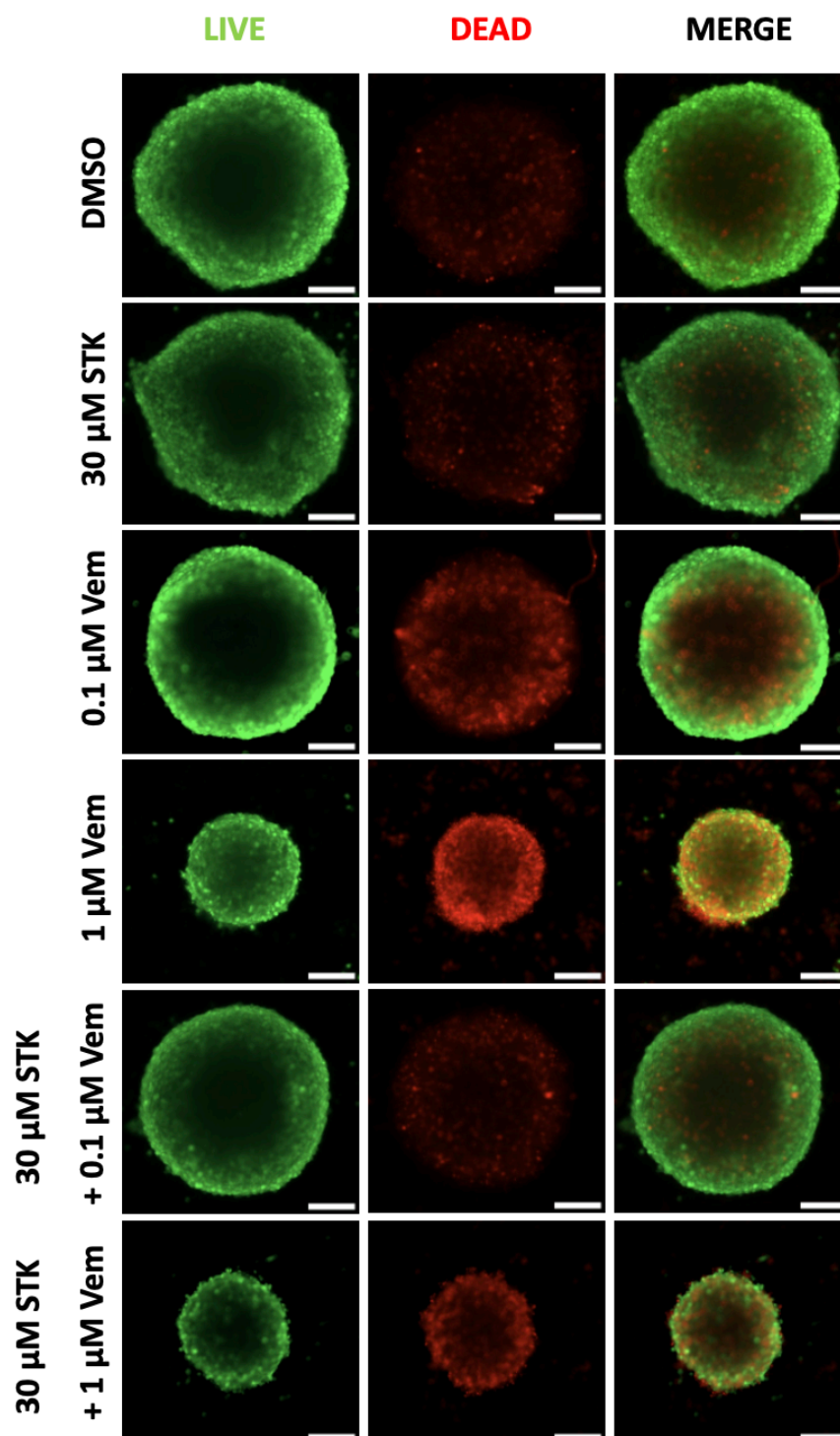
**Figure 38 – Effects of 30 µM STK793590 in combination with vemurafenib on A375 ULA tumouroid viability and cytotoxicity.** Representative images of tumouroids labelled with fluorescent LIVE/DEAD® viability/cytotoxicity dye following continuous treatments of vemurafenib (0.1 or 1 µM) and STK793590 (30 µM) on their own or in combination. Tumouroids were cultured for 3 days before being treated with drugs on day 4. They were then left to incubate up to day 9 and were treated every day. On day 9, the LIVE/DEAD® viability/cytotoxicity dye was incubated with the tumouroids for 45 mins and tumouroid

viability and cytotoxicity was visualised via fluorescence microscopy (N=1). Images were analysed in ImageJ. Scale bar 100 µm.
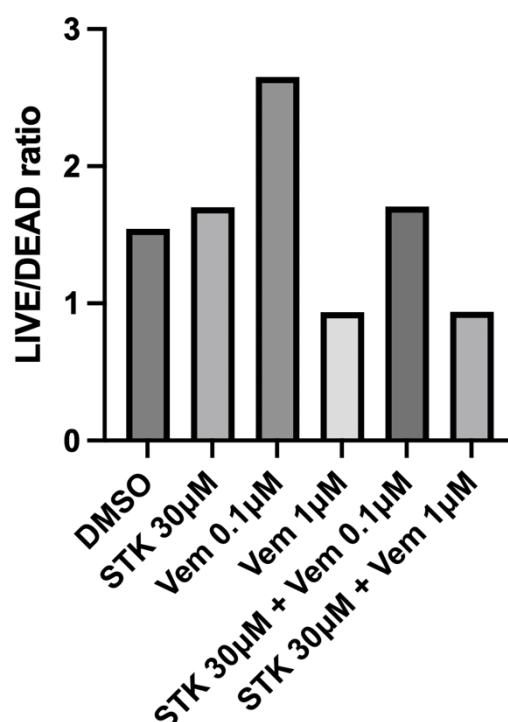


**Figure 39 – LIVE/DEAD ratio of 30 µM STK793590 in combination with vemurafenib on A375 ULA tumouroids.** Continuous treatments of vemurafenib (0.1 or 1 µM) and STK793590 (30 µM) on their own or in combination. Tumouroids were cultured for 3 days before being treated with drugs on day 4. They were then left to incubate up to day 9 and were treated every day. On day 9, the LIVE/DEAD® viability/cytotoxicity dye was incubated with the tumouroids for 45 mins and tumouroid viability and cytotoxicity was visualised via fluorescence microscopy. LIVE/DEAD ratio was calculated using ImageJ. Results are representative of one independent experiment (N=1).

# 6. References

1       Smittenaar, C. R., Petersen, K. A., Stewart, K. & Moitt, N. (2016). Cancer incidence and mortality projections in the UK until 2035. *British Journal of Cancer*, 115, 1147-1155, doi:10.1038/bjc.2016.304

2       Cancer Research UK. (2015). Cancer Statistics for the UK. *Cancer Research UK; CRUK*. <https://www.cancerresearchuk.org/health-professional/cancer-statistics-for-the-uk#heading-Zero> [Date accessed: 14/11/24]

3       Bray, F., Laversanne, M., Sung, H., Ferlay, J., Siegel, R. L., Soerjomataram, I., & Jemal, A. (2024). Global Cancer Statistics 2022: GLOBOCAN Estimates of Incidence and Mortality Worldwide for 36 Cancers in 185 Countries. *CA: A Cancer Journal for Clinicians, 74*(3), 229–263, doi: 10.3322/caac.21834

4       Hanahan, D., & Weinberg, R. A. (2000). The Hallmarks of Cancer. *Cell, 100*(1), 57–70, doi: 10.1016/s0092-8674(00)81683-9

5       Hanahan, D., & Weinberg, Robert A. (2011). Hallmarks of cancer: the next Generation. *Cell, 144(*5), 646–674, doi: 10.1016/j.cell.2011.02.013

6       Hanahan, D. (2022). Hallmarks of Cancer: New Dimensions. *Cancer Discovery, 12*(1), 31–46, doi: 10.1158/2159-8290.cd-21-1059

7       O'Connor, C. (2008). Cell Division: Stages of Mitosis. *Nature Education 1*(1):188. <https://www.nature.com/scitable/topicpage/mitosis-and-cell-division-205/> [Date accessed: 14/11/24]

8       Rehman, I., Basit, H., Malik, A., & Simpson, B. (2023). Genetics, Mitosis. PubMed; *StatPearls Publishing*. <https://www.ncbi.nlm.nih.gov/books/NBK482449/> [Date accessed: 02/01/25]

9       Matthews, H. K., Bertoli, C., & de Bruin, R. A. M. (2021). Cell cycle control in cancer. *Nature Reviews Molecular Cell Biology*, *23*, doi: 10.1038/s41580-021-00404-3

10      Liggett, W. H., & Sidransky, D. (1998). Role of the p16 tumor suppressor gene in cancer. *Journal of Clinical Oncology: Official Journal of the American Society of Clinical Oncology, 16*(3), 1197–1206, doi: 10.1200/JCO.1998.16.3.1197

11      Romagosa, C., Simonetti, S., López-Vicente, L., Mazo, A., Lleonart, M. E., Castellvi, J., & Ramon y Cajal, S. (2011). p16Ink4a overexpression in cancer: a tumor suppressor gene associated with senescence and high-grade tumors. *Oncogene*, *30*(18), 2087–2097, doi: 10.1038/onc.2010.614

12      Serra, S., & Chetty, R. (2018). p16. *Journal of Clinical Pathology*, *71*(10), 853–858, doi: 10.1136/jclinpath-2018-205216

13      Pisano, M., Arru, C., Serra, M., Galleri, G., Sanna, D., Garribba, E., Palmieri, G., & Rozzo, C. (2019). Antiproliferative activity of vanadium compounds: effects on the major malignant melanoma molecular pathways. *Metallomics*, *11*(10), 1687–1699, doi: 10.1039/c9mt00174c

14      Cilluffo, D., Barra, V., & Di Leonardo, A. (2020). P14ARF: The Absence that Makes the Difference. *Genes, 11*(7), 824, doi: 10.3390/genes11070824

15    Wang, H., Guo, M., Wei, H., & Chen, Y. (2023). Targeting p53 pathways: mechanisms, structures, and advances in therapy. *Signal Transduction and Targeted Therapy*, *8*(1), 1–35, doi: 10.1038/s41392-023-01347-1

16    Dasari, S., & Tchounwou, P. B. (2014). Cisplatin in Cancer therapy: Molecular Mechanisms of Action. *European Journal of Pharmacology*, *740*(1), 364–378, doi: 10.1016/j.ejphar.2014.07.025

17    Karimian, A., Ahmadi, Y., & Yousefi, B. (2016). Multiple functions of p21 in cell cycle, apoptosis and transcriptional regulation after DNA damage. *DNA Repair*, *42*, 63–71, doi: 10.1016/j.dnarep.2016.04.008

18    Dimri, G. P., Nakanishi, M., Desprez, P.-Y., Smith, J. R., & Campisi, J. (1996). Inhibition of E2F Activity by the Cyclin-Dependent Protein Kinase Inhibitor p21 in Cells Expressing or Lacking a Functional Retinoblastoma Protein. *Molecular and Cellular Biology*, *16*(6), 2987–2997, doi: 10.1128/mcb.16.6.2987

19    M.R. Sargen, Merrill, S. L., Chu, E. Y., & Nathanson, K. L. (2016). *CDKN2A* mutations with p14 loss predisposing to multiple nerve sheath tumours, melanoma, dysplastic naevi and internal malignancies: a case series and review of the literature. *British Journal of Dermatology*, *175*(4), 785–789, doi: 10.1111/bjd.14485

20    Aubrey, B. J., Kelly, G. L., Janic, A., Herold, M. J., & Strasser, A. (2017). How does p53 induce apoptosis and how does this relate to p53-mediated tumour suppression? *Cell Death & Differentiation*, *25*(1), 104–113, doi: 10.1038/cdd.2017.169

21    Zhang, X.-P., Liu, F., & Wang, W. (2010). Coordination between cell cycle progression and cell fate decision by the p53 and E2F1 pathways in response to DNA damage. *The Journal of Biological Chemistry*, *285*(41), 31571–31580, doi: 10.1074/jbc.M110.134650

22    Chen, X., Zhang, T., Su, W., Dou, Z., Zhao, D., Jin, X., Lei, H., Wang, J., Xie, X., Cheng, B., Li, Q., Zhang, H., & Di, C. (2022). Mutant p53 in cancer: from molecular mechanism to therapeutic modulation. *Cell Death & Disease*, *13*(11), doi: 10.1038/s41419-022-05408-1

23    Kim, S. K., & Cho, S. W. (2022). The evasion mechanisms of cancer immunity and drug intervention in the tumor microenvironment. *Frontiers in Pharmacology*, *13*(868695), doi: 10.3389/fphar.2022.868695

24    Mravec, B. (2024). Avoiding Immune Destruction. In: Neurobiology of Cancer. Springer, Cham, doi: 10.1007/978-3-031-68590-3_12

25    Nam, A. S., Chaligne, R., & Landau, D. A. (2021). Integrating genetic and non-genetic determinants of cancer evolution by single-cell multi-omics. *Nature Reviews Genetics*, *22*(1), 3–18, doi: 10.1038/s41576-020-0265-5

26    Darwiche, N. (2020). Epigenetic mechanisms and the hallmarks of cancer: an intimate affair. *American Journal of Cancer Research*, *10*(7), 1954–1978. <https://pubmed.ncbi.nlm.nih.gov/32774995/> [Date accessed: 03/01/25]

27 Xiao, S., Qin, D., Hou, X., Tian, L., Yu, Y., Zhang, R., Lyu, H., Guo, D., Chen, X.-Z., Zhou, C., & Tang, J. (2023). Cellular senescence: a double-edged sword in cancer therapy. *Frontiers in Oncology*, *13*, doi: 10.3389/fonc.2023.1189015

28 Faget, D. V., Ren, Q., & Stewart, S. A. (2019). Unmasking senescence: context-dependent effects of SASP in cancer. *Nature Reviews Cancer*, *19*(8), 439–453, doi: 10.1038/s41568-019-0156-2

29 Lee, S., & Schmitt, C. A. (2019). The dynamic nature of senescence in cancer. *Nature Cell Biology*, *21*(1), 94–101, doi: 10.1038/s41556-018-0249-2

30 Cancer Research UK. (2023). What is chemotherapy? | Cancer in general | Cancer Research UK. <https://www.cancerresearchuk.org/about-cancer/treatment/chemotherapy/what-chemotherapy-is> [Date accessed: 03/01/25]

31 Humphrey P. Rang, M. M. D., James M. Ritter, Rod J. Flower, Graeme Henderson, Yoon K. Loke and David MacEwan. *Rang and Dale's Pharmacology*. 9 edn, (London Churchill Livingstone Elsevier, 2020).

32 DeVita, V. T., & Chu, E. (2008). A History of Cancer Chemotherapy. *Cancer Research*, *68*(21), 8643–8653, doi: 10.1158/0008-5472.can-07-6611

33 Smith, S. L. (2017). War! What is it good for? Mustard gas medicine. *Canadian Medical Association Journal*, *189*(8), doi: 10.1503/cmaj.161032

34 Macmillan Cancer Support. (2022). Side Effects of Chemotherapy. *Macmillan Cancer Support*. <https://www.macmillan.org.uk/cancer-information-and-support/treatment/types-of-treatment/chemotherapy/side-effects-of-chemotherapy> [Date accessed: 10/01/25]

35 Krzyszczyk, P., Acevedo, A., Davidoff, E. J., Timmins, L. M., Marrero-Berrios, I., Patel, M., White, C., Lowe, C., Sherba, J. J., Hartmanshenn, C., O'Neill, K. M., Balter, M. L., Fritz, Z. R., Androulakis, I. P., Schloss, R. S., & Yarmush, M. L. (2018). The growing role of precision and personalized medicine for cancer treatment. *Technology*, 79–100, doi: 10.1142/s2339547818300020

36 Riley, R. S., June, C. H., Langer, R., & Mitchell, M. J. (2019). Delivery technologies for cancer immunotherapy. *Nature Reviews. Drug Discovery*, *18*(3), 175–196, doi: 10.1038/s41573-018-0006-z

37 Cheng, X. (2024). A Comprehensive Review of HER2 in Cancer Biology and Therapeutics. *Genes*, *15*(7), 903–903, doi: 10.3390/genes15070903

38 Slamon, D., Clark, G., Wong, S., Levin, W., Ullrich, A., & McGuire, W. (1987). Human breast cancer: correlation of relapse and survival with amplification of the HER-2/neu oncogene. *Science*, *235*(4785), 177–182, doi: 10.1126/science.3798106

39 Swain, S. M., Shastry, M., & Hamilton, E. (2022). Targeting HER2-positive breast cancer: advances and future directions. *Nature Reviews Drug Discovery*, *22*(2), 1–26.

40    Han, Y., Liu, D., & Li, L. (2020). PD-1/PD-L1 pathway: current researches in cancer. *American Journal of Cancer Research*, *10*(3), 727. <https://pmc.ncbi.nlm.nih.gov/articles/PMC7136921/> [Date accessed: 10/01/25]

41    Macmillan Cancer Support (2023). *Nivolumab (Opdivo®)*. *Macmillan Cancer Support*. <https://www.macmillan.org.uk/cancer-information-and-support/treatments-and-drugs/nivolumab> [Date accessed: 10/01/25]

42    Hong, M., Clubb, J. D., & Chen, Y. Y. (2020). Engineering CAR-T Cells for Next-Generation Cancer Therapy. *Cancer Cell*, *38*(4), 473–488, doi: 10.1016/j.ccell.2020.07.005

43    Alnefaie, A., Albogami, S., Asiri, Y., Ahmad, T., Alotaibi, S. S., Al-Sanea, M. M., & Althobaiti, H. (2022). Chimeric Antigen Receptor T-Cells: An Overview of Concepts, Applications, Limitations, and Proposed Solutions. *Frontiers in Bioengineering and Biotechnology*, *10*, doi: 10.3389/fbioe.2022.797440

44    Rose, S. (2017). First-Ever CAR T-cell Therapy Approved in U.S. *Cancer Discovery*, *7*(10), doi: 10.1158/2159-8290.cd-nb2017-126

45    Novartis Pharmaceuticals. (2024). A Phase II, Single Arm, Multicenter Trial to Determine the Efficacy and Safety of CTL019 in Pediatric Patients With Relapsed and Refractory B-cell Acute Lymphoblastic Leukemia. *Clinicaltrials.gov*. <https://clinicaltrials.gov/study/NCT02435849> [Date accessed: 11/01/25]

46    Sterner, R. C., & Sterner, R. M. (2021). CAR-T Cell therapy: Current Limitations and Potential Strategies. *Blood Cancer Journal*, *11*(4), 1–11. <https://www.nature.com/articles/s41408-021-00459-7> [Date accessed: 11/01/25]

47    Saxena, M., van der Burg, S. H., Melief, C. J. M., & Bhardwaj, N. (2021). Therapeutic cancer vaccines. *Nature Reviews Cancer*, *21*(6), 360–378. <https://doi.org/10.1038/s41568-021-00346-0> [Date accessed: 11/01/25]

48    Fan, T., Zhang, M., Yang, J., Zhu, Z., Cao, W., & Dong, C. (2023). Therapeutic cancer vaccines: advancements, challenges, and prospects. *Signal Transduction and Targeted Therapy*, *8*(1), doi: 10.1038/s41392-023-01674-3

49    Ishikawa, H., Imano, M., Shiraishi, O., Yasuda, A., Peng, Y.-F., Shinkai, M., Yasuda, T., Imamoto, H., & Shiozaki, H. (2013). Phase I clinical trial of vaccination with LY6K-derived peptide in patients with advanced gastric cancer. *Gastric Cancer*, *17*(1), 173–180, doi: 10.1007/s10120-013-0258-6

50    Lee, W.-L., Cheng, M.-H., Chao, H.-T., & Wang, P.-H. (2008). The Role of Selective Estrogen Receptor Modulators on Breast Cancer: From Tamoxifen to Raloxifene. *Taiwanese Journal of Obstetrics and Gynecology*, *47*(1), 24–31, doi: 10.1016/S1028-4559(08)60051-0

51     Cook, T., & Sheridan, W. P. (2000). Development of GnRH Antagonists for Prostate Cancer: New Approaches to Treatment. *The Oncologist*, *5*(2), 162–168, doi: 10.1634/theoncologist.5-2-162

52     Anand, U., Dey, A., Chandel, A. K. S., Sanyal, R., Mishra, A., Pandey, D. K., De Falco, V., Upadhyay, A., Kandimalla, R., Chaudhary, A., Dhanjal, J. K., Dewanjee, S., Vallamkondu, J., & Pérez de la Lastra, J. M. (2022). Cancer chemotherapy and beyond: Current status, drug candidates, associated risks and progress in targeted therapeutics. *Genes & Diseases*, *10*(4), 1367–1401, doi: 10.1016/j.gendis.2022.02.007

53     Long, G. V., Swetter, S. M., Menzies, A. M., Gershenwald, J. E., & Scolyer, R. A. (2023). Cutaneous melanoma. *The Lancet*, *402*(10400), 485–502, doi: 10.1016/s0140-6736(23)00821-8

54     Davis, L. E., Shalin, S. C., & Tackett, A. J. (2019). Current state of melanoma diagnosis and treatment. *Cancer Biology & Therapy*, *20*(11), 1366–1379, doi: 10.1080/15384047.2019.1640032

55     National Cancer Institute. (2023). Melanoma Treatment. *National Cancer Institute; Cancer.gov*. <https://www.cancer.gov/types/skin/patient/melanoma-treatment-pdq> [Date accessed: 22/01/25]

56     Cancer Research UK. (2020). What is melanoma? | Melanoma skin cancer | Cancer Research UK. <https://www.cancerresearchuk.org/about-cancer/melanoma/about> [Date accessed: 12/01/25]

57     Leonardi, G., Falzone, L., Salemi, R., Zanghì, A., Spandidos, D., Mccubrey, J., Candido, S., & Libra, M. (2018). Cutaneous melanoma: From pathogenesis to therapy (Review). *International Journal of Oncology*, *52*(4), doi: 10.3892/ijo.2018.4287

58     Cancer Research UK. (2018). Melanoma skin cancer statistics. *Cancer Research UK; CRUK*. <https://www.cancerresearchuk.org/health-professional/cancer-statistics/statistics-by-cancer-type/melanoma-skin-cancer#heading-One> [Date accessed: 12/01/25]

59     Motwani, J., & Eccles, M. R. (2021). Genetic and Genomic Pathways of Melanoma Development, Invasion and Metastasis. *Genes*, *12*(10), 1543, doi: 10.3390/genes12101543

60     Shain, A. H., & Bastian, B. C. (2016). From melanocytes to melanomas. *Nature Reviews Cancer*, *16*(6), 345–358, doi: 10.1038/nrc.2016.37

61     Strashilov, S., & Yordanov, A. (2021). Aetiology and Pathogenesis of Cutaneous Melanoma: Current Concepts and Advances. *International Journal of Molecular Sciences*, *22*(12), 6395, doi: 10.3390/ijms22126395

62     Naoi, M., Maruyama, W., & Riederer, P. (2010). Melanin. *Encyclopedia of Movement Disorders*, 169–171, doi: 10.1016/b978-0-12-374105-9.00480-9

63     Lin, J. Y., & Fisher, D. E. (2007). Melanocyte biology and skin pigmentation. *Nature*, *445*(7130), 843–850, doi: 10.1038/nature05660

64  Mitra, D., Luo, X., Morgan, A., Wang, J., Hoang, M. P., Lo, J., Guerrero, C. R., Lennerz, J. K., Mihm, M. C., Wargo, J. A., Robinson, K. C., Devi, S. P., Vanover, J. C., D'Orazio, J. A., McMahon, M., Bosenberg, M. W., Haigis, K. M., Haber, D. A., Wang, Y., & Fisher, D. E. (2012). An ultraviolet-radiation-independent pathway to melanoma carcinogenesis in the red hair/fair skin background. *Nature*, *491*(7424), 449–453, doi: 10.1038/nature11624

65  Más, J. S., Sánchez, C. O., Ghanem, G., Haycock, J., Teruel, J. A. L., García-Borrón, J. C., & Jiménez-Cervantes, C. (2002). Loss-of-function variants of the human melanocortin-1 receptor gene in melanoma cells define structural determinants of receptor function. *European Journal of Biochemistry*, *269*(24), 6133–6141, doi: 10.1046/j.1432-1033.2002.03329.x

66  Maranduca, M., Branisteanu, D., Serban, D., Branisteanu, D., Stoleriu, G., Manolache, N., & Serban, I. (2019). Synthesis and physiological implications of melanic pigments (Review). *Oncology Letters*, *17*(5), doi: 10.3892/ol.2019.10071

67  Holcomb, G., Murphy, P., Ostlie, D.J. *Ashcraft's Pediatric Surgery*. 5edn, (Saunders Elsevier, 2010).

68  Piipponen, M., Li, D., & Landén, N. X. (2020). The Immune Functions of Keratinocytes in Skin Wound Healing. *International Journal of Molecular Sciences*, *21*(22), doi: 10.3390/ijms21228790

69  Benito-Martínez, S., Salavessa, L., Raposo, G., Marks, M. S., & Delevoye, C. (2021). Melanin Transfer and Fate within Keratinocytes in Human Skin Pigmentation. *Integrative and Comparative Biology*, *61*(4), 1546–1555, doi: 10.1093/icb/icab094

70  Li, X., Mao, W., Chen, J., Goding, C. R., Cui, R., Xu, Z.-X., & Miao, X. (2021). The protective role of MC1R in chromosome stability and centromeric integrity in melanocytes. *Cell Death Discovery*, *7*, 111, doi: 10.1038/s41420-021-00499-9

71  Dong, L., Wen, J., Pier, E., Zhang, X., Zhang, B., Dong, F., Ziegler, N., Mysz, M., Armenta, R., & Cui, R. (2010). Melanocyte-Stimulating Hormone Directly Enhances UV-Induced DNA Repair in Keratinocytes by a Xeroderma Pigmentosum Group A–Dependent Mechanism. *Cancer Research*, *70*(9), 3547–3556, doi: 10.1158/0008-5472.can-09-4596

72  Bertolotto, C. (2013). Melanoma: From Melanocyte to Genetic Alterations and Clinical Options. *Scientifica*, *2013*, 1–22, doi: 10.1155/2013/635203

73  Randic, T., Kozar, I., Margue, C., Utikal, J., & Kreis, S. (2021). NRAS mutant melanoma: Towards better therapies. *Cancer Treatment Reviews*, *99*, doi: 10.1016/j.ctrv.2021.102238

74  Kunz, M., & Vera, J. (2019). Modelling of Protein Kinase Signaling Pathways in Melanoma and Other Cancers. *Cancers*, *11*(4), 465, doi: 10.3390/cancers11040465

75    Yakovian, O., Sajman, J., Arafeh, R., Neve-Oz, Y., Alon, M., Samuels, Y., & Sherman, E. (2021). MEK Inhibition Reverses Aberrant Signaling in Melanoma Cells through Reorganization of NRas and BRAF in Self Nanoclusters. *Cancer Research*, *81*(5), 1279–1292, doi: 10.1158/0008-5472.CAN-20-1205

76    Li, S., Balmain, A., & Counter, C. M. (2018). A model for RAS mutation patterns in cancers: finding the sweet spot. *Nature Reviews. Cancer*, *18*(12), 767–777, doi: 10.1038/s41568-018-0076-6

77    Johnson, D. B., & Puzanov, I. (2015). Treatment of NRAS-Mutant Melanoma. *Current Treatment Options in Oncology*, *16*(4), 15, doi: 10.1007/s11864-015-0330-z

78    Zhao, J., Galvez, C., Kathryn Eby Beckermann, Johnson, D. B., & Sosman, J. A. (2021). Novel insights into the pathogenesis and treatment of NRAS mutant melanoma. *Expert Review of Precision Medicine and Drug Development*, 6(4), 281–294, doi: 10.1080/23808993.2021.1938545

79    Ascierto, P. A., Kirkwood, J. M., Grob, J.-J., Simeone, E., Grimaldi, A. M., Maio, M., Palmieri, G., Testori, A., Marincola, F. M., & Mozzillo, N. (2012). The role of BRAF V600 mutation in melanoma. *Journal of Translational Medicine*, *10*(1), doi: 10.1186/1479-5876-10-85

80    Gonzalez, D., Fearfield, L., Nathan, P., Tanière, P., Wallace, A., Brown, E., Harwood, C., Marsden, J., & Whittaker, S. (2013). BRAF mutation testing algorithm for vemurafenib treatment in melanoma: recommendations from an expert panel. *British Journal of Dermatology*, *168*(4), 700–707, doi: 10.1111/bjd.12248

81    Śmiech, M., Leszczyński, P., Kono, H., Wardell, C., & Taniguchi, H. (2020). Emerging BRAF Mutations in Cancer Progression and Their Possible Effects on Transcriptional Networks. *Genes*, *11*(11), 1342, doi: 10.3390/genes11111342

82    Ince, F. A., Shariev, A., & Dixon, K. (2022). PTEN as a target in melanoma. *Journal of Clinical Pathology*, *75*(9), 581–584, doi: 10.1136/jclinpath-2021-208008

83    Wang, L., Kim, K. B., Kashani-Sabet, M., Dighe, P. R., & Aboosaiedi, A. (2023). Outcomes of patients with advanced NF1-mutant melanoma treated with MEK inhibitors. *Journal of Clinical Oncology*, *41*(16_suppl), e21513–e21513, doi: 10.1200/jco.2023.41.16_suppl.e21513

84    Davis, E. J., Johnson, D. B., Sosman, J. A., & Chandra, S. (2018). Melanoma: What do all the mutations mean? *Cancer*, *124*(17), 3490–3499, doi: 10.1002/cncr.31345

85    Pham, D. (Daniel) M., Guhan, S., & Tsao, H. (2020). KIT and Melanoma: Biological Insights and Clinical Implications. *Yonsei Medical Journal*, *61*(7), 562–571, doi: 10.3349/ymj.2020.61.7.562

86    Chandra, P. K. (2023). KIT Genetic Mutation in a Melanoma Patient. *Personalized Medicine in Oncology*.

<https://www.personalizedmedonc.com/articles/514:kit-genetic-mutation-in-a-melanoma-patient> [Date accessed: 18/01/25]

87   Cronin, J. C., Wunderlich, J., Loftus, S. K., Prickett, T. D., Wei, X., Ridd, K., Vemula, S., Burrell, A. S., Agrawal, N. S., Lin, J. C., Banister, C. E., Buckhaults, P., Rosenberg, S. A., Bastian, B. C., Pavan, W. J., & Samuels, Y. (2009). Frequent Mutations in the MITF Pathway in Melanoma. *Pigment Cell & Melanoma Research*, *22*(4), 435–444, doi: 10.1111/j.1755-148X.2009.00578.x

88   Toussi, A., Mans, N., Welborn, J., & Kiuru, M. (2020). Germline mutations predisposing to melanoma. *Journal of Cutaneous Pathology*, *47*(7), 606–616, doi: 10.1111/cup.13689

89   Guo, Y., Chen, Y., Zhang, L., Ma, L., Jiang, K., Yao, G., & Zhu, L. (2022). TERT Promoter Mutations and Telomerase in Melanoma. *Journal of Oncology*, doi: 10.1155/2022/6300329

90   Turner, K., Vasu, V., & Griffin, D. (2019). Telomere Biology and Human Phenotype. *Cells*, *8*(1), 73, doi: 10.3390/cells8010073

91   Gajos-Michniewicz, A., & Czyz, M. (2020). WNT Signaling in Melanoma. *International Journal of Molecular Sciences*, *21*(14), 4852. https://doi.org/10.3390/ijms21144852

92   Liu, J., Xiao, Q., Xiao, J., Niu, C., Li, Y., Zhang, X., Zhou, Z., Shu, G., & Yin, G. (2022). Wnt/β-catenin Signalling: Function, Biological mechanisms, and Therapeutic Opportunities. *Signal Transduction and Targeted Therapy*, *7*(3), 3, doi: 10.1038/s41392-021-00762-6

93   Yang, A. S., & Chapman, P. B. (2009). The History and Future of Chemotherapy for Melanoma. *Hematology/Oncology Clinics of North America*, *23*(3), 583–597, doi: 10.1016/j.hoc.2009.03.006

94   Reid, J. M., Kuffel, M. J., Miller, J. K., Rios, R., & Ames, M. M. (1999). Metabolic activation of dacarbazine by human cytochromes P450: the role of CYP1A1, CYP1A2, and CYP2E1. *Clinical Cancer Research: An Official Journal of the American Association for Cancer Research*, *5*(8), 2192–2197. <https://pubmed.ncbi.nlm.nih.gov/10473105/> [Date accessed: 23/01/25]

95   Liu, Y., & Sheikh, M. S. (2014). Melanoma: Molecular Pathogenesis and Therapeutic Management. *Molecular and Cellular Pharmacology*, *6*(3), 228. <https://pmc.ncbi.nlm.nih.gov/articles/PMC4346328/> [Date accessed: 23/01/25]

96   Luke, J. J., & Schwartz, G. K. (2013). Chemotherapy in the Management of Advanced Cutaneous Malignant Melanoma. *Clinics in Dermatology*, *31*(3), 290–297, doi: 10.1016/j.clindermatol.2012.08.016

97   Li, R.-H., Hou, X.-Y., Yang, C.-S., Liu, W.-L., Tang, J.-Q., Liu, Y.-Q., & Jiang, G. (2015). Temozolomide for Treating Malignant Melanoma. *Journal of the College of Physicians and Surgeons--Pakistan: JCPSP*, *25*(9), 680–688. <https://pubmed.ncbi.nlm.nih.gov/26374366/> [Date accessed: 23/01/25]

98    Middleton, M. R., Grob, J. J., Aaronson, N., Fierlbeck, G., Tilgen, W., Seiter, S., Gore, M., Aamdal, S., Cebon, J., Coates, A., Dreno, B., Henz, M., Schadendorf, D., Kapp, A., Weiss, J., Fraass, U., Statkevich, P., Muller, M., & Thatcher, N. (2000). Randomized phase III study of temozolomide versus dacarbazine in the treatment of patients with advanced metastatic malignant melanoma. *Journal of Clinical Oncology: Official Journal of the American Society of Clinical Oncology*, *18*(1), 158–166, doi: 10.1200/JCO.2000.18.1.158

99    Patel, P. M., Suciu, S., Mortier, L., Kruit, W. H., Robert, C., Schadendorf, D., Trefzer, U., Punt, C. J. A., Dummer, R., Davidson, N., Becker, J., Conry, R., Thompson, J. A., Hwu, W.-J., Engelen, K., Agarwala, S. S., Keilholz, U., Eggermont, A. M. M., & Spatz, A. (2011). Extended schedule, escalated dose temozolomide versus dacarbazine in stage IV melanoma: Final results of a randomised phase III study (EORTC 18032). *European Journal of Cancer*, *47*(10), 1476–1483, doi: 10.1016/j.ejca.2011.04.030

100   Paul, M. J., Summers, Y., Calvert, A. H., Rustin, G., Brampton, M. H., Thatcher, N., & Middleton, M. R. (2002). Effect of temozolomide on central nervous system relapse in patients with advanced melanoma. *Melanoma Research*, *12*(2), 175–178, doi: 10.1097/00008390-200204000-00011

101   Tarhini, A., Lo, E., & Minor, D. R. (2010). Releasing the Brake on the Immune System: Ipilimumab in Melanoma and Other Tumors. *Cancer Biotherapy & Radiopharmaceuticals*, *25*(6), 601–613, doi: 10.1089/cbr.2010.0865

102   Saad, P., & Kasi, A. (2023). Ipilimumab. *PubMed; StatPearls Publishing*. <https://www.ncbi.nlm.nih.gov/books/NBK557795/> [Date accessed: 24/01/25]

103   Camacho, L. H. (2015). CTLA-4 blockade with ipilimumab: biology, safety, efficacy, and future considerations. *Cancer Medicine*, *4*(5), 661–672, doi: 10.1002/cam4.371

104   Larkin, J., Chiarion-Sileni, V., Gonzalez, R., Grob, J.-J., Rutkowski, P., Lao, C. D., Cowey, C. L., Schadendorf, D., Wagstaff, J., Dummer, R., Ferrucci, P. F., Smylie, M., Hogg, D., Hill, A., Márquez-Rodas, I., Haanen, J., Guidoboni, M., Maio, M., Schöffski, P., & Carlino, M. S. (2019). Five-Year Survival with Combined Nivolumab and Ipilimumab in Advanced Melanoma. *New England Journal of Medicine*, *381*(16), 1535–1546, doi: 10.1056/nejmoa1910836

105   Bristol-Myers Squibb. (2025). A Phase 3, Randomized, Double-Blind Study of Nivolumab Monotherapy or Nivolumab Combined With Ipilimumab Versus Ipilimumab Monotherapy in Subjects With Previously Untreated Unresectable or Metastatic Melanoma. *Clinicaltrials.gov*. <https://clinicaltrials.gov/study/NCT01844505> [Date accessed: 24/01/25]

106   NCI Drug Dictionary. (2025). *Cancer.gov*. <https://www.cancer.gov/publications/dictionaries/cancer-drug/def/vemurafenib> [Date accessed: 24/01/25]

107 Khaddour, K., Kurn, H., & Zito, P. M. (2020). Vemurafenib. *PubMed; StatPearls Publishing*. <https://www.ncbi.nlm.nih.gov/books/NBK535429/> [Date accessed: 24/01/25]

108 Chapman, P. B., Hauschild, A., Robert, C., Haanen, J. B., Ascierto, P., Larkin, J., Dummer, R., Garbe, C., Testori, A., Maio, M., Hogg, D., Lorigan, P., Lebbe, C., Jouary, T., Schadendorf, D., Ribas, A., O'Day, S. J., Sosman, J. A., Kirkwood, J. M., & Eggermont, A. M. M. (2011). Improved survival with vemurafenib in melanoma with BRAF V600E mutation. *The New England Journal of Medicine*, *364*(26), 2507–2516, doi: 10.1056/NEJMoa1103782

109 Maverakis, E., Tran, K., Cheng, M., Mitra, A., Ogawa, H., Shi, V., Olney, L., & Kloxin, A. (2015). MEK inhibitors and their potential in the treatment of advanced melanoma: the advantages of combination therapy. *Drug Design, Development and Therapy*, 43, doi: 10.2147/dddt.s93545

110 Wu, P.-K., & Park, J.-I. (2015). MEK1/2 Inhibitors: Molecular Activity and Resistance Mechanisms. *Seminars in Oncology*, *42*(6), 849–862, doi: 10.1053/j.seminoncol.2015.09.023

111 Ascierto, P. A., Dréno, B., Larkin, J., Ribas, A., Liszkay, G., Maio, M., Mandalà, M., Demidov, L., Stroyakovskiy, D., Thomas, L., de la Cruz-Merino, L., Atkinson, V., Dutriaux, C., Garbe, C., Hsu, J., Jones, S., Li, H., McKenna, E., Voulgari, A., & McArthur, G. A. (2021). 5-Year Outcomes with Cobimetinib plus Vemurafenib in *BRAF*V600 Mutation–Positive Advanced Melanoma: Extended Follow-up of the coBRIM Study. *Clinical Cancer Research*, *27*(19), 5225–5235, doi: 10.1158/1078-0432.ccr-21-0809

112 Hoffmann-La Roche (2025). A Phase III, Double-Blind, Placebo-Controlled Study of Vemurafenib Versus Vemurafenib Plus GDC-0973 in Previously Untreated BRAF^600-Mutation Positive Patients With Unresectable Locally Advanced or Metastatic Melanoma. *Clinicaltrials.gov*. <https://clinicaltrials.gov/study/NCT01689519> [Date accessed: 24/01/25]

113 Halim, A.B. *Biomarkers, Diagnostics and Precision Medicine in the Drug Industry*. (Academic Press, 2019).

114 Zhang, L., Hao, B., Geng, Z., & Geng, Q. (2022). Toripalimab: the First Domestic Anti-Tumor PD-1 Antibody in China. *Frontiers in Immunology*, *12*, doi: 10.3389/fimmu.2021.730666

115 Ramagopal, U. A., Liu, W., Garrett-Thomson, S. C., Bonanno, J. B., Yan, Q., Srinivasan, M., Wong, S. C., Bell, A., Mankikar, S., Rangan, V. S., Deshpande, S., Korman, A. J., & Almo, S. C. (2017). Structural basis for cancer immunotherapy by the first-in-class checkpoint inhibitor ipilimumab. *Proceedings of the National Academy of Sciences*, *114*(21), E4223–E4232, doi: 10.1073/pnas.1617941114

116  Ramos, A., Sadeghi, S., & Tabatabaeian, H. (2021). Battling Chemoresistance in Cancer: Root Causes and Strategies to Uproot Them. *International Journal of Molecular Sciences*, *22*(17), 9451, doi: 10.3390/ijms22179451

117  Zheng, H.-C. (2017). The molecular mechanisms of chemoresistance in cancers. *Oncotarget*, *8*(35), doi: 10.18632/oncotarget.19048

118  Bartosz Wilczyński, Alicja Dąbrowska, Julita Kulbacka, & Dagmara Baczyńska. (2024). Chemoresistance and the tumor microenvironment: the critical role of cell–cell communication. *Cell Communication and Signaling*, *22*(1), doi: 10.1186/s12964-024-01857-7

119  Filipits, M. (2004). Mechanisms of cancer: multidrug resistance. *Drug Discovery Today: Disease Mechanisms*, *1*(2), 229–234, doi: 10.1016/j.ddmec.2004.10.001

120  Kannampuzha, S., Gopalakrishnan, A. V. (2023). Cancer chemoresistance and its mechanisms: Associated molecular factors and its regulatory role. *Medical Oncology*, *40*(9), doi: 10.1007/s12032-023-02138-y

121  Kalal, B. S., Upadhya, D., & Pai, V. R. (2017). Chemotherapy resistance mechanisms in advanced skin cancer. *Oncology Reviews*, *11*(1), doi: 10.4081/oncol.2017.326

122  Elliott, A. M., & Al-Hajj, M. A. (2009). ABCB8 Mediates Doxorubicin Resistance in Melanoma Cells by Protecting the Mitochondrial Genome. *Molecular Cancer Research*, *7*(1), 79–87, doi: 10.1158/1541-7786.mcr-08-0235

123  Frank, N. Y., Margaryan, A., Huang, Y., Schatton, T., Waaga-Gasser, A. M., Gasser, M., Sayegh, M. H., Sadee, W., & Frank, M. H. (2005). ABCB5-Mediated Doxorubicin Transport and Chemoresistance in Human Malignant Melanoma. *Cancer Research*, *65*(10), 4320–4333, doi: 10.1158/0008-5472.can-04-3327

124  Liedert, B., Materna, V., Schadendorf, D., Thomale, J., & Lage, H. (2003). Overexpression of cMOAT (MRP2/ABCC2) Is Associated with Decreased Formation of Platinum-DNA Adducts and Decreased G2-Arrest in Melanoma Cells Resistant to Cisplatin. *Journal of Investigative Dermatology*, *121*(1), 172–176, doi: 10.1046/j.1523-1747.2003.12313.x

125  Khanisyah Erza Gumilar, Chin, Y., Ibrahim, I. H., Tjokroprawiro, B. A., Yang, J.-Y., Zhou, M., Gassman, N. R., & Tan, M. (2023). Heat Shock Factor 1 Inhibition: A Novel Anti-Cancer Strategy with Promise for Precision Oncology. *Cancers*, *15*(21), 5167–5167, doi: 10.3390/cancers15215167

126  Nakamura, Y., Fujimoto, M., Fukushima, S., Nakamura, A., Hayashida, N., Ryosuke Takii, Takaki, E., Nakai, A., & Muto, M. (2014). Heat shock factor 1 is required for migration and invasion of human melanoma in vitro and in vivo. *Cancer Letters*, *354*(2), 329–335, doi: 10.1016/j.canlet.2014.08.029

127  Rünger, T. M., Emmert, S., Schadendorf, D., Diem, C., Bernd Epe, & D. Hellfritsch. (2000). Alterations of DNA Repair in Melanoma Cell Lines Resistant to Cisplatin, Fotemustine, or Etoposide. *Journal of Investigative Dermatology*, *114*(1), 34–39, doi: 10.1046/j.1523-1747.2000.00844.x

128  Fu, D., Calvo, J. A., & Samson, L. D. (2012). Balancing repair and tolerance of DNA damage caused by alkylating agents. *Nature Reviews Cancer*, *12*(2), 104–120, doi: 10.1038/nrc3185

129  Christmann, M., Pick, M., Lage, H., Schadendorf, D., & Kaina, B. (2001). Acquired resistance of melanoma cells to the antineoplastic agent

fotemustine is caused by reactivation of the DNA repair gene MGMT. *International Journal of Cancer*, *92*(1), 123–129, doi: 10.1002/1097-0215(200102)9999:9999<::AID-IJC1160>3.0.CO;2-V

130 Anvekar, R. A., Asciolla, J. J., Missert, D. J., & Chipuk, J. E. (2011). Born to be Alive: A Role for the BCL-2 Family in Melanoma Tumor Cell Survival, Apoptosis, and Treatment. *Frontiers in Oncology*, *1*, doi: 10.3389/fonc.2011.00034

131 Koetz-Ploch, L., Hanniford, D., Igor Dolgalev, Sokolova, E., Zhong, J., Díaz-Martínez, M., Bernstein, E., Farbod Darvishian, Flaherty, K. T., Chapman, P. B., Hussein Tawbi, & Hernando, E. (2017). MicroRNA-125a promotes resistance to BRAF inhibitors through suppression of the intrinsic apoptotic pathway. *Pigment Cell & Melanoma Research*, *30*(3), 328–338, doi: 10.1111/pcmr.12578

132 Tran, K. B., Kolekar, S., Jabed, A., Jaynes, P., Shih, J.-H., Wang, Q., Flanagan, J. U., Rewcastle, G. W., Baguley, B. C., & Shepherd, P. R. (2021). Diverse mechanisms activate the PI 3-kinase/mTOR pathway in melanomas: implications for the use of PI 3-kinase inhibitors to overcome resistance to inhibitors of BRAF and MEK. *BMC Cancer*, *21*(1), doi: 10.1186/s12885-021-07826-4

133 Olivo, E., La Chimia, M., Ceramella, J., Catalano, A., Chiaradonna, F., Sinicropi, M. S., Cuda, G., Iacopetta, D., & Scumaci, D. (2022). Moving beyond the Tip of the Iceberg: DJ-1 Implications in Cancer Metabolism. *Cells*, *11*(9), 1432, doi: 10.3390/cells11091432

134 Tao, X., & Tong, L. (2003). Crystal Structure of Human DJ-1, a Protein Associated with Early Onset Parkinson's Disease. *Journal of Biological Chemistry*, *278*(33), 31372–31379, doi: 10.1074/jbc.m304221200

135 Wilson, M. A., Collins, J. L., Hod, Y., Ringe, D., & Petsko, G. A. (2003). The 1.1-A resolution crystal structure of DJ-1, the protein mutated in autosomal recessive early onset Parkinson's disease. *Proceedings of the National Academy of Sciences*, *100*(16), 9256–9261, doi: 10.1073/pnas.1133288100

136 Tashiro, S., Caaveiro, J. M. M., Nakakido, M., Tanabe, A., Nagatoishi, S., Tamura, Y., Matsuda, N., Liu, D., Hoang, Q. Q., & Tsumoto, K. (2018). Discovery and Optimization of Inhibitors of the Parkinson's Disease Associated Protein DJ-1. *ACS Chemical Biology*, *13*(9), 2783–2793, doi: 10.1021/acschembio.8b00701

137 Zhang, L., Wang, J., Wang, J., Yang, B., He, Q., & Weng, Q. (2020). Role of DJ-1 in Immune and Inflammatory Diseases. *Frontiers in Immunology*, *11*, doi: 10.3389/fimmu.2020.00994

138 Mencke, P., Boussaad, I., Romano, C. D., Kitami, T., Linster, C. L., & Krüger, R. (2021). The Role of DJ-1 in Cellular Metabolism and Pathophysiological Implications for Parkinson's Disease. *Cells*, *10*(2), 347, doi: 10.3390/cells10020347

139 Wilson, M. A. (2011). The Role of Cysteine Oxidation in DJ-1 Function and Dysfunction. *Antioxidants & Redox Signaling*, *15*(1), 111–122, doi: 10.1089/ars.2010.3481

140 Dolgacheva, L. P., Berezhnov, A. V., Fedotova, E. I., Zinchenko, V. P., & Abramov, A. Y. (2019). Role of DJ-1 in the mechanism of pathogenesis of Parkinson's disease. *Journal of Bioenergetics and Biomembranes*, *51*(3), 175–188, doi: 10.1007/s10863-019-09798-4

141 Sun, M. E., & Zheng, Q. (2023). The Tale of DJ-1 (PARK7): A Swiss Army Knife in Biomedical and Psychological Research. *International Journal of Molecular Sciences*, *24*(8), 7409–7409, doi: 10.3390/ijms24087409

142 Andreeva, A., Bekkhozhin, Z., Omertassova, N., Baizhumanov, T., Yeltay, G., Akhmetali, M., Toibazar, D., & Utepbergenov, D. (2019). The apparent deglycase activity of DJ-1 results from the conversion of free methylglyoxal present in fast equilibrium with hemithioacetals and hemiaminals. *Journal of Biological Chemistry*, *294*(49), 18863–18872, doi: 10.1074/jbc.RA119.011237

143 Mazza, M. C., Shuck, S. C., Lin, J., Moxley, M. A., Termini, J., Cookson, M. R., & Wilson, M. A. (2022). DJ-1 is not a deglycase and makes a modest contribution to cellular defense against methylglyoxal damage in neurons. *Journal of Neurochemistry*, *162*(3), 245–261, doi: 10.1111/jnc.15656

144 Richarme, G., Mihoub, M., Dairou, J., Bui, L. C., Leger, T., & Lamouri, A. (2014). Parkinsonism-associated Protein DJ-1/Park7 Is a Major Protein Deglycase That Repairs Methylglyoxal- and Glyoxal-glycated Cysteine, Arginine, and Lysine Residues. *Journal of Biological Chemistry*, *290*(3), 1885–1897, doi: 10.1074/jbc.m114.597815

145 Toyoda, Y., Cihan Erkut, Pan-Montojo, F., Boland, S., Stewart, M. P., Müller, D. J., Wurst, W., Hyman, A. A., & Kurzchalia, T. V. (2014). Products of the Parkinson's disease-related glyoxalase DJ-1, D-lactate and glycolate, support mitochondrial membrane potential and neuronal survival. *Biology Open*, *3*(8), 777–784, doi: 10.1242/bio.20149399

146 Dash, B. K., Urano, Y., Saito, Y., & Noguchi, N. (2022). Redox-sensitive DJ-1 protein: an insight into physiological roles, secretion, and therapeutic target. *Redox Experimental Medicine*, (1), doi: 10.1530/rem-22-0007

147 Oh, S. E., & Mouradian, M. M. (2017). Regulation of Signal Transduction by DJ-1. *Advances in Experimental Medicine and Biology*, *1037*, 97–131, doi: 10.1007/978-981-10-6583-5_8

148 Gan, L., Johnson, D. A., & Johnson, J. A. (2010). Keap1-Nrf2 activation in the presence and absence of DJ-1. *European Journal of Neuroscience*, *31*(6), 967–977, doi: 10.1111/j.1460-9568.2010.07138.x

149 Rojo de la Vega, M., Chapman, E., & Zhang, D. D. (2018). NRF2 and the Hallmarks of Cancer. *Cancer Cell*, *34*(1), 21–43, doi: 10.1016/j.ccell.2018.03.022

150 He, F., Ru, X., & Wen, T. (2020). NRF2, a Transcription Factor for Stress Response and Beyond. *International Journal of Molecular Sciences*, *21*(13), doi: 10.3390/ijms21134777

151 Saha, S., Buttari, B., Panieri, E., Profumo, E., & Saso, L. (2020). An Overview of Nrf2 Signaling Pathway and Its Role in Inflammation. *Molecules*, *25*(22), 5474, doi: 10.3390/molecules25225474

152 Zhang, D. D. (2025). Thirty years of NRF2: advances and therapeutic challenges. *Nature Reviews Drug Discovery*, doi: 10.1038/s41573-025-01145-0

153 Fernández-Ginés, R., José Antonio Encinar, Hayes, J. D., Oliva, B., Rodríguez-Franco, M. I., Rojo, A. I., & Cuadrado, A. (2022). An inhibitor of interaction between the transcription factor NRF2 and the E3 ubiquitin ligase adapter β-TrCP delivers anti-inflammatory responses in mouse liver. *Redox Biology*, *55*, 102396–102396, doi: 10.1016/j.redox.2022.102396

154 Dong Joon Kim, Yong Weon Yi, & Seong, Y.-S. (2023). Beta-Transducin Repeats-Containing Proteins as an Anticancer Target. *Cancers*, *15*(17), 4248–4248, doi: 10.3390/cancers15174248

155 Chowdhry, S., Zhang, Y., McMahon, M., Sutherland, C., Cuadrado, A., & Hayes, J. D. (2012). Nrf2 is controlled by two distinct β-TrCP recognition motifs in its Neh6 domain, one of which can be modulated by GSK-3 activity. *Oncogene*, *32*(32), 3765–3781, doi: 10.1038/onc.2012.388

156 Tonelli, C., Chio, I. I. C., & Tuveson, D. A. (2018). Transcriptional Regulation by Nrf2. *Antioxidants & Redox Signaling*, *29*(17), 1727–1745, doi: 10.1089/ars.2017.7342

157 Zgorzynska, E., Dziedzic, B., & Walczewska, A. (2021). An Overview of the Nrf2/ARE Pathway and Its Role in Neurodegenerative Diseases. *International Journal of Molecular Sciences*, *22*(17), 9592, doi: 10.3390/ijms22179592

158 Zimta, A.-A., Cenariu, D., Irimie, A., Magdo, L., Nabavi, S. M., Atanasov, A. G., & Berindan-Neagoe, I. (2019). The Role of Nrf2 Activity in Cancer Development and Progression. *Cancers*, *11*(11), doi: 10.3390/cancers11111755

159 Torrente, L., Maan, G., Asma Oumkaltoum Rezig, Quinn, J., Jackson, A., Grilli, A., Casares, L., Zhang, Y., Evgeny Kulesskiy, Saarela, J., Silvio Bicciato, Edwards, J., Dinkova-Kostova, A. T., & Laureano. (2020). High NRF2 Levels Correlate with Poor Prognosis in Colorectal Cancer Patients and with Sensitivity to the Kinase Inhibitor AT9283 In Vitro. *Biomolecules*, *10*(10), 1365–1365, doi: 10.3390/biom10101365

160 Kumar, H., Kumar, R. M., Bhattacharjee, D., Somanna, P., & Jain, V. (2022). Role of Nrf2 Signaling Cascade in Breast Cancer: Strategies and Treatment. *Frontiers in Pharmacology*, *13*, doi: 10.3389/fphar.2022.720076

161 Zahra Malakoutikhah, Zahra Mohajeri, Dana, N., & Shaghayegh Haghjooy Javanmard. (2023). The dual role of Nrf2 in melanoma: a systematic review. *BMC Molecular and Cell Biology*, *24*(1), doi: 10.1186/s12860-023-00466-5

162 Weitzenböck, H. P., Gschwendtner, A., Wiesner, C., Depke, M., Schmidt, F., Franz Trautinger, Hengstschläger, M., Harald Hundsberger, & Mikula, M. (2021). Proteome analysis of NRF2 inhibition in melanoma reveals CD44 up-regulation and increased apoptosis resistance upon vemurafenib treatment. *Cancer Medicine*, *11*(4), 956–967, doi: 10.1002/cam4.4506

163 Menegon, S., Columbano, A., & Giordano, S. (2016). The Dual Roles of NRF2 in Cancer. *Trends in Molecular Medicine*, *22*(7), 578–593, doi: 10.1016/j.molmed.2016.05.002

164 Yoon, J.-H., Youn, K., & Jun, M. (2021). Protective effect of sargahydroquinoic acid against Aβ25–35-evoked damage via PI3K/Akt mediated Nrf2 antioxidant defense system. *Biomedicine & Pharmacotherapy*, *144*, 112271, doi: 10.1016/j.biopha.2021.112271

165 Niture, S. K., & Jaiswal, A. K. (2012). Nrf2 Protein Up-regulates Antiapoptotic Protein Bcl-2 and Prevents Cellular Apoptosis. *Journal of Biological Chemistry*, *287*(13), 9873–9886, doi: 10.1074/jbc.m111.312694

166 Pouremamali, F., Pouremamali, A., Dadashpour, M., Soozangar, N., & Jeddi, F. (2022). An update of Nrf2 activators and inhibitors in cancer prevention/promotion. *Cell Communication and Signaling*, *20*(1), doi: 10.1186/s12964-022-00906-3

167 Bao, S., Yi, M., Xiang, B., & Chen, P. (2024). Antitumor mechanisms and future clinical applications of the natural product triptolide. *Cancer Cell International*, *24*(1), doi: 10.1186/s12935-024-03336-y

168 Srivastava, R., Fernández-Ginés, R., Encinar, J. A., Cuadrado, A., & Wells, G. (2022). The current status and future prospects for therapeutic targeting of KEAP1-NRF2 and β-TrCP-NRF2 interactions in cancer chemoresistance. *Free Radical Biology and Medicine*, *192*, 246–260, doi: 10.1016/j.freeradbiomed.2022.09.023

169 Sveinbjornsdottir, S. (2016). The clinical symptoms of Parkinson's disease. *Journal of Neurochemistry*, *139*(S1), 318–324, doi: 10.1111/jnc.13691

170 Aarsland, D., Batzu, L., Halliday, G. M., Geurtsen, G. J., Ballard, C., Ray Chaudhuri, K., & Weintraub, D. (2021). Parkinson disease-associated cognitive impairment. *Nature Reviews Disease Primers*, *7*(1), doi: 10.1038/s41572-021-00280-3

171 Beitz, J. (2014). Parkinson's Disease: A Review. *Frontiers in Bioscience, 6*(1), 65-74, doi: 10.2741/s415

172 Morris, H. R., Spillantini, M. G., Sue, C. M., & Williams-Gray, C. H. (2024). The pathogenesis of Parkinson's disease. *Lancet (London, England)*, *403*(10423), 293–304, doi: 10.1016/S0140-6736(23)01478-2

173 Bonifati, V. (2003). Mutations in the DJ-1 Gene Associated with Autosomal Recessive Early-Onset Parkinsonism. *Science*, *299*(5604), 256–259, doi: 10.1126/science.1077209

174 Skou, L. D., Johansen, S. K., Okarmus, J., & Meyer, M. (2024). Pathogenesis of DJ-1/PARK7-Mediated Parkinson's Disease. *Cells*, *13*(4), 296, doi: 10.3390/cells13040296

175 Huang, M., & Chen, S. (2021). DJ-1 in neurodegenerative diseases: Pathogenesis and clinical application. *Progress in Neurobiology*, *204*, 102114, doi: 10.1016/j.pneurobio.2021.102114

176 Krebiehl, G., Ruckerbauer, S., Burbulla, L. F., Kieper, N., Maurer, B., Waak, J., Wolburg, H., Gizatullina, Z., Gellerich, F. N., Woitalla, D., Riess, O., Kahle, P. J., Proikas-Cezanne, T., & Krüger, R. (2010). Reduced Basal Autophagy and Impaired Mitochondrial Dynamics Due to Loss of Parkinson's Disease-Associated Protein DJ-1. *PLOS One*, *5*(2), e9367, doi: 10.1371/journal.pone.0009367

177 Lee, Y. J., Kim, W. I., Park, T. H., Bae, J. H., Nam, H. S., Cho, S. W., Choi, Y. J., Lee, S. H., & Cho, M. K. (2020). Upregulation of DJ-1 expression in melanoma regulates PTEN/AKT pathway for cell survival and migration. *Archives of Dermatological Research*, *313*(7), 583–591, doi: 10.1007/s00403-020-02139-1

178 Chen, L.-L., Tian, J.-J., Su, L., Jing, Y., Zhang, S.-C., Zhang, H.-X., Wang, X.-Q., & Zhu, C.-B. (2014). DJ-1: a promising marker in metastatic uveal melanoma. *Journal of Cancer Research and Clinical Oncology*, *141*(2), 315–321, doi: 10.1007/s00432-014-1804-2

179 Tang, Z., Li, C., Kang, B., Gao, G., Li, C., & Zhang, Z. (2017). GEPIA: a web server for cancer and normal gene expression profiling and interactive analyses. *Nucleic Acids Research*, *45*(W1), 98–102, doi: 10.1093/nar/gkx247

180 Leong, Y. Q., Wen, S., & Khuen Yen Ng. (2021). Cancer risk in Parkinson disease: An updated systematic review and meta-analysis. *European Journal of Neurology*, *28*(12), 4219–4237, doi: 10.1111/ene.15069

181 Clements, C. M., McNally, R. S., Conti, B. J., Mak, T. W., & Ting, J. P.-Y. (2006). DJ-1, a cancer- and Parkinson's disease-associated protein, stabilizes the antioxidant transcriptional master regulator Nrf2. *Proceedings of the National Academy of Sciences*, *103*(41), 15091–15096, doi: 10.1073/pnas.0607260103

182 Jin, W. (2020). Novel Insights into PARK7 (DJ-1), a Potential Anti-Cancer Therapeutic Target, and Implications for Cancer Progression. *Journal of Clinical Medicine*, *9*(5), 1256, doi: 10.3390/jcm9051256

183 Raninga, P. V., Di Trapani, G., & Tonissen, K. F. (2014). Cross talk between two antioxidant systems, Thioredoxin and DJ-1: consequences for cancer. *Oncoscience*, *1*(1), 95–110, doi: 10.18632/oncoscience.12

184 Tournier, C. (2013). The 2 Faces of JNK Signaling in Cancer. *Genes & Cancer*, *4*(9-10), 397–400, doi: 10.1177/1947601913486349

185 Dhanasekaran, D. N., & Reddy, E. P. (2017). JNK-signaling: A multiplexing hub in programmed cell death. *Genes & Cancer*, *8*(9-10), 682–694, doi: 10.18632/genesandcancer.155

186 Nadel, G., Galia Maik-Rachline, & Seger, R. (2023). JNK Cascade-Induced Apoptosis—A Unique Role in GqPCR Signaling. *International Journal of Molecular Sciences*, *24*(17), 13527–13527, doi: 10.3390/ijms241713527

187 Kale, J., Osterlund, E. J., & Andrews, D. W. (2017). BCL-2 family proteins: changing partners in the dance towards death. *Cell Death & Differentiation*, *25*(1), 65–80, doi: 10.1038/cdd.2017.186

188 O'Connor, L. (1998). Bim: a novel member of the Bcl-2 family that promotes apoptosis. *The EMBO Journal*, *17*(2), 384–395, doi: 10.1093/emboj/17.2.384

189 Yang, E., Zha, J., Jockel, J., Boise, L. H., Thompson, C. B., & Korsmeyer, S. J. (1995). Bad, a heterodimeric partner for Bcl-xL and Bcl-2, displaces bax and promotes cell death. *Cell*, *80*(2), 285–291, doi: 10.1016/0092-8674(95)90411-5

190 Im, J.-Y., Lee, K.-W., Junn, E., & Mouradian, M. M. (2010). DJ-1 protects against oxidative damage by regulating the thioredoxin/ASK1 complex. *Neuroscience Research*, *67*(3), 203–208, doi: 10.1016/j.neures.2010.04.002

191 Oh, S. E., & Mouradian, M. M. (2017a). Cytoprotective mechanisms of DJ-1 against oxidative stress through modulating ERK1/2 and ASK1 signal transduction. *Redox Biology*, *14*, 211–217, doi: 10.1016/j.redox.2017.09.008

192 Mazurakova, A., Lenka Koklesova, Sandra Hurta Csizmár, Samec, M., Aranka Brockmüller, Miroslava Šudomová, Biringer, K., Kudela, E., Pec, M., Samson Mathews Samuel, Kassayova, M., Sherif T.S. Hassan, Smejkal, K., Mehdi Shakibaei, Dietrich Büsselberg, Saso, L., Kubatka, P., & Golubnitschaja, O. (2024). Significance of flavonoids targeting PI3K/Akt/HIF-1α signaling pathway in therapy-resistant cancer cells – A potential contribution to the predictive, preventive, and personalized medicine. *Journal of Advanced Research*, *55*, 103–118, doi: 10.1016/j.jare.2023.02.015

193 Basheeruddin, M., & Qausain, S. (2024). Hypoxia-Inducible Factor 1-Alpha (HIF-1α) and Cancer: Mechanisms of Tumor Hypoxia and Therapeutic Targeting. *Cureus*, *16*(10), doi: 10.7759/cureus.70700

194 Song, C. W., Kim, H., Kim, M.-S., Park, H. J., Paek, S.-H., Terezakis, S., & Cho, L. C. (2024). Role of HIF-1α in the Responses of Tumors to Radiotherapy and Chemotherapy. *Cancer Research and Treatment*, doi: 10.4143/crt.2024.255

195 Vasseur, S., Afzal, S., Tardivel-Lacombe, J., Park, D. S., Iovanna, J. L., & Mak, T. W. (2009). DJ-1/PARK7 is an important mediator of hypoxia-induced cellular responses. *Proceedings of the National Academy of Sciences of the United States of America*, *106*(4), 1111–1116, doi: 10.1073/pnas.0812745106

196 Li, L., Zhang, C., Li, Y., Zhang, Y., & Lei, Y. (2020). DJ-1 promotes epithelial-to-mesenchymal transition via enhancing FGF9 expression in colorectal cancer. *Biology Open*, *9*(5), doi: 10.1242/bio.051680

197 McNally, R. S., Davis, B. K., Clements, C. M., Accavitti-Loper, M. A., Mak, T. W., & Ting, J. P.-Y. (2010). DJ-1 Enhances Cell Survival through the Binding of Cezanne, a Negative Regulator of NF-κB. *Journal of Biological Chemistry*, *286*(6), 4098–4106, doi: 10.1074/jbc.m110.147371

198 Cao, J., Lou, S., Ying, M., & Yang, B. (2015). DJ-1 as a human oncogene and potential therapeutic target. *Biochemical Pharmacology, 93*(3), 241–250, doi: 10.1016/j.bcp.2014.11.012

199 Saidu, N. E. B., Noé, G., Cerles, O., Cabel, L., Kavian-Tessler, N., Chouzenoux, S., Bahuaud, M., Chéreau, C., Nicco, C., Leroy, K., Borghese, B., Goldwasser, F., Batteux, F., & Alexandre, J. (2017). Dimethyl Fumarate Controls the NRF2/DJ-1 Axis in Cancer Cells: Therapeutic Applications. *Molecular Cancer Therapeutics*, *16*(3), 529–539, doi: 10.1158/1535-7163.MCT-16-0405

200 Rupp, T., Solène Debasly, Genest, L., Guillaume Froget, & Castagné, V. (2022). Therapeutic Potential of Fingolimod and Dimethyl Fumarate in Non-Small Cell Lung Cancer Preclinical Models. *International Journal of Molecular Sciences*, *23*(15), 8192–8192, doi: 10.3390/ijms23158192

201 Saidu, N. E. B., Kavian, N., Leroy, K., Jacob, C., Nicco, C., Batteux, F., & Alexandre, J. (2019). Dimethyl fumarate, a two-edged drug: Current status and future directions. *Medicinal Research Reviews*, *39*(5), 1923–1952, doi: 10.1002/med.21567

202 Ismail, I. A., El-Sokkary, G. H., & Saber, S. H. (2018). Low doses of Paclitaxel repress breast cancer invasion through DJ-1/KLF17 signalling pathway. *Clinical and Experimental Pharmacology and Physiology*, *45*(9), 961–968, doi: 10.1111/1440-1681.12960

203 Zhou, J., Zhang, L., Wang, M., Zhou, L., Feng, X., Yu, L., Lan, J., Gao, W., Zhang, C., Bu, Y., Huang, C., Zhang, H., & Lei, Y. (2019). CPX Targeting DJ-1 Triggers ROS-induced Cell Death and Protective Autophagy in Colorectal Cancer. *Theranostics*, *9*(19), 5577–5594, doi: 10.7150/thno.34663

204 Taira, T., Saito, Y., Niki, T., Iguchi-Ariga, S. M. M., Takahashi, K., & Ariga, H. (2004). DJ-1 has a role in antioxidative stress to prevent cell death. *EMBO Reports*, *5*(2), 213–218, doi: 10.1038/sj.embor.7400074

205 Chen, X., Zhu, H., Bao, K., Jiang, L., Zhu, H., Ying, M., He, Q., Yang, B., Sheng, R., & Cao, J. (2021). Bis-isatin derivatives: design, synthesis, and biological activity evaluation as potent dimeric DJ-1 inhibitors. *Acta Pharmacologica Sinica*, *42*(7), 1160–1170, doi: 10.1038/s41401-020-00600-5

206 Lago-Baameiro, N., Santiago-Varela, M., Camino, T., Silva-Rodríguez, P., Bande, M., Blanco-Teijeiro, M. J., Pardo, M., & Piñeiro, A. (2023). PARK7/DJ-1

inhibition decreases invasion and proliferation of uveal melanoma cells. *Tumori*, *109*(1), 47–53, doi: 10.1177/03008916211061766

207 Patton, E. E., Mueller, K. L., Adams, D. J., Anandasabapathy, N., Aplin, A. E., Bertolotto, C., Bosenberg, M., Ceol, C. J., Burd, C. E., Chi, P., Herlyn, M., Holmen, S. L., Karreth, F. A., Kaufman, C. K., Khan, S., Kobold, S., Leucci, E., Levy, C., Lombard, D. B., & Lund, A. W. (2021). Melanoma models for the next generation of therapies. *Cancer Cell*, *39*(5), 610–631, doi: 10.1016/j.ccell.2021.01.011

208 Karras, F., & Kunz, M. (2024). Patient-derived melanoma models. *Pathology - Research and Practice*, *259*, 155231, doi: 10.1016/j.prp.2024.155231

209 Ran, R., Li, L., Shi, Z., Liu, G., Jiang, H., Fang, L., Xu, T., Huang, J., Chen, W., & Chen, Y. (2022). Disruption of tp53 leads to cutaneous nevus and melanoma formation in Xenopus tropicalis. *Molecular Oncology, 16*(19), 3554–3567, doi: 10.1002/1878-0261.13301

210 Joudi El Mir, Nasrallah, A., Thézé, N., Cario, M., Hussein Fayyad-Kazan, Thiébaud, P., & Rezvani, H. (2024). *Xenopus* as a model system for studying pigmentation and pigmentary disorders. *Pigment Cell & Melanoma Research*, doi: 10.1111/pcmr.13178

211 Marconi, A., Quadri, M., Saltari, A., & Pincelli, C. (2018). Progress in melanoma modelling in vitro. *Experimental Dermatology*, *27*(5), 578–586, doi: 10.1111/exd.13670

212 Rodrigues, D. B., Moreira, H. R., Jarnalo, M., Horta, R., Marques, A. P., Reis, R. L., & Pirraco, R. P. (2024). Generation of 3D melanoma models using an assembloid-based approach. *Acta Biomaterialia*, *178*, 93–110, doi: 10.1016/j.actbio.2024.02.023

213 Daugaard, N. D., Rikke Tholstrup, Jakob Rask Tornby, Bendixen, S. M., Larsen, F. T., Zio, D. D., Barnkob, M. B., Ravnskjaer, K., & Brewer, J. R. (2024). Characterization of Human Melanoma Skin Cancer Models: A step towards Model-Based Melanoma Research. *Acta Biomaterialia*, doi: 10.1016/j.actbio.2024.11.018

214 Boz Er, A. B., & Sumer, C. (2025). Spheroid Invasion Assay of Melanoma Cells by Hanging Drop Technique. *Methods in Molecular Biology (Clifton, N.J.)*, doi: 10.1007/7651_2025_615

215 Julien Ablain, Mahi, A. A., Rothschild, H., Prasad, M., Aires, S., Yang, S., Dokukin, M. E., Xu, S., Dang, M., Sokolov, I., Lian, C. G., & Zon, L. I. (2022). Loss of NECTIN1 triggers melanoma dissemination upon local IGF1 depletion. *Nature Genetics*, *54*(12), 1839–1852, doi: 10.1038/s41588-022-01191-z

216 Kim, S., Min, S., Choi, Y. S., Jo, S.-H., Jung, J. H., Han, K., Kim, J., An, S., Ji, Y. W., Kim, Y.-G., & Cho, S.-W. (2022). Tissue extracellular matrix hydrogels as alternatives to Matrigel for culturing gastrointestinal organoids. *Nature Communications*, *13*(1), doi: 10.1038/s41467-022-29279-4

217 Sanfilippo, S., Canis, M., Ouchchane, L., Botchorishvili, R., Artonne, C., Janny, L., & Brugnon, F. (2011). Viability assessment of fresh and frozen/thawed isolated human follicles: reliability of two methods (Trypan blue and Calcein AM/ethidium homodimer-1). *Journal of Assisted Reproduction and Genetics*, *28*(12), 1151–1156, doi: 10.1007/s10815-011-9649-y

218  Williams, M. J. (2024). Exploration of DJ-1 as a Therapeutic Target in Metastatic Melanoma. Masters thesis, University of East Anglia. UEA Digital Repository. <https://ueaeprints.uea.ac.uk/id/eprint/97677/> [Date accessed: 15/05/25]

219  Flockhart, R. J., Armstrong, J. L., Reynolds, N. J., & Lovat, P. E. (2009). NFAT signalling is a novel target of oncogenic BRAF in metastatic melanoma. *British Journal of Cancer*, *101*(8), 1448–1455, doi: 10.1038/sj.bjc.6605277

220  Ariza, M. E., Broome-Powell, M., Lahti, J. M., Kidd, V. J., & Nelson, M. A. (1999). Fas-induced Apoptosis in Human Malignant Melanoma Cell Lines Is Associated with the Activation of the p34 -related PITSLRE Protein Kinases. *Journal of Biological Chemistry*, *274*(40), 28505–28513, doi: 10.1074/jbc.274.40.28505

221  Quesnel, A., Martin, L. D., Tarzi, C., Lenis, V. P., Coles, N., Islam, M., Angione, C., Outeiro, T. F., Khundakar, A. A., & Filippou, P. S. (2024). Uncovering potential diagnostic and pathophysiological roles of α-synuclein and DJ-1 in melanoma. *Cancer Medicine*, *13*(1), doi: 10.1002/cam4.6900

222  De Lazzari, F., Prag, H. A., Gruszczyk, A. V., Whitworth, A. J., & Bisaglia, M. (2021). DJ-1: A promising therapeutic candidate for ischemia-reperfusion injury. *Redox Biology*, *41*, 101884, doi: 10.1016/j.redox.2021.101884

223  Junn, E., Jang, W. H., Zhao, X., Jeong, B. S., & Mouradian, M. M. (2009). Mitochondrial localization of DJ-1 leads to enhanced neuroprotection. *Journal of Neuroscience Research*, *87*(1), 123–129, doi: 10.1002/jnr.21831

224  Jin, F., Wang, H., Li, D., Fang, C., Li, W., Shi, Q., Diao, Y., Ding, Z., Dai, X., Tao, L., Masataka Sunagawa, Wu, F., Qian, Y., & Liu, Y. (2020). DJ-1 promotes cell proliferation and tumor metastasis in esophageal squamous cell carcinoma via the Wnt/β-catenin signaling pathway. *International Journal of Oncology*, doi: 10.3892/ijo.2020.5005

225  Ning, J., Mo, L., & Lai, X. (2025). Low- and high-dose hydrogen peroxide regulation of transcription factor NF-E2-related factor 2. *Chinese Medical Journal*, 123(8), 1063-1069, doi: 10.3760/cma.j.issn.0366-6999.2010.08.016

226  Belanova, A. A., Smirnov, D. S., Makarenko, M. S., Belousova, M. M., Mashkina, E. V., Aleksandrova, A. A., Soldatov, A. V., & Zolotukhin, P. V. (2017). Individual expression features of GPX2, NQO1 and SQSTM1 transcript variants induced by hydrogen peroxide treatment in HeLa cells. *Genetics and Molecular Biology*, *40*(2), 515–524, doi: 10.1590/1678-4685-gmb-2016-0005

227  Marinho, H. S., Real, C., Cyrne, L., Soares, H., & Antunes, F. (2014). Hydrogen peroxide sensing, signaling and regulation of transcription factors. *Redox Biology*, *2*, 535–562, doi: 10.1016/j.redox.2014.02.006

228  Fang, J., Islam, R., Gao, S., Zhang, C., Kunisaki, R., Sakaguchi, S., Honda, N., Zhou, J.-R., & Yokomizo, K. (2021). Expression Dynamics of Heme Oxygenase-1 in Tumor Cells and the Host Contributes to the Progression of Tumors. *Journal of Personalized Medicine*, *11*(12), 1340–1340, doi: 10.3390/jpm11121340

229  Jian, Z., Li, K., Liu, L., Zhang, Y., Zhou, Z., Li, C., & Gao, T. (2011). Heme Oxygenase-1 Protects Human Melanocytes from H2O2-Induced Oxidative Stress via the Nrf2-ARE Pathway. *Journal of Investigative Dermatology*, *131*(7), 1420–1427, doi: 10.1038/jid.2011.56

230  Dratkiewicz, E., Simiczyjew, A., Pietraszek-Gremplewicz, K., Mazurkiewicz, J., & Nowak, D. (2019). Characterization of Melanoma Cell Lines Resistant to

Vemurafenib and Evaluation of Their Responsiveness to EGFR- and MET-Inhibitor Treatment. *International Journal of Molecular Sciences*, *21*(1), 113, doi: 10.3390/ijms21010113

231  Vihinen, M. (2021). Functional effects of protein variants. *Biochimie*, *180*, 104–120, doi: 10.1016/j.biochi.2020.10.009

232  Karimi, H., Moskal, P., Agata Żak, & Stępień, E. Ł. (2023). 3D melanoma spheroid model for the development of positronium biomarkers. *Scientific Reports*, *13*(1), doi: 10.1038/s41598-023-34571-4

233  Wagner, M., Koyasu, S. (2020). A 3D Skin Melanoma Spheroid-Based Model to Assess Tumor-Immune Cell Interactions. *BioProtocol Journal,* 10(23), doi: 10.21769/BioProtoc.3839

234  Su, F., Bradley, W. D., Wang, Q., Yang, H., Xu, L., Higgins, B., Kolinsky, K., Packman, K., Min Jung Kim, Trunzer, K., Lee, R. J., Schostack, K., Carter, J., Thomas, A., Germer, S., Rosinski, J., Martin, M., Mary Ellen Simcox, Lestini, B., & Heimbrook, D. (2012). Resistance to Selective BRAF Inhibition Can Be Mediated by Modest Upstream Pathway Activation. *Cancer Research*, *72*(4), 969–978, doi: 10.1158/0008-5472.can-11-1875

235  Smalley, K. S. M., Haass, N. K., Brafford, P. A., Lioni, M., Flaherty, K. T., & Herlyn, M. (2006). Multiple signaling pathways must be targeted to overcome drug resistance in cell lines derived from melanoma metastases. *Molecular Cancer Therapeutics*, *5*(5), 1136–1144, doi: 10.1158/1535-7163.mct-06-0084

236  Shannan, B., Chen, Q., Watters, A., Perego, M., Krepler, C., Thombre, R., Li, L., Rajan, G., Peterson, S., Gimotty, P. A., Wilson, M., Nathanson, K. L., Gangadhar, T. C., Schuchter, L. M., Weeraratna, A. T., Herlyn, M., & Vultur, A. (2016). Enhancing the evaluation of PI3K inhibitors through 3D melanoma models. *Pigment Cell & Melanoma Research*, *29*(3), 317–328, doi: 10.1111/pcmr.12465

237  Girard, Y. K., Wang, C., Ravi, S., Howell, M. C., Mallela, J., Alibrahim, M., Green, R., Hellermann, G., Mohapatra, S. S., & Mohapatra, S. (2013). A 3D Fibrous Scaffold Inducing Tumoroids: A Platform for Anticancer Drug Development. *PLOS One*, *8*(10), e75345, doi: 10.1371/journal.pone.0075345

238  Edmondson, R., Broglie, J. J., Adcock, A. F., & Yang, L. (2014). Three-Dimensional Cell Culture Systems and Their Applications in Drug Discovery and Cell-Based Biosensors. *ASSAY and Drug Development Technologies*, *12*(4), 207–218, doi: 10.1089/adt.2014.573

239  Pérez, C. N., Falcón, C. R., Mons, J. D., Orlandi, F. C., Sangiacomo, M., Fernandez-Muñoz, J. M., Guerrero, M., Benito, P. G., Colombo, M. I., Zoppino, F. C. M. ., & Alvarez, S. E. (2023). Melanoma cells with acquired resistance to vemurafenib have decreased autophagic flux and display enhanced ability to transfer resistance. *Biochimica et Biophysica Acta (BBA) - Molecular Basis of Disease*, *1869*(7), 166801, doi: 10.1016/j.bbadis.2023.166801